

Tor Stensola

# Population codes in medial entorhinal cortex

Thesis for the degree of Doctor Philosophiae

Trondheim, May 2014

Norwegian University of Science and Technology  
Faculty of Medicine  
Centre for Neural Computation and  
Kavli Institute for Systems Neuroscience



**NTNU – Trondheim**  
Norwegian University of  
Science and Technology

**NTNU**

Norwegian University of Science and Technology

Thesis for the degree of Doctor Philosophiae

Faculty of Medicine  
Centre for Neural Computation and  
Kavli Institute for Systems Neuroscience

© Tor Stensola

ISBN 978-82-326-0234-6 (printed ver.)  
ISBN 978-82-326-0235-3 (electronic ver.)  
ISSN 1503-8181

Doctoral theses at NTNU, 2014:156

Printed by NTNU-trykk

## Norsk sammendrag

### *Populasjonskoder i mediale entorhinal korteks*

Hjernebarken utfører kontinuerlig et velde av kompliserte funksjoner, hvis mekanismer vi kan tjene mye på å forstå. Nevrovitenskap er et relativt nytt fag, men med utrolig moment. Mye vites i dag om enkle nevroners egenskaper, men nevralt komputering foregår i store trekk i interaksjonene mellom celler. Men på dette planet er det mange hindere som må overkommes; teknologisk nyvinning og konseptuell modning har ført til at nevrovitenskap gjennom de senere år har kunnet tilnærme seg spørsmål som fanger mekanismer på systemnivå. Hippokampus, som inneholder stedsselektive celler, utgjør et eksperimentelt system som tillater spørsmål om visse kjernemekanismer, slik som hukommelsesfunksjon og intern representasjonsdynamikk, uten streng eksperimentell kontroll på innkommende og utgående signaler slik man baserer seg på i for eksempel sansenevitenskap. I hippokampusforskning er dyrets naturlige adferd en enorm ressurs. På grunn av den sterke tilknytningen til rom kan man ved å korrelere nevralt aktivitet til dyrets adferd etablere svært robuste forhold mellom nevronenes aktivitet og funksjon på adferdnivå. Dette har ført til at hippokampusforskning har blitt en foregangsfront på innsamling av store datasett i dyr under normal adferd, samt tolkning av denne i adferdskontekst.

Et stort skritt mot å forstå hvordan stedsselektiviteten i hippokampus oppstår og brukes kom med funnet av gitterceller, celler som er aktive i et gittermønster som dekker hele miljøet. Vi vet mye om disse cellenes oppførsel på enkeltcellenivå, men på grunn av teknisk krevende innspillingsteknikk har det vært vanskelig å spille inn nok celler til å forstå hvordan disse kombinerer til en populasjonskode for rom. Denne hindringen har vi nå overkommet, og i første arbeid brukte vi nye teknikker for å spille inn store antall gitterceller innen dyr og viser at gittercellekartet er organisert i moduler, hver med sin egen kartgeometri. Vi viser hvordan disse modulene er fordelt i vevet, og utviklet nye analyser for å beskrive modulenes egenskaper. Vi viser at gitterkart i forskjellige moduler inad i dyr ikke bare kan innta forskjellig geometriske former, men også utføre separate operasjoner samtidig på samme eksperimentelle manipulering. Dette er første bevis på slik uavhengig funksjon i gitterkartet, og foreslår hvordan stedsceller kan generere høykapasitetslagring av representasjoner for forskjellige miljø.

I andre arbeid beskriver vi hvordan en annen funksjonelt definert cellegruppe i entorhinal korteks fungerer på populasjonsnivå, denne gangen for celler som koder retning til dyret i forhold til miljøet. Vi viser at denne populasjonen har en topografisk fordeling langs samme akse i vevet som gitterceller utviser topografi, men at denne er kontinuerlig i motsetning til gitterkartets modulære fordeling.

I siste arbeid viser vi at miljøets geometri bestemmer hvordan gitterkartet ankres til det eksterne rom. Vi beskriver en universal ankringsstrategi som er optimal for å skape størst mulig forskjell mellom populasjonskoder for områder langs rommets grenser. Dette brukes kanskje til å forhindre sanseforvirring av gitterkartet i miljø med geometrisk ambiguøse segmenter.

Avhandlingen legger frem første beskrivelser av nevralt mekanismer på populasjonsnivå i entorhinal korteks, og gir flere innsikter i generell organisering av nettverkene som er involvert i stedssans og hukommelse.

**Navn kandidat:** Tor Stensola

**Institutt:** Kavli Institute for Systems Neuroscience  
Centre for Neural Computation  
Institutt for Nevromedisin

**Veileder(e):** Professor Edvard I. Moser og Professor May-Britt Moser

## Summary

Current systems neuroscience has unprecedented momentum, in terms of both technological and conceptual development. It is crucial to study systems mechanisms and their associated functions with behavior in mind. Hippocampal and parahippocampal cortices has proved a highly suitable experimental system because the high level functions that are performed here, including episodic memory formation, are accessible through the clear readout of spatial behavior. Grid cells in medial entorhinal cortex (MEC) have been proposed to account for the spatial selectivity in downstream hippocampal place cells. Until now, however, entorhinal grid cells have only been studied on single cell- or small local ensemble level. The main reason for population studies lagging behind that of hippocampus is the technical difficulties associated with entorhinal implantation and recording.

Here we have overcome some of the main technical hurdles, and recorded unprecedented number of cells from distinct functional classes in MEC. We show in Paper 1 that the entorhinal grid map is organized into sub-maps-or modules-that contain grid cells sharing numerous features including spatial pattern scale, orientation, deformation and temporal modulation. We also demonstrate that grid modules in the same system can operate independently on the same input, raising the possibility that hippocampal capacity for encoding distinct spatial representations is enabled by the grid input.

We further show in Paper 2 that also head direction cells in entorhinal cortex distribute according to a functional topography along the dorsoventral axis. The head direction system, however, was not modular in contrast to the grid system.

Finally, Paper 3 details a common grid anchoring strategy shared across animals and environments. The grid pattern displayed a striking tendency to align to the cardinal axes of the environment, but systematically offset  $7.5^\circ$ . Through simulations, we show that this constitutes an optimal orientation of the grid to maximally decorrelate population encoding of environment border segments, providing a possible link to border-selective cells in the mechanisms that embeds internal representation of space into external frames of reference.

These findings have implications for our understanding of entorhinal and hippocampal computations and add several new venues for further investigation.



## List of papers

- Paper 1      The Entorhinal Grid Map is Discretized**  
Stensola H\*, Stensola T\*, Solstad T, Frøland K,  
Moser M-B and Moser EI (2012).  
*Nature*, 492, 72-78.
- Paper 2      Topography of Head Direction Cells in Medial Entorhinal Cortex**  
Giocomo LM, Stensola T\*, Bonnevie T\*, van Cauter T,  
Moser, M-B and Moser EI.  
Submitted to *Current Biology* 2013.
- Paper 3      Geometric Features of the Environment Determine Grid Orientation**  
Stensola T\*, Stensola H\*, Moser M-B and Moser EI.  
In preparation for submission to *Nature* 2014.

## **Acknowledgements**

Acknowledgements go to the Norwegian Research Council, European Research Council and Kavli Foundation, from which these projects received generous financial support.

I want to extend great appreciation for the work performed by technicians, engineers and animal personnel in the lab, which more essentially than anything else enables a productive and fertile scientific environment. Takk!

A lab is a strange social ecosystem. That is a fact. Nonetheless, the Centre has proven an extremely thriving and interesting paragon of such ecosystems. Warm thanks to great colleagues and friends! And the skiing!

A special thank you to Hanne, Lisa, Trygve, Kristian, Tora and Tiffany for sharing your expertise and science with me in our publications.

Albert, these have been great times for a couple of SRs, for which I am in eternal dept - and to your drawer! Michael, thank you for being a friend, and the first to lure me into entorhinal cortex.

My family, my parents in particular, have been extraordinarily supportive and above average interested in neural dynamics and spatial codes. That has meant very much to me; thank you.

Edvard and May-Britt, I can hardly express how grateful I am for everything you have done for me and meant to me. Your guidance is, has been, and will stand, as among the most important influences of my life.

...

Hanne, du har mer enn noe annet formet mitt sinn og mitt hjerte og min vitenskap. Takk for at du er verdens beste partner, i liv og vitenskap! Alio sub Sole

Sofie Veslemøy, under dette arbeidet kom du til verden og tok min med storm. Jeg dedikerer dette til deg.

**Trondheim October 2013**



## Contents

<b>1. Introduction</b>	<b>11</b>
1.1. Social anthropology of neurons	11
1.2. The importance of behavior	12
1.3. Keeping space in mind	12
1.3.1. The cognitive map	12
1.3.2. The neural map	13
1.3.3. Going upstream	15
<b>2. Objectives</b>	<b>17</b>
2.1. Functional organization of the entorhinal grid map	17
2.2. Functional organization of the entorhinal head direction system	17
2.3. Environmental features that control grid anchoring	18
<b>3. Synopsis of results</b>	<b>19</b>
<b>4. Discussion</b>	<b>25</b>
4.1. Grid modularity: implications for downstream computations	26
4.1.1. Place field generation	26
4.1.2. Place cell remapping: basics	28
4.1.3. Place cell remapping: attractor dynamics	32
4.2. Topography in the parahippocampal systems	34
4.3. A need to develop our understanding of grid spacing	36
4.4. Embedding internal representations into external frames	38
4.5. Oblique effect in grids?	39
<b>5. Conclusions</b>	<b>41</b>
Ethical and legal issues	42
References	43
<b>6. Contributions</b>	<b>55</b>
Paper 1	57
Paper 2	109
Paper 3	149



# 1 Introduction

---

Neuroscience is a relatively new discipline, and much of the brain's workings are still *terra incognita*. There are several interesting reasons for why this is the case. For one, the anatomical neuroarchitecture of even the smallest of animals is enormously complex. However, even in species that we have mapped every neuron's connections and developmental origin (*C. Elegans* has 302 neurons, the connections between which are all mapped out) and can put through rigorous experimental tests, the mechanisms behind most computations remain obscure<sup>1</sup>. We know much about single-neuron computations<sup>2</sup>, and have detailed insights into biochemical and biophysical processes that govern the internal operations within neurons<sup>3</sup>. Still, there is a gap between levels of understanding, where such knowledge has limited contributions. A hallmark of brain systems is that individual neurons are heavily connected to other neurons. Cortical circuits consist mainly of principal cells that have on the order of 10000 inputs, and 1000 outputs, which in lieu of the number of neurons that exists in brain systems becomes an astonishingly interconnected network. Systems with abundant feedback can be notoriously unstable or unpredictable. Considerable amounts of feedback in a system typically removes the system dynamics from a linear domain where inputs are 'orderly' correlated with outputs, into nonlinear domain where even microscopic perturbations can amplify and completely change the system's trajectory. With nonlinear dynamics comes very rich system behavior, but leaves even the simplest of underlying mechanisms often hopelessly shrouded.

## 1.1. Social anthropology of neurons

The study of social anthropology considers the interactions between individuals and sociocultural dynamics. It is said that the smallest focus, the atom, of social anthropology is not the individual, but rather the interaction between two individuals. In many ways, this summarizes an experimental focus that is becoming increasingly adopted among current neuroscientists. The mind is not in the neuron, but the interactions between neurons. As such, many of the brain's computations are embedded in population representations and dynamics, and our understanding can benefit from investigations on this level. David Marr proclaimed 3 distinct levels of understanding that brain systems need to be analyzed within: the computational, the algorithmic and the physical levels. With current technical and conceptual momentum perhaps being stronger than ever, we are asking questions that have answers spanning these levels.

## 1.2. The importance of behavior

A large focus of systems neuroscience has been to understand input-output transformations, especially in sensory systems<sup>4</sup>. While this approach has produced some of the greatest leaps in our understanding of the brain so far, it is often without much consideration for intrinsic context. All neural computations are set in a rich internal neural activity context. Computations are behaviorally relevant, which is reflected in the internal state<sup>5</sup>. Behavior (including sleep) is associated with highly specific neuronal- and population-states<sup>4</sup>, which are not feasible to successfully reproduce *in vitro* or anaesthetized animals. And while outward behavior is the direct consequence and purpose of many forms of neural activities, behaviors are complex themselves and often associate with a crowded variable-space. An appropriate system for these pursuits would perform core circuit operations, but with readily available, low dimensional behavioral correlates. Such a system is offered by studies in hippocampal and parahippocampal cortices.

## 1.3. Keeping space in mind

### 1.3.1. The cognitive map

Edward Tolman published 'Cognitive Maps in Rats and Men' in 1948, within which he argued for the existence of a cognitive map<sup>6</sup>. The reasoning behind this was based in part on the finding that animals, when having learned to traverse a meandering maze route to find a food reward, picked the right shortcut when presented with several alternative routes and not the original route, even if the rat had not occupied that space before. This, he argued, meant that the animals had a representation of space, a cognitive map, from which the shortcut could be computed. This line of reasoning was different from the contemporary and dominant behaviorist view in which behaviors were learned as chains of stimulus-response associations.

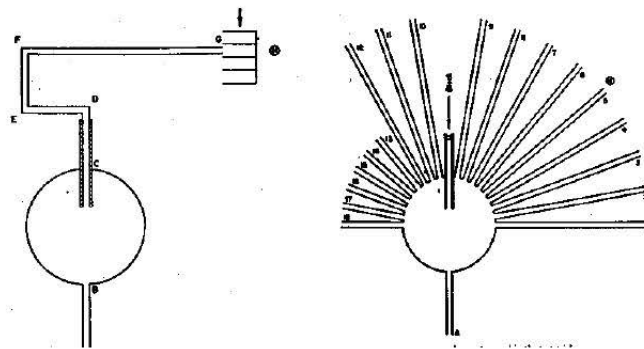


Figure 1. Tolman's experimental apparatus. Rats learned a tortuous maze route (left). When confronted with all new arm choices, the rats consistently picked the arm that was the shortcut (denoted by black dot). From ref <sup>6</sup>.

### 1.3.2. The neural map

The hippocampus is located deep within the medial temporal lobe and is an evolutionarily ancient type of cortex, archicortex, which has a very distinct architecture compared to neocortex or allocortex<sup>7,8</sup>. It does not feature the 6 layers associated with neocortex, but instead has 3, only one of which contains principal cells. There are subregions, which are characteristically connected. The dentate gyrus provides input to the CA3, which provides input to the CA1, which then provides output from hippocampus (see figure 2). This connection is referred to as the trisynaptic loop as information starts and ends in the same structure outside hippocampus (entorhinal cortex), and the information flow is more or less one-directional. This view is of course shamefully simplistic (see <sup>9</sup> for a comprehensive review), but it nonetheless highlights some features of hippocampal organization that has important bearing on functional considerations.

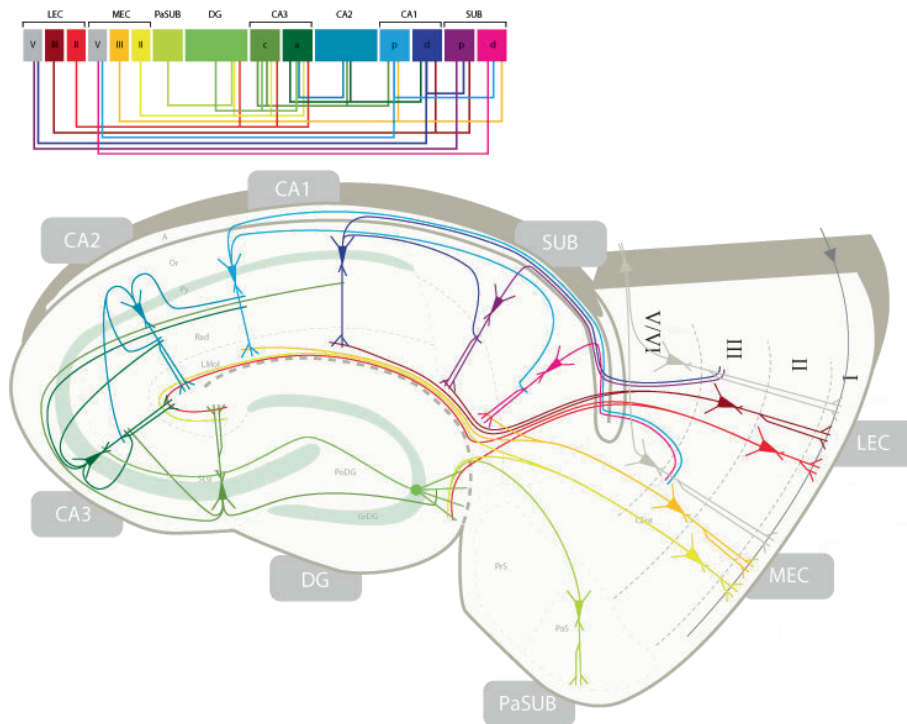


Figure 2. Overview of main connections to and from as well as within the hippocampal circuit. LEC: lateral entorhinal cortex, MEC: medial entorhinal cortex, PaSub: parasubiculum, DG: dentate gyrus, CA3: Cornu Ammonis 3, CA2: Cornu Ammonis 2, CA1: Cornu Ammonis 1; SUB: subiculum

Although hippocampus had been rigorously implicated in memory function<sup>10-13</sup>, there was an entirely new branch of neuroscience that opened with the discovery of hippocampal place cells<sup>14,15</sup>. Place cells display low firing rates on average, but within tightly delineated areas of an environment, their firing rates drastically increase. This location, the spatial receptive field, or place field, was seen early as a possible candidate for the neural implementation of the cognitive map<sup>15</sup>. Darwin had already formulated suspicions that the ability of animals (including humans) to navigate using 'dead reckoning' was based on some localized brain structure<sup>16</sup>. Dead reckoning refers to what we more commonly call path integration<sup>17</sup>. This is the ability to keep track of spatial location using self-motion cues, instead of landmarks (piloting). As the name suggests, the self-motion cues allow integration of movement vectors that make up a journey (as with Tolman's rats that picked the shortcut). Such self-motion cues, in neural terms, likely correspond to motor efference (or proprioceptive feedback) with information about movement distance, heading direction conveyed through vestibular systems, and such features as optic flow. There is abundant evidence that place cells can derive spatial constancy through either self motion cues, sensory cues or a combination<sup>18-25</sup>. Furthermore, place cells areas were intimately linked to memory<sup>12,26-30</sup>.

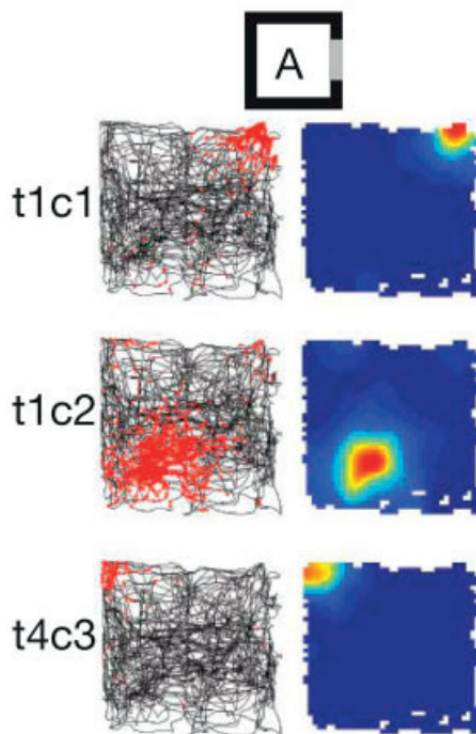


Figure 3. Place cells recorded in hippocampal subarea CA3. Top: recording box layout. A polarizing cue card is positioned on the eastward wall. Left: Bird's eye view of 3 place cells' activity (red dots) on the rat's recorded path (black). Cells were recorded simultaneously. Right: pseudo-color activity maps of the cells to the left. Red is high firing rate, and blue is no firing.

### 1.3.3. Going upstream

In trying to understand which incoming signals could take part in generating place responses, both experimental and theoretical suggestions were presented<sup>14,31-34</sup>. An important clue came from Brun et al<sup>35</sup> who showed that place cells in CA1 could sustain place characteristics even faced with ablation of its assumed critical input CA3. This suggested that place responses in CA1 originated from the other major input, medial entorhinal cortex (MEC). In pursuing this possibility, it was revealed that neurons in MEC were also spatially selective<sup>36,37</sup>, although typically with several fields. Shortly after, when the recording environment was enlarged, the spatial cells in MEC were revealed to be spatially selective in a near-perfect hexagonal grid of firing fields tessellating the entire environment<sup>38</sup>. Each grid cell has a slightly different x,y-coordinate in the environment, so that they cover the entire environment space collectively. Dorsally in MEC, grid patterns typically have small fields packed densely together, while with increasing distance ventrally, the grid pattern scale increases.

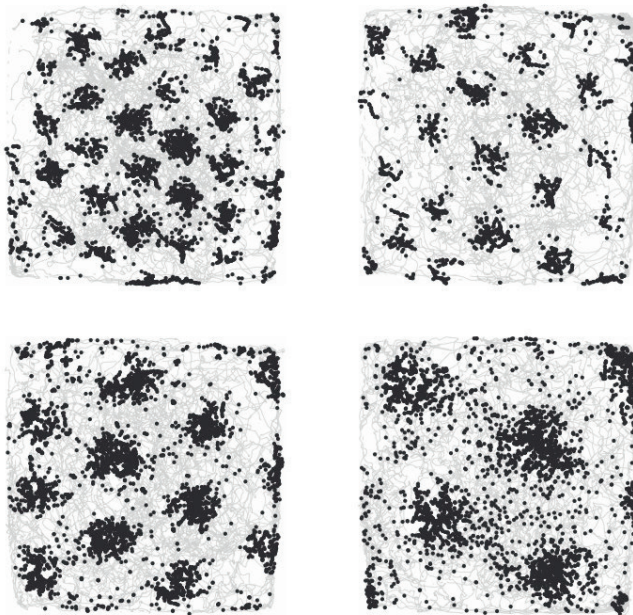


Figure 4. Grid cell firing patterns, birds eye view. Action potentials (black) superimposed on the rat's movement path (gray) reveal a tiling spatial activity pattern. Shown are grid patterns of 4 distinct scales recorded within the same animal.





## 2 Objectives

---

### 2.1. Functional organization of the entorhinal grid map

Several models<sup>33,39-43</sup> and lines of evidence<sup>35,44-46</sup> point to grid cells as prime candidates in conferring spatial selectivity to place cells in downstream hippocampus. Models that describe possible grid-to-place transforms are dependent on how the grid map is organized on several functional levels. Grid spacing distributes with topography along the dorsoventral axis of medial entorhinal cortex<sup>36,38,47</sup>; grid spacing increases with more ventral locations. Despite initial reports<sup>48</sup>, it was unclear if grid scale within animals distributed as a scale-continuum or instead progressed in steps. To answer this question, it is essential to record large numbers of grid cells from within considerable dorsoventral distances within animals, as to sample a sufficient range of grid spacing. It is necessary to record with minimal discontinuity in the tissue so that steps in spacing are discernable from discontinuous sampling of a smooth topography.

Grid orientation was in initial reports always similar<sup>38,49</sup>, suggesting there was only one shared orientation within the circuit. The existence of orientation configurations across scale has implications for grid-to-place transforms, but highlights a more basic question. Is the grid map composed of smaller sub-maps, or does it act as one coherent representation of space, but with distinct geometric features such as spacing? Hippocampal remapping, the orthogonalization of population encoding of space between environments, demonstrates a system with great capacity for distinct representations. A grid map with independently functioning sub-maps may produce unique population pattern-combinations for every environment, resulting in unique input patterns to place cells, and in turn, unique hippocampal output<sup>49</sup>. A major objective was therefore to determine if grid cells within the same grid circuit could perform separate operations on the same inputs, which we explore in Paper 1.

### 2.2. Functional organization of the entorhinal head direction system

The entorhinal cortex contains a circuit for spatial representation that is not restricted to grid cells<sup>50,51</sup>. Head direction-selective cells are found in intermediate and deeper layers<sup>51,52</sup> and are believed to contribute to grid and place cell function. Given the functional topography of grid cells within the medial entorhinal cortex, and that principal cells in this region expresses ion channel gradients<sup>53,54</sup>, we hypothesized that functional topography could be a general feature of entorhinal circuits, and would therefore also be

present in the head direction population. In addition, current models describe similar mechanisms underlying the two functional classes<sup>17,34,55</sup> in which case the similarities of underlying dynamics may produce similar functional characteristics on the population level. However, multiple upstream areas contain head direction cells<sup>52,56</sup> from which entorhinal cortex could inherit this representation, in which case population characteristics may differ fundamentally from other entorhinal cell classes. To establish the presence of a topographic distribution, large data sets are necessary, as well as sampling across considerable extents of medial entorhinal cortex, within the deep/intermediate layers, which is a challenging technical feat. These ideas, questions and issues were the focus of Paper 2.

### **2.3. Environmental features that control grid anchoring**

There are no hexagonal features in the environment that correspond to the grid pattern representation. Grid patterns are believed to arise from local network dynamics but driven by self-motion and sensory inputs<sup>33,39,41,57,58</sup>. For the grid pattern to be useful in allocentric representations it must anchor to external context; allocentric representations are context-dependent. It is not known how the grid anchors to context. Several possibilities exist that involve anchoring to salient sensory cues in the environment, such as visual or olfactory cues, or to the features of the environment itself. Cells that encode environment borders have been described<sup>50,59</sup>, providing a possible direct cellular link between grid cells and geometric features from the environment. We investigate these questions in Paper 3.

## 3 Synopsis of Results

---

### **Paper 1 | The entorhinal grid map is discretized**

Locally, grid cells behave as a coherent ensemble<sup>49</sup>, but it was unknown if the entire grid map functions as a coordinated whole or is fractioned into sub-units that display capacity for independent function. By combining novel and established experimental approaches we were able to record unprecedented number of grid cells within animals. This allowed us to determine that the grid map is a conglomerate of several sub-maps or modules. Such modules were composed of cells that all shared several functional features.

The gradient in grid pattern scale (grid spacing) along the dorsoventral axis of MEC that was established in earlier works<sup>36,38,47</sup> was found to progress in clear steps rather than a continuum within animals. All cells within a module shared the same grid spacing, and modules of increasing scale distributed with increased ventral distance along the dorsoventral axis. Cells that shared the same grid spacing within animals also shared grid orientation, the relative alignment of the pattern axes to the environment. We further found that modules within animals could differ substantially (see also ref<sup>60</sup> for a contemporary account); orientation distributed with tightly delineated clusters up to 30° apart, which, because of six-fold symmetry in the grid pattern, is maximally different. We next demonstrated that the grid pattern displayed systematic deformations, which were particular to each module. The deformations were detectable as ellipses in the distribution of fields in spatial autocorrelograms, and could vary substantially within animals, both in terms of direction (ellipse tilt) and amount (ellipse eccentricity).

Grid cells are tuned to the ongoing population activity, manifested as oscillations in the local field potentials<sup>61,62</sup>. Several models implicate the ‘theta’ rhythm in grid function (see<sup>63</sup> for review). It was known that cells along the dorsoventral axis oscillate with a slower beat frequency than dorsal cells, thought to arise from gradients in the expression of specific ion channels<sup>53,54,62,64–66</sup>. We found that grid cells within geometrically defined modules were also modulated by the same frequency. On average, modules with greater grid spacing had lower theta frequencies, but within animals, modules were not strictly confined to this trend.

The consistency of geometric features within, but not across modules made it possible to define module membership for all the cells with an automated multidimensional clustering approach (K-means clustering), thus removing experimenter bias from this process.

After defining the modules, we could turn to the question of how modules were distributed in the tissue. Several signs of anatomical clustering exist within the entorhinal system<sup>67-69</sup>, pointing to anatomical substrates for the functional clustering. Modules occupied extensive portions of MEC. We found that on average, a module spanned >1mm in the dorsoventral axis. There was extensive module-overlap in the tissue such that at any one location, cells from several modules could be present. Grid modules were found to cut across layers; cells that were part of one module were found in several layers. In contrast to the dorsoventral axis, there was no discernable topography along the mediolateral axis. Instead, modules extended across large mediolateral distances (~1 mm which was the limit of our recording equipment), suggesting modules distribute as mediolateral bands along the dorsoventral axis. With this knowledge, combined with the distribution pattern of modules in the dorsoventral axis, we could estimate the number of distinct modules within animals to likely be in the upper single-digit range. This anatomical distribution of modules does not match any known anatomical clustering in the entorhinal cytoarchitecture.

With previous reports having suggested a set relationship between scale steps<sup>48</sup>, we investigated the relationship between module scales within and across animals. Within animals, there was considerable variation in the relationship between one module scale and the next, suggesting scale is set independently for each module and animal. However, when we pooled the scale progressions, a pattern was revealed. On average, modules across animals increased by a fixed scale ratio, as a geometric progression. The ratio was 1.42, very close to  $\sqrt{2}$ . This relationship pointed to underlying genetic or circuit-mechanisms playing a role in setting grid scale, yet the geometric individuality of modules suggested that modules enjoy a substantial level of autonomy.

In the final set of experiments, we tested if grid modules are also functionally independent. Grid cells are known to rescale along with environmental compression<sup>48,50</sup>. When animals were exposed to a relocation of one of the walls in the environment, modules rescaled along the compression, but to varying degrees. Cells within a module behaved coherently, while individual modules could rescale to completely different

extents within animals. This provided the first proof-of-principle for independent function within sub-populations in the grid map.

The findings contained in this work have implications for hippocampal coding, which occurs one level downstream of grid cells, as well as for models of how the grid pattern emerges within the grid circuit.

### **Paper 2 | Topography of head direction cells in medial entorhinal cortex**

Grid cells distribute topographically with increased grid scale at increased ventral locations in the medial entorhinal cortex<sup>36,38,47</sup>. Along the same axis, expression of particular protein channels was found to distribute as a gradient with expression tapering off towards one end<sup>64</sup>. This gradient associates with changes in response properties of neurons, for example by altering time constants in afterdepolarization- or afterhyperpolarization events<sup>53,54</sup>, and has been shown to impact on properties of the grid pattern such as pattern scale<sup>65</sup>. Within the same circuit, medial entorhinal cortex contains cells that are head direction-selective. It is likely that such head direction cells also express the gradients of particular ion channels. We sought to determine if head direction cells distribute with functional topography, similar to grid cells, along the dorsoventral axis of medial entorhinal cortex. Grid modularity may arise from network dynamics rather than from direct physiological bases. If head direction tuning was topographic, we also asked whether this topography was continuous or modular in nature.

Animals were implanted with microdrives carrying tetrodes parallel to intermediate-deep layers within medial entorhinal cortex. The tetrodes were advanced systematically to allow sampling along extensive dorsoventral strips of tissue, gathering large data sets within animals.

Head direction cells in layer 3 distributed with clear topography along the dorsoventral axis. At dorsal sites, a considerable proportion of cells were strongly tuned such that spikes were elicited only when the animal's head was within a very narrow angular segment. At more ventral sites, however, tuning was on average broader. This was not an effect of decreased head direction cell distribution at more ventral sites; angular tuning stability and shuffling procedures were used to verify consistent head direction tuning despite broad tuning width. However, head direction tuning varied substantially

at all dorsoventral levels, such that the topographic decrease in tuning width was a gradual drop-off of sharply tuned cells toward ventral portions of medial entorhinal cortex. No topography was present in layers 5-6; head direction tuning was similarly distributed at all dorsoventral levels. There was also a distinction between head direction cells in layer 3 in medial entorhinal cortex, and in the neighboring parasubiculum. Cells in parasubiculum did not show any topographic reduction in tuning width with depth, but instead contained sharply tuned cells at all levels. As with grid cells, no topography was found in distribution of head direction cells in any layer along the mediolateral axis of medial entorhinal cortex. These point to a specific functional difference in head direction modulation within entorhinal layer 3.

To determine if the tuning topography generalized across species, mice were implanted with tetrodes and head direction cells recorded in medial entorhinal cortex. The head direction tuning topography was present also in this species pointing to a general organizational feature. Unlike tuning width, tuning directional phase did not distribute systematically. Instead, phases were uniformly distributed across recording depths, both in rats and mice.

Finally, we investigated if directional tuning topography was continuous or modular. In the same animals as we recorded the head direction data sets, grid cells were also recorded. These displayed modular features as shown previously, and had high scores on a 'discontinuity' measure sensitive to clustered topographical distributions. Across animals, head direction topography produced consistently low discontinuity values. This smooth nature of the head direction tuning was in stark contrast to grid spacing recorded in the same tissue. Lastly, we performed simulations to establish the robustness of discontinuity analyses, which supported a legitimate difference in modularity between grid and head direction populations.

Head direction cells thus distribute with smooth tuning topography along the dorsoventral axis of layer 3 in medial entorhinal cortex. The existence of functional topography in several cell classes suggests this may be a general feature in the entorhinal space-circuit, but that select sub-populations express modularity. This distinction may result from separate network dynamics inherent to entorhinal cortex, or from whether the functional tuning is generated within entorhinal cortex itself or inherited from upstream areas, a plausible candidate for entorhinal head direction cells given the wealth of directionally tuned inputs it receives<sup>56</sup>.

### **Paper 3 | Geometric features of the environment determine grid orientation**

Grid patterns are thought to emerge from local pattern-generating processes rather than by direct extraction from inputs. To achieve spatial constancy, however, such internal patterns must anchor to an external reference frame, the mechanisms by which are unknown. Several features of the pattern can be involved in this anchoring, including spatial phase (offset in the x,y-plane), grid spacing and grid orientation (alignment between grid pattern axes and environment features). We demonstrated earlier that grid orientation can assume distinct orientations across and within animals, but it was unknown whether there is any orderly relationship between grid alignment and environment features.

We compared grid orientation from large data sets recorded in two distinct square environments enabling rigorous analyses of grid alignment. Grid orientation did not distribute randomly across animals. Instead, there was a strong tendency to align to the cardinal axes of the environment, and avoid the oblique axes. In one environment, we observed clustering around one axis only, while in the other environment around both cardinal axes. The strong bias by axes in the box suggested the box geometry itself acted as the grid-anchor, not salient extra-environmental visual cues, which were deliberately abundant.

Rather than aligning perfectly parallel to the box axes, cells were consistently offset by a small amount across environments. In one environment, this offset was to either side of one cardinal axis. We demonstrated that these offsets reflected the same general alignment strategy, only as mirror-versions reflected around the same environment axis. In the second environment, cells were also offset from parallel, but to both cardinal axes. We found that these were in fact rotated versions of the same general anchoring strategy. Further, the offset was identical across the two environments; cells were systematically offset parallel by  $7.5^\circ$ , yielding four general alignment configurations within square environments. We next asked whether the observed distributions were a result of pooling all the cells, or if individual grid modules expressed the same alignment configurations. Modules from different animals expressed the same few configurations; cells were offset parallel by  $7.5^\circ$ .

We noted that a triangular pattern within a square is maximally asymmetric at  $7.5^\circ$  rotation in relation to the axes of symmetry in the square, the same as the offset observed in the data. We asked whether the consistent offset could confer a particular

function in spatial encoding within the square environment. The environment axes are primarily available to the animal in the form of borders imposed by environment walls. Because border segments have been implicated in spatial coding<sup>31,32,70</sup>, and as cells exist that encode these specifically<sup>50,59</sup>, we hypothesized that one function performed by grid alignment is to create maximally distinct population codes along environment border segments. Further, this may be a relevant strategy for encoding an environment in which sensory input may be confusing. Grid cells are thought to perform path integration (dead-reckoning from integration of distance and angle over time) from self-motion cues. Without sensory input, however, small errors will accumulate to some point where the representation becomes wholly unreliable. Sensory cues affect grid cells<sup>38,71</sup> and are thought to provide update signals that recalibrate path integration and reset accumulated errors. The symmetry and geometric ambiguity of the square recording environment may render such sensory cues less useful because similar relative location in the environment may produce similar update signals despite being at distinct absolute locations. Therefore, the most distinct population grid representation of border segments may contribute to reduced erroneous sensory resets.

By simulating grid population representations of square environments, we could systematically vary grid orientation (and spacing) and gauge the effect this had on segment encoding. We calculated population vectors for all spatial bins in the simulated square maps. We then determined the correlation such population vectors had between distinct border segments. The resulting correlation values showed lowest segment correlation occurred at 7.5° offset parallel, exactly like the observed distributions. The simulations also revealed a complex possible relationship imposed by grid spacing on the effect of grid orientation on decorrelating border segments. The same relationship was present in the experimental data suggesting it captured a fundamental structure behind the distribution of grid orientation.

These findings demonstrate that grid anchoring involves highly specific alignment to geometric features of the recording environment, universally expressed across animals. Simulations suggest that producing maximally distinct border segment encoding may be at the heart of this anchoring strategy.



## 4 Discussion

---

Since its discovery with the description of place cells<sup>14,15</sup>, the cortical circuit for spatial representation has revealed a wealth of functional systems, each dedicated to highly specific aspects of spatial processing<sup>38,50,52,56,59,60,72</sup>. The close relationship between memory and spatial processing<sup>10-12,26,27,29,73,74</sup> allows probing relatively abstract concepts such as memory formation and retrieval, consolidation and representational dynamics to be explored by very accessible experimental means, often little more than an animal's location and movements in space<sup>48,75-77</sup>. This connection provides an experimental system that performs computations at the highest level, yet remains one of the systems with best readout for experimental analyses and intervention. By studying core mechanisms such as navigation and memory, key concepts and insights into systems function and organization are available, and often with considerable generality to other cortical systems. As an example, by careful training and manipulation of sensory cues, rats could be manipulated to 'teleport' (neurally) between two environments<sup>78</sup>, manifested as abrupt transitions between place cell population representations for the two rooms. The study showed such population activity follows competitive attractor dynamics at very fast time scales and revealed that single cycles of a local oscillation acted as a minimal representation packet. The finding has far-reaching implications for network function and our understanding of the dynamics of representations in general. It emphasizes the power of the spatial-systems approach, and stresses the need and advantages of careful behavioral observation in conjunction with high-yield data-collection, such as *in vivo* electrophysiology. These concepts are at the core of the work presented in this thesis. After optimizing recording approaches, we could sample unprecedented numbers of grid cells and head direction cells within animals, which in conjunction with behavioral observation allowed characterization of novel principles that govern the organization of populations in MEC.

We showed that the grid map is composed of modules that have distinct grid geometry, temporal dynamics and response properties to environmental manipulation. We further demonstrated that head direction cells in MEC also distribute with feature topography along the dorsoventral axis, but that this was specific to MEC layer 3. Finally, the grid map was shown to anchor systematically to geometric features of the environment across animals revealing a universal alignment strategy.

## 4.1. Grid modularity: implications for downstream computations

### 4.1.1. Place field generation

Grid cells have been singled out as a particularly strong candidate for conferring spatial selectivity in downstream hippocampal neurons<sup>17,35,36,38,41,51</sup>. It seems appropriate that the interference patterns of cells across spatial scale could sum to produce punctate fields in hippocampus, as has been shown theoretically<sup>33,40,41,79–82</sup>. How the grid map is organized in terms of pattern geometry, map anchoring and population behavior can therefore inform us about coding strategies or bounds in hippocampus.

A simple but intuitive grid-to-place model<sup>40</sup> suggests that place fields originate from the summed activity of multiple grid cells with aligned spatial phase (field overlap) across scale. Phase-alignment between the grids causes extensive input at a tightly delimited spatial location, and while the regularities of the grid pattern may result in regularities also in the place cell, a high peak to background ratio could in principle provide masking of extra-place-field activity by feed-forward inhibition<sup>17,40</sup>. This strategy, however, is sensitive to geometric distributions in the grid map across scale. For optimal peak to background grid summation, grids should not cluster around particular orientations, because the overlap of axes across scale results in spokes of high activity. Similarly, grid scales with non-integer-scale ratios are favored because integer ratios result in periodic field-overlap.

In Paper 1, we show that grid modules assume irregular grid spacing ratios within animals. However, on average, when pooled across animals, the module pair relationships from within animals clustered around a mean ratio that was the same whether the module pair expressed smaller or larger spacing. This common scale ration was very close to  $\sqrt{2}$ , which results in scale doubling every other module. This particular scale arrangement would likely cause considerable regularities from pattern overlap outside a place field location, although this could perhaps be ameliorated by each spacing having a particular grid orientation allocated. We found in Paper 1 that although grid cells can assume widely differing orientations, the norm was to be closely aligned across scales (see figure 5). We further showed in Paper 3 that there exists an underlying strategy shared across animals to align the grid pattern to one of only four general configurations in relation to the environment geometry.

Together, this speaks against a grid-to-place transform based on field overlap from grid cells with aligned spatial phases across scales. Instead, other models have been proposed in which the downstream area plays an important role in distributing place characteristics based on non-coordinated inputs<sup>79-81</sup>. Here, local dynamics, such as competitive interactions and learning, delegate the spatial location with which each cell is associated, making input regularities less problematic<sup>81</sup>.

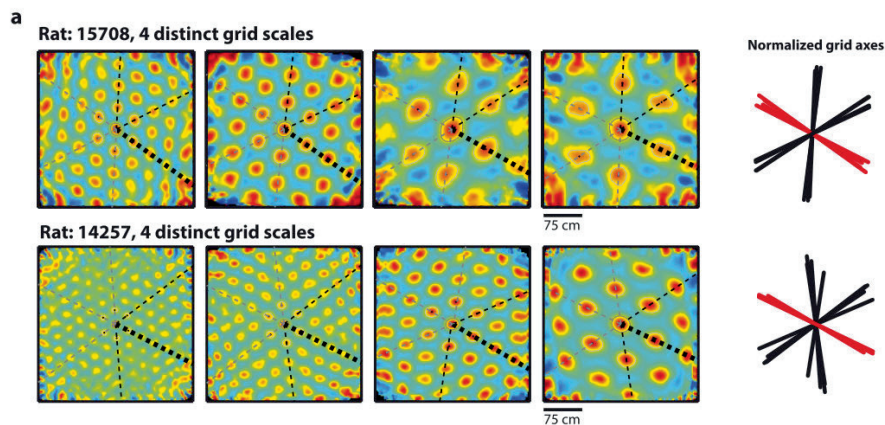


Figure 5. Spatial autocorrelograms from representative cells belonging to 4 distinct modules (left to right) in two different animals (top to bottom). Grid orientation was very similar across all modules within (and across) animals. From Paper 1 (supplementary figure 6). Extracted grid axes shown on right.

Other models exist that take into account different features than grid activity in generating place responses<sup>70</sup>. Cells that encode relationships between the animal and environment boundaries exist in entorhinal cortex<sup>50</sup>, as well as head direction cells<sup>51-52</sup>. It was recently shown that hippocampal place cells not only receive functional input from entorhinal grid cells, but also both these classes (and non-spatial cells)<sup>45</sup>. Place cells may very well get their place selectivity from composite contributions that encompass multiple cell classes and dynamics. If place cell formation does not necessitate the specific geometric features of grid modules, what is their function? We observed considerable evidence for independent module operation (see also section 4.1.2). This suggests, despite the intermingling of modules in the tissue, that modules are segregated connectivity-wise. As such, the translation of module grid patterns in relation to actual

movement may be driven by the same signals (e.g. velocity and directionality signals), but associate with independent noise. Multiple lines of evidence point to the grid pattern arising from local pattern-generating dynamics in which pattern translation from spatial translation is driven by amongst other path integration signals<sup>57,58,83-85</sup>. Such pattern-formation mechanisms can generate noise (and error accumulation) that is more dependent on the local network dynamics than the input signals<sup>42,86</sup>. Therefore, independence of grid ensembles may confer a signal parallelization with signal-to-noise improvement, as each module will share the translation signal but not system noise. Common noise or error in the driving signals themselves will necessarily not be different, and may instead need to be overcome by other means such as sensory resets.

#### **4.1.2 Place cell remapping: basics**

In a landmark paper, Kubie et al<sup>76</sup> described a phenomenon that had great implications for our understanding of the relationship between the spatial map in hippocampus, and its role in memory formation. For one, they demonstrated that place cells are under the control of sensory cues in the environment as rotation of a cue resulted in consistent rotation of the place cells' activity. More importantly, they demonstrated that given discrepancies of sufficient magnitude between two recording environments, the activity of the recorded cells changed drastically; of the cells that were active in the first environment and stayed active in the second, the firing locations were completely reorganized in space. Further, a large portion of cells active in one environment became silent in the next. This functional reorganization was termed 'remapping' and represents an orthogonalization in the population encoding between the distinct environments. The combinatorial capacity of hippocampal representations, given the number of cells, and their possible firing locations, is *very* large. This capacity for distinct population codes may lie at the heart of hippocampal encoding. Wilson et al<sup>74</sup>, using novel techniques, provided the first recordings of large place cell populations recorded simultaneously. They demonstrated that population representations are very accurate (<5 cm error from ~100 cells) and indeed minimally correlated between two environments. When exposed to a new environment, the representations of a familiar environment did not change<sup>74</sup>, supporting a coding scheme that allows independent and unique representations for each environment.

Grid modularity appears to offer very favorable conditions for hippocampal remapping. Maps from the different modules could reorganize to yield completely novel downstream population inputs, and therefore hippocampal place maps. Grid cells coherently realign with simultaneously recorded hippocampal place cells<sup>49</sup>. The realignment involved a shift in phase, and reorientation of the pattern relative the environment, and was coherent for all grid cells recorded, so that despite the realignment, spatial relationships between the grid cells remained<sup>49</sup>. This does not preclude independent realignment of distinct modules, as all the grid cells in this paper were recorded at the same dorsoventral location and had similar scale (very likely belonging to the same module). The authors of this work also suggest different scenarios for what the larger-scale population realignment configurations may be (see figure 6).

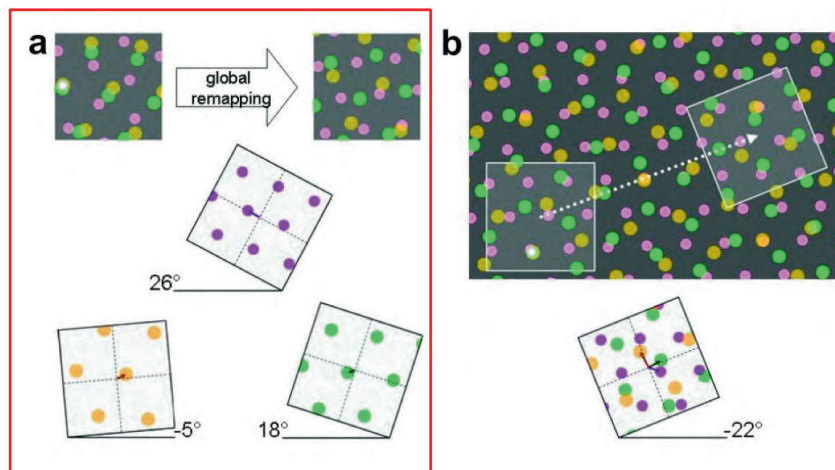


Figure 6. Proposal for two mechanisms that may underlie hippocampal remapping based on grid inputs. Left: several independent maps realign independently and cause unique combinatorial population pattern in hippocampus. Right: The grid map is coherent across scales, and remapping occurs from a shift in spatial phase space. From ref <sup>49</sup>.

Which features are important in modular realignment for hippocampal remapping? As discussed above (section 4.1.1), the geometric features of the grid follow certain constraints. As we demonstrate in Paper 3, modules typically assume one of only 4 distinct alignment configurations relative the environment. This constraint on orientation may seem highly disadvantageous for generating maximally distinct

hippocampal inputs. However, recently, it was shown theoretically that remapping based on grid modules was much more sensitive to the spatial phase offset between the modules than the relative orientation and spacing<sup>81</sup>. Varying grid orientation caused less reorganization in hippocampus compared to varying phase (see figure 7).

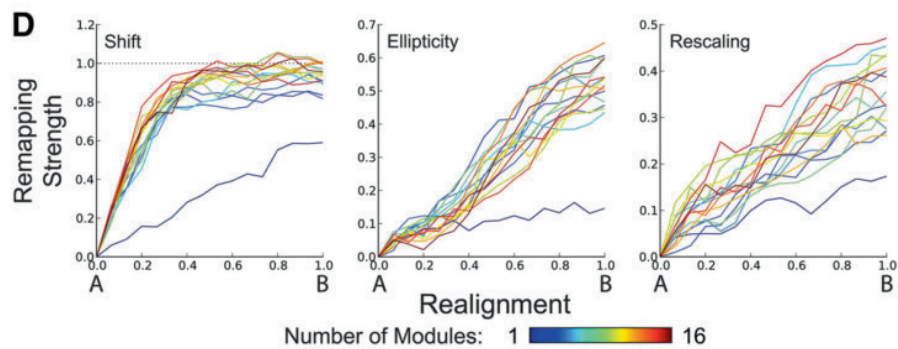


Figure 7. Efficacy of reorganizing different parameters of grid geometry between modules. The strongest remapping occurred from phase shifts, while other features were less effective. From ref <sup>81</sup>.

If grid modules are a main source of hippocampal remapping, the level of independence between grid modules will affect remapping-based mnemonic capacity. Do grid modules display independent operation? We show in Paper 3 that grid modules have several geometric traits that suggest autonomy. Grid spacing relationships varied across animals, and grid orientation could be completely offset between modules. In attractor models of grid cells, a grid network can only support a circuit in which all cells share pattern geometry<sup>42</sup>. Grid modules also differed in the amount and directionality of pattern deformation. Grid deformations had perhaps been observed before in the absence of environmental manipulation, but there was no telling this was not from systematic path integration errors affecting the whole grid map. Deformation, scale and orientation changed independently per module during exposure to a novel room (see figure 8). Together, these suggest independent geometry between modules. We also observed rescaling of grid module maps to compression of the environment<sup>48</sup>. Importantly, these were to distinct levels between modules in the same animals, but always consistent within modules. Further, it was always the modules of smallest spacing that rescaled minimally (kept the original node locations). It is unlikely that grid

rescaling was dependent on the wavelength of the grid pattern in relation to the environment size *per se* as there was no absolute threshold for which modules rescaled and which did not within animals recorded in the same environment. A caveat with more credence is the possibility that rescaling is dependent on wall anchoring rather than reflecting genuine coding differences. Absence of rescaling could occur from smaller grid cells not anchoring to the wall that is relocated during the environment compression, but rather to the opposing wall. This could render the relocated wall 'invisible' to that module. Conversely, if larger grid cells tend to anchor to both the relocated wall and the opposing wall, rescaling would occur. It seems unlikely that this is a full explanation, however, as we never saw a smaller module not rescale but move along the wall that was relocated. And nonetheless, there is still a functionally distinct output from these cells that is likely to cause reorganization downstream in hippocampus.

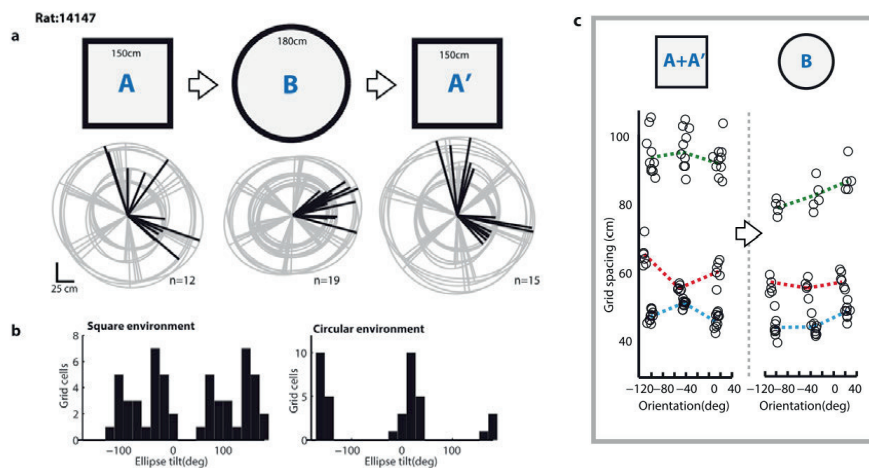


Figure 8. Modules realigned in response to a novel room and environment shape. Grid scale, orientation and ellipse directions all changed independently between modules strongly suggesting independent operation. The figure on the right shows data from all three grid-axes. From Paper 1 (supplementary figure 10).

The effects of such separated rescaling levels may be offered by an influential study on the effects of changing the environment geometry on place cells in hippocampus<sup>31</sup>. Place cells were recorded in an environment that could be extended or compressed in

any of the 4 cardinal directions. When the recording box was extended or compressed, place fields followed the environment changes, at fixed or relative distance from the environment boundaries. Some cells were anchored to one wall or set of walls so that they moved along the extension, others to other walls. Some cells were anchored to the room instead of the box, and others distended the place field along the room changes or even split fields into two. This behavior suggested an underlying input pattern with distinct geometric relationship to the walls of the recording box or room. The authors proposed a model to explain the results where spatial modulation arose from the sum of multiple Gaussian activity bands offset the environment boundaries at different distances<sup>31</sup>. This idea was further developed into the boundary vector model of place cells<sup>32,70</sup>. Although boundary selective cells exist in MEC and do project to hippocampal place cells<sup>45</sup>, this study is also intuitively in line with expectations from the above discussed results of grid rescaling. Because of rescaling, place fields can receive input that is topologically identical to the original map, only distended or compressed, likely resulting in distended or compressed place fields. In the case of two particular module inputs to a place cell, and the modules differed greatly in rescaling levels, it seems reasonable to assume that their contribution could be separated upon environment changes to break the place field into two separate components.

#### **4.1.3 Place cell remapping: attractor dynamics**

A study by Lever et al<sup>28</sup> used two recording environments that differed in geometry but had very similar layouts otherwise. There were very similar ensemble representations of these environments that first over time diverged into separate representations. It seems likely that the similarities in this study caused generalization, which was with time separated into distinct representations. In Paper 1, we recorded different cells from the same modules for long periods of time. What can be seen in these data are slow (on the order of days and weeks) graded changes in grid features. Moreover, these were distinct for each module and also for the individual grid axes (see figure 9). In the smallest module in the figure example below, there was a systematic positive relationship between recording session and grid orientation. During the same recording sessions, cells in the next module also expressed some graded changes, but much less than the first module and in opposite direction. Completely separate trends were present in the two modules. Such slow changes may underlie the effects seen in the Wills study. However, there are sharper and nonlinear transitions seen in hippocampal population responses to distinct environments.



Place cell ensembles have been shown to exhibit attractor dynamics<sup>78,87,88</sup>. Attractor dynamics involve noise-robust population representations of stimuli or states, in which the entirety of the original signal can be reproduced from only a subset of the original active cells. Such states are often mutually exclusive and exhibit competitive interactions. In Wills et al<sup>87</sup>, hippocampal place representations underwent a very abrupt and coherent transition from one place representation to another during a gradual 'morphing' from the one environment shape to the other. Leutgeb et al found similarly, that neurons in dentate gyrus and CA3 respond with sharp population changes upon graded changes in the environment. For grid cells to account for this effect, either it is due to rapid attractor kinetics in the upstream grid map, or small changes in the grid map that are nonetheless, through associations within hippocampus, enough to shift the current hippocampal activity into another attractor state. Upon grid realignment, we observed several dissimilarities in grid features across the two rooms, pointing to independent remapping. During rescaling to environment compression, however, only graded responses were found. It remains to be determined if graded transitions can cause similar transitions in grid cells.

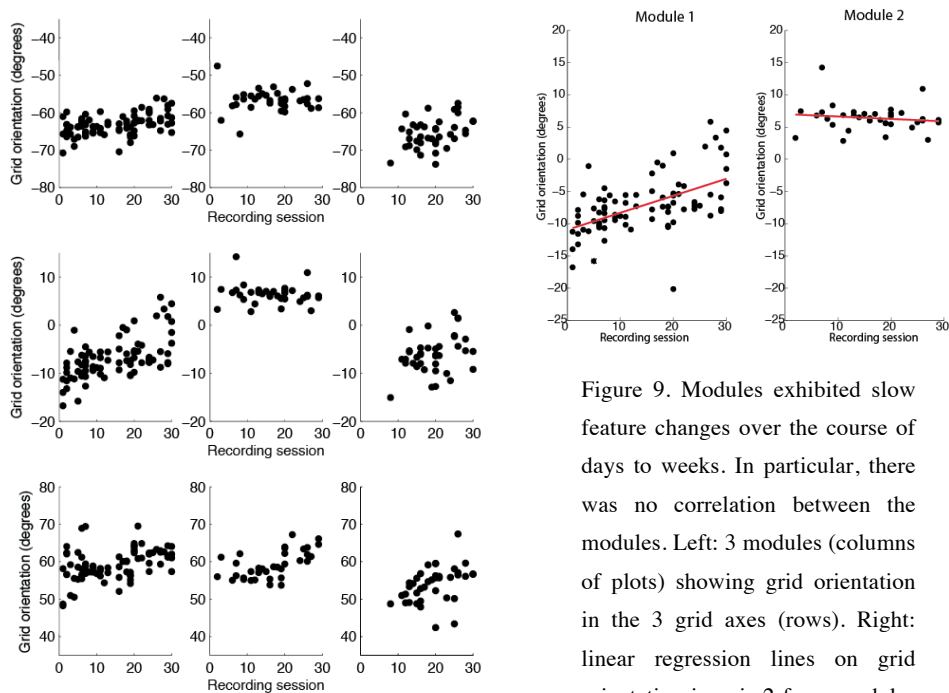


Figure 9. Modules exhibited slow feature changes over the course of days to weeks. In particular, there was no correlation between the modules. Left: 3 modules (columns of plots) showing grid orientation in the 3 grid axes (rows). Right: linear regression lines on grid orientation in axis 2 from modules 1 and 2 in left panel are highly distinct. Unpublished.

#### **4.2. Topography in the parahippocampal systems**

In sensory and motor cortices, there is typically a neat correspondence between relationships in the external world and their internal representations in the brain. That is to say continuous or discrete variables in the external world are mapped topographically into the cortical sheet<sup>89</sup>. Topography often represents a 'where' component onto which other information about stimulus quality can be superimposed<sup>7,8</sup>. There is an orderly correspondence between retinal receptor location and its representation in primary visual cortex. Likewise with the somatosensory system. In sensory and motor cortices, topographical strictness tends to lessen with increased distance from input/output organs (level in the cortical hierarchy). In hippocampus, which is very far removed from the senses and motor outputs, there are nonetheless reports of feature topography. What is this topography? The 'where' component topography of space may seem obvious to be space itself. Neither place cells nor grid cells display topographic representation of spatial location, however. In hippocampus, using 2-photon imaging, the activity of an entire ensemble of hippocampal place cells could be imaged simultaneously while the mouse navigated within a virtual environment<sup>90,91</sup>. The place cells developed clear place fields suggesting the task was not too alienating for the spatial representation system. Further, there was no statistical relationship between the location of place cells in the hippocampal cellular sheet (>35  $\mu\text{m}$  apart), and the locations of their place fields in (virtual) space. Cell pairs <35  $\mu\text{m}$  apart, displayed a significant correlation, but not separable from correlations from common neuropil or activity bleed-over in the imaging technique<sup>90</sup>. Grid cells do not show any relationship with the position recorded in the tissue and their spatial phase offsets<sup>38</sup>. Mechanisms by which topography is present during development as a teaching signal to set up appropriate circuitry for grid function, only to disappear in the adult brain, have been proposed<sup>33</sup>. It is worth noting that both hippocampus and entorhinal cortex are evolutionarily 'old', such that the orderly topography seen in typical low level cortex only likely arose after these structures were past their phylogenetic 'window of opportunity'<sup>18</sup>. Accordingly, the olfactory piriform cortex is another ancient cortical structure that does not show topographical organization even though continuity in stimulus dimensions exists.

However, place fields recorded on an 18m linear track formed punctate fields delineated within 15-20 cm diameter in dorsal hippocampus, while at the ventral pole the place fields could reach several meters across<sup>92</sup>. See also ref <sup>93</sup>. Similarly for grid spacing: dorsally, grid fields and their inter-field spacing is strict and on the order of a few tens

of cm. Ventrally, on the other hand, inter-field distances can cover several meters<sup>47</sup>. In Paper 2, we show that also head direction cells express topography in terms of the sharpness of their directional tuning.

What do these topographies reflect? There is a long literature on distinct features of dorsal and ventral portions of hippocampus. For instance, lesions to different dorsoventral portions produces markedly different behavioral deficits<sup>94</sup>. Lesions of a small portion of the dorsal pole impairs spatial memory efficiently, while similar portions of the ventral pole do not<sup>27</sup>. Stress responses and emotional behavior are affected by lesions to the ventral but not dorsal portions of hippocampus<sup>95</sup>. Connectivity to and from these portions of hippocampus is distinct<sup>30,96</sup>. Also in spatial cognition in humans is there a growing body of literature that suggests functional polarization along the human equivalent of the dorsoventral axis<sup>30,97</sup>. In particular, activity in ventral hippocampus (human equivalent) is associated with coarse global spatial representations and route planning and execution, while the dorsal equivalent fine-grained local representations and navigation strategies (such as number of turns on a route)<sup>98</sup>.

The neural codes used by the parahippocampal spatial system may very well reflect an axis of generalization. With increased scale of spatial fields in hippocampus and MEC, one coding aspect is that the larger fields do not denote spatial location with equal demarcation, so spatial resolution is diminished. However, another coding aspect is that for these ventral codes, at any particular point in space, a greater portion of cells will be active. This increased representational density may confer better robustness to noise; the more cells that can take part in a 'majority' vote, the better the vote will be statistically, despite poorer spatial resolution. It is interesting that the same exact argument can be made for the head direction gradient (see figure 10). Alternatively, ventral cells (both grid, place and head direction cells) code a bigger portion of the environment at any moment, so that the population code at any location is more generalized. This may be beneficial for associating different content into current spatial contexts. The ventral hippocampus is more associated with stress and fear responses, and has stronger connections to and from amygdala<sup>94,96</sup>. For embedding e.g. fear memories into spatial context, it may be strategic to impose a higher level of generalization. In Paper 1, we observed a functional dissociation between modules of small and large grid spacing. In particular, smaller grid spacing associated with little or no rescaling in response to the environment manipulation, while the largest cells always did. This could reflect an

underlying topographic distribution of spatial generalization, in line with the above suggestions.

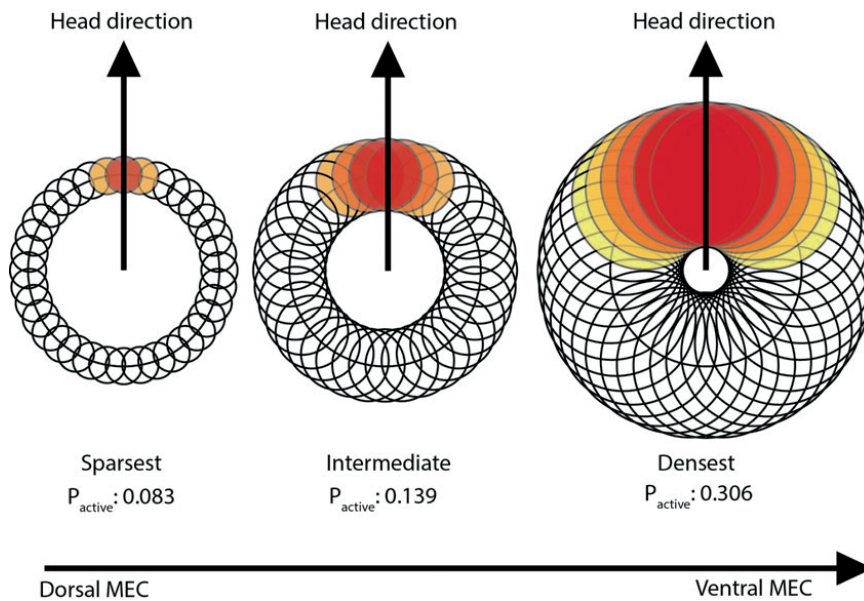


Figure 10. Head direction representational density increases with ventral position in MEC layer 3. Given populations of equal size (cells as rings of the doughnut; dorsal to ventral as left to right), and the same direction input, a different proportion ( $P$ ) of the cell population will be active.

### 4.3. A need to develop our understanding of grid spacing

We demonstrated that grid spacing increases in steps along the dorsoventral axis of MEC (see also <sup>48</sup>). Which factors determine topographical grid spacing is currently unknown. We failed to find a systematic relationship between module scales within animals; the scale distributions were tightly delineated but distributed irregularly. However, when all module pair ratios were pooled across animals, a consistent average scale ratio was revealed. This consistency across animals implicates a genetic component in determining grid spacing. Gradients of specific ion channels, such as the hyperpolarization-activated cyclic nucleotide-gated (HCN) channels, exist in entorhinal cortex, and have been suggested to account for the grid scale topography<sup>53,54,65</sup>.

However, such channels, when genetically knocked out, did not remove grid scaling along the dorsoventral axis, but instead changed the baseline spacing<sup>66</sup>. Other channel-gradients may contribute to scaling (such as potassium channels<sup>54</sup>). If scale is determined in part from channel gradients, or indeed any genetic expression patterns, it seems likely the gradient will provide a smooth topography of any conferred scale parameter, instead of modular. How could modular grid scale result from a smooth underlying gradient?

One possible scenario is that module grid scale is determined by network dynamics acting on an underlying scale parameter gradient. Attractor models of grid cells predict that all cells in a circuit must have the same grid spacing (as well as orientation and pattern deformation) to generate a stable grid pattern<sup>57</sup>. Within a grid network determined by attractor dynamics, there will likely be a some tolerance to small variations in the scale-parameter distribution across cells, so that when the network is initiated, the effects of population dynamics dominate individual cells enough to coordinate all cells into a common pattern, cancelling out individual variation. In a sense, this 'spatial synchronization' acts similarly to synchronization in the temporal domain; originally observed by Huygens in 1665, coupled oscillators settle on a mean frequency that entrains all the individual oscillators even in the presence of relatively large variations in individual frequencies. What would happen if the scale parameter distribution had very large spread? The variation becomes too big to entrain all units into one coherent pattern, and the pattern may fraction into sub-ensembles that each center on a mean frequency that the ensemble can sustain. This way, by having a network self-organize from a very wide, continuous scale parameter distribution (such as channel expressions along an axis in MEC), several local modules of internal spatial consistency could arise from the unstable global pattern.

However, in Paper 1, we observed convincing signs of independence between modules within animals, both in terms of pattern geometry and rescaling responses. To incorporate this in to the suggested mechanism above, one can suppose that during development, learning strengthens connections within spatially synchronized ensembles, but weakens connections between spatially desynchronized cells. Spatial synchronization will produce a consistent phase-offset between fields of two cells. If such cells have similar spatial phase, their coordinated firing in space will cause coordinated firing in time, a prerequisite for many forms of long-term potentiation (LTP)<sup>99</sup>. This way, ensembles intermingled in the same tissue could develop, with

strong inter-ensemble connectivity and weak cross-ensemble connectivity, in effect decoupling the ensembles functionally. A testable prediction from this idea is that very young animals, which have yet to achieve complete module decoupling, will display grid cells with poor pattern regularity because the network cannot sustain a coherent grid pattern on account of cross-ensemble interactions. As the animal explores more space, decoupling will at some point become complete enough that the modules can self-organize into modules with coherent and regular grid patterns. Such a transition may be rapid as it involves a 'tipping point' after which network dynamics kick in to entrain the ensemble. In two studies that characterized grid cells in early development in rats, grid patterns were indeed not very regular initially<sup>100,101</sup>. Instead, only after considerable time did regular grid firing occur. The transition to this state had rapid onset, in line with the above proposal.

Conversely, if the scale parameter is associated with temporal characteristics such as intrinsic resonance frequency, as is suggested by several models (see <sup>63,102</sup> for review) and experimental findings<sup>53,62,66</sup>, synchronization in the temporal domain during development could result in similar module fractioning and synaptic consolidation to cause *temporally* consistent ensembles. If the scale parameter associated with temporal frequency, these temporally synchronized ensembles would also become spatially synchronized. By this mechanism, grid modules could develop to fully or close to fully mature, functionally decoupled modules at least in part before the animal ever explores space. In line with this is our finding, also in Paper 1, that modules are temporally consistent. Cells within a module, as defined by pattern geometry, were more temporally consistent than cells across ensembles (even at similar recording locations and grid scale). The validity of these suggestions can be explored through modeling.

#### **4.4. Embedding internal representations into external frames**

The need to anchor internal representations of space to external frames is paramount for allocentric function. We demonstrated in Paper 3 that grids align to the environment in a very systematic manner. We also suggested that the particular configuration bore functional significance beyond grid-to-place transformations. In particular, we hypothesized that the alignment of the grid pattern could be used to counteract geometric confusion within geometrically ambiguous environments. Simulations showed that in square environments, the observed alignment offsets from the cardinal axes of the environment were in close register with the offsets that produced minimal

correlation between grid population encoding of border regions. Rats tested in spatial working memory tasks in rectangular environments make systematic errors in segments of the box that have rotationally equivalent geometry, even in the presence of polarizing cues<sup>103</sup>. This suggests geometric confusion is a common issue in spatial representation, as is supported by similar effects found in several other species<sup>104</sup>. We further hypothesized that border cells may provide the mechanistic link between the grid map and the external environment frame. Despite abundant visual landmarks in the recording rooms, modules with few exceptions aligned according to environment geometry. There may be a special salience given to environment borders, as opposed to visual cues, likely because environment borders are generally more dependable. Biegler et al<sup>105</sup> found that rats only used landmarks within an environment to gauge distances if the landmarks were stable within that environment. Several studies have shown similar connections to environment geometry<sup>18,24,71,106-109</sup>, but also highlighted the fact that the system's use of landmarks for spatial representation can be changed experimentally through learning<sup>20,21</sup>. The close match between observed alignment and that for optimally decorrelated grid population encoding of environment segments suggested to us that there could be a competitive interaction between path integration signals and sensory resets. Evidence for this comes from hippocampus, where Gothard et al<sup>22</sup>, and later Redish et al<sup>23</sup> described the rapid switching between navigation strategy according to path integration or landmarks. Rats started running from a start-box at the end of a linear track. As the rat was outbound, the box would be moved closer to the endpoint. On the inbound journey, place fields abruptly remapped to accommodate the visually apparent change, and switched back to a path integration strategy on the outbound journey. They showed signatures of competitive attractor dynamics supporting such an interaction between idiothetic and landmark based information<sup>22,23</sup>.

#### **4.5. Oblique effect in grids?**

Discrimination and detection of visual stimuli are dependent on the relationship of the stimulus to the axes of the environment, a well-known effect known as the 'oblique effect' (Mach 1861<sup>110</sup>). Stimuli oriented along the cardinal axes yield better psychophysical performance compared to obliquely oriented stimuli. In visual cortices, both single-neuron responses and population-responses reflect the psychophysical anisotropy by increased representational density along the cardinal axes<sup>111-113</sup>. Several studies suggest that the oblique effect originates in higher order cortices<sup>114-116</sup>, as the effect is stronger here compared to early sensory cortex<sup>116,117</sup>, and the effect in early cortex is selectively abolished by temporal inactivation of higher order cortex<sup>116</sup>. Grid

cells were typically aligned—close to—cardinal axes of the environment. Recently, it was shown that grid representations are not limited to navigational space; a grid map of visual space was demonstrated in the monkey entorhinal cortex<sup>118</sup>. Although highly speculative, it is interesting to ponder the possibilities for similar mechanisms at play in embedding internal representations into external reference frames in the visual domain as in the spatial domain. Although not very many examples were given in Killian et al, there seems to be also here a trend to align with slight offset to cardinal axes (see figure 1 in ref <sup>118</sup>). Further, using optical imaging in area MT (which shows movement and orientation selectivity for stimuli) in the visual system, Xu et al show frequency-plots of activation over the range of possible stimulus orientations. In these there are quite distinct peaks bimodally offset the cardinal axes. And at further inspection, these are very close to 7.5° offset, which is the exact peak we observed in the alignment offset in grid cells (see figure 11). This points to a possible albeit suppositional link between visual and spatial encoding in relation to real world axes, a link to be explored through future studies.

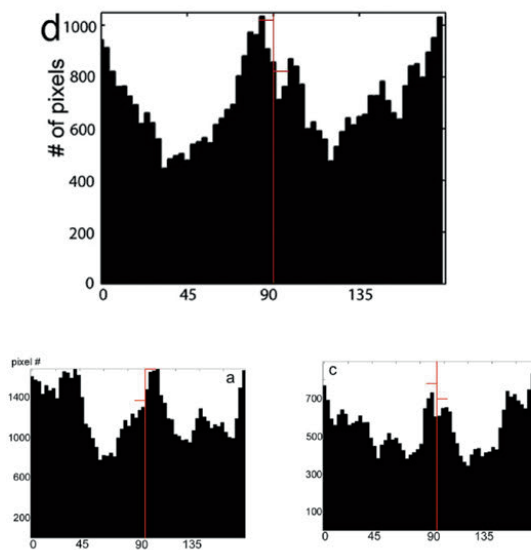


Figure 11. The oblique effect in visual area MT in the owl monkey. Histograms are modified from ref <sup>113</sup> (top panel: figure 3, bottom panels: supplementary figure 6). Histograms show local activity measured through intrinsic optical imaging. Increased pixel count (y-axis) corresponds to higher activation. The different panels are from distinct subareas within MT. The red lines show 7.5° offset calculated from the x-axis of the plots. Note the correspondence between peak offset and red lines.



## 5 Conclusions

---

Hippocampus and associated structures offer a good systems approach to understanding basic functions carried out by neural networks within a behavioral context. Our understanding of grid cells has been fruitfully developed on the single cell level, but has lagged behind the population insights gained from hippocampus. This has been to a large extent because of technical challenges given entorhinal cortex location in the rodent brain. With overcoming these hurdles, we have defined the first large-scale population characteristics of two central spatial encoding populations. The grid map was shown to be modular, with separate geometric features and operation. The head direction system has a topographic dimension similar to grid and place cells, but the head direction is non-modular. We finally showed a universal strategy grid modules use to anchor to the environment, implicating this strategy in optimal population encoding of ambiguous environment segments.

## **Legal and ethical aspects**

All animal experiments described in this thesis were conducted according to the Norwegian Animal Welfare Act (Lov om dyrevern, no 73 av 20. desember 1974) and the European Convention for the Protection of Vertebrate Animals used for Experimentation and Other Scientific Purposes.

The research laboratory is licensed by the national authority for animal research and satisfies the requirements for rodent units as recommended by the European Convention. The previous inspection of the animal facility was conducted 2012 and is valid through 2014.

All experimenters involved were certified through a compulsory course in laboratory animal science for researchers (NEVR8003 or equivalent).

All experiments were specifically designed to minimize the number of experimental animals used and to maximize the animals' wellbeing through continual inspection by the researchers, qualified caretakers, and the laboratory vet.

## References

1. Bargmann, C. I. & Marder, E. From the connectome to brain function. *Nat. Methods* **10**, 483–90 (2013).
2. Spruston, N. Pyramidal neurons: dendritic structure and synaptic integration. *Nat. Rev. Neurosci.* **9**, 206–21 (2008).
3. Kennedy, M. B., Beale, H. C., Carlisle, H. J. & Washburn, L. R. Integration of biochemical signalling in spines. *Nat. Rev. Neurosci.* **6**, 423–34 (2005).
4. Harris, K. D. & Thiele, A. Cortical state and attention. *Nat. Rev. Neurosci.* **12**, 509–23 (2011).
5. Vanderwolf, C. H. Hippocampal electrical activity and voluntary movement in the rat. *Electroencephalogr. Clin. Neurophysiol.* **26**, 407–18 (1969).
6. Tolman, E. Cognitive Maps in Rats and Men. *Psychol. Rev.* **55**, 189–208 (1948).
7. Montagnini, A. & Treves, A. The evolution of mammalian cortex, from lamination to arealization. *Brain Res. Bull.* **60**, 387–93 (2003).
8. Kaas, J. H. Evolution of columns, modules, and domains in the neocortex of primates. *Proc. Natl. Acad. Sci. U. S. A.* **109 Suppl** , 10655–60 (2012).
9. Van Strien, N. M., Cappaert, N. L. M. & Witter, M. P. The anatomy of memory: an interactive overview of the parahippocampal-hippocampal network. *Nat. Rev. Neurosci.* **10**, 272–82 (2009).
10. Squire, L. R. & Alvarez, P. Retrograde amnesia and memory consolidation: a neurobiological perspective. *Curr. Opin. Neurobiol.* **5**, 169–77 (1995).
11. Squire, L. R., Stark, C. E. L. & Clark, R. E. The medial temporal lobe. *Annu. Rev. Neurosci.* **27**, 279–306 (2004).
12. *The Hippocampus Book (Oxford Neuroscience Series)*. 872 (Oxford University Press, USA, 2006).

13. SCOVILLE, W. B. & MILNER, B. Loss of recent memory after bilateral hippocampal lesions. *J. Neurol. Neurosurg. Psychiatry* **20**, 11–21 (1957).
14. O’Keefe, J. & Dostrovsky, J. The hippocampus as a spatial map. Preliminary evidence from unit activity in the freely-moving rat. *Brain Res.* **34**, 171–5 (1971).
15. O’Keefe, J. & Nadel, L. *The Hippocampus as a Cognitive Map*. 584 (Oxford University Press, USA, 1978).
16. DARWIN, C. R. Origin of Certain Instincts. *Nature* **7**, 417–418 (1873).
17. McNaughton, B. L., Battaglia, F. P., Jensen, O., Moser, E. I. & Moser, M.-B. Path integration and the neural basis of the “cognitive map”. *Nat. Rev. Neurosci.* **7**, 663–78 (2006).
18. Knierim, J. J., Kudrimoti, H. S. & McNaughton, B. L. Place cells, head direction cells, and the learning of landmark stability. *J. Neurosci.* **15**, 1648–59 (1995).
19. Etienne, A. S. & Jeffery, K. J. Path integration in mammals. *Hippocampus* **14**, 180–92 (2004).
20. Jeffery, K. J., Donnett, J. G., Burgess, N. & O’Keefe, J. M. Directional control of hippocampal place fields. *Exp. Brain Res.* **117**, 131–42 (1997).
21. Jeffery, K. J. Learning of landmark stability and instability by hippocampal place cells. *Neuropharmacology* **37**, 677–87
22. Gothard, K. M., Skaggs, W. E. & McNaughton, B. L. Dynamics of mismatch correction in the hippocampal ensemble code for space: interaction between path integration and environmental cues. *J. Neurosci.* **16**, 8027–40 (1996).
23. Redish, A. D., Rosenzweig, E. S., Bohanick, J. D., McNaughton, B. L. & Barnes, C. A. Dynamics of Hippocampal Ensemble Activity Realignment: Time versus Space. *J. Neurosci.* **20**, 9298–9309 (2000).
24. Sharp, E., Blair, H. T., Etkin, D. & Tzanetos, B. Influences of Vestibular and Visual Motion Information Firing Patterns of Hippocampal Place Cells on the Spatial. **15**, (1995).

25. Fenton, A. A., Csizmadia, G. & Muller, R. U. Conjoint control of hippocampal place cell firing by two visual stimuli. I. The effects of moving the stimuli on firing field positions. *J. Gen. Physiol.* **116**, 191–209 (2000).
26. Moser, E. I., Krobot, K. A., Moser, M. B. & Morris, R. G. Impaired spatial learning after saturation of long-term potentiation. *Science* **281**, 2038–42 (1998).
27. Moser, M. B. & Moser, E. I. Functional differentiation in the hippocampus. *Hippocampus* **8**, 608–19 (1998).
28. Lever, C., Wills, T., Cacucci, F., Burgess, N. & O’Keefe, J. Long-term plasticity in hippocampal place-cell representation of environmental geometry. *Nature* **416**, 90–4 (2002).
29. Whitlock, J. R., Heynen, A. J., Shuler, M. G. & Bear, M. F. Learning induces long-term potentiation in the hippocampus. *Science* **313**, 1093–7 (2006).
30. Fanselow, M. S. & Dong, H.-W. Are the Dorsal and Ventral Hippocampus Functionally Distinct Structures? *Neuron* **65**, 7–19 (2010).
31. O’Keefe, J. & Burgess, N. Geometric determinants of the place fields of hippocampal neurons. *Nature* **381**, 425–8 (1996).
32. Hartley, T., Burgess, N., Lever, C., Cacucci, F. & O’Keefe, J. Modeling place fields in terms of the cortical inputs to the hippocampus. *Hippocampus* **10**, 369–79 (2000).
33. Samsonovich, A. & McNaughton, B. L. Path integration and cognitive mapping in a continuous attractor neural network model. *J. Neurosci.* **17**, 5900–20 (1997).
34. McNaughton, B. *et al.* Deciphering the hippocampal polyglot: the hippocampus as a path integration system. *J. Exp. Biol.* **199**, 173–185 (1996).
35. Brun, V. H. *et al.* Place cells and place recognition maintained by direct entorhinal-hippocampal circuitry. *Science* **296**, 2243–6 (2002).
36. Fyhn, M., Molden, S., Witter, M. P., Moser, E. I. & Moser, M.-B. Spatial representation in the entorhinal cortex. *Science* **305**, 1258–64 (2004).

37. Hargreaves, E. L., Rao, G., Lee, I. & Knierim, J. J. Major dissociation between medial and lateral entorhinal input to dorsal hippocampus. *Science* **308**, 1792–4 (2005).
38. Hafting, T., Fyhn, M., Molden, S., Moser, M.-B. & Moser, E. I. Microstructure of a spatial map in the entorhinal cortex. *Nature* **436**, 801–6 (2005).
39. Fuhs, M. C. & Touretzky, D. S. A spin glass model of path integration in rat medial entorhinal cortex. *J. Neurosci.* **26**, 4266–76 (2006).
40. Solstad, T., Moser, E. I. & Einevoll, G. T. From grid cells to place cells: a mathematical model. *Hippocampus* **16**, 1026–31 (2006).
41. O’Keefe, J. & Burgess, N. Dual phase and rate coding in hippocampal place cells: theoretical significance and relationship to entorhinal grid cells. *Hippocampus* **15**, 853–66 (2005).
42. Burak, Y. & Fiete, I. R. Accurate path integration in continuous attractor network models of grid cells. *PLoS Comput. Biol.* **5**, e1000291 (2009).
43. Burgess, N., Barry, C. & O’Keefe, J. An oscillatory interference model of grid cell firing. *Hippocampus* **17**, 801–12 (2007).
44. Van Cauter, T., Poucet, B. & Save, E. Unstable CA1 place cell representation in rats with entorhinal cortex lesions. *Eur. J. Neurosci.* **27**, 1933–46 (2008).
45. Zhang, S.-J. *et al.* Optogenetic dissection of entorhinal-hippocampal functional connectivity. *Science* **340**, 1232627 (2013).
46. Witter, M. P. The perforant path: projections from the entorhinal cortex to the dentate gyrus. *Prog. Brain Res.* **163**, 43–61 (2007).
47. Brun, V. H. *et al.* Progressive increase in grid scale from dorsal to ventral medial entorhinal cortex. *Hippocampus* **18**, 1200–12 (2008).
48. Barry, C., Hayman, R., Burgess, N. & Jeffery, K. J. Experience-dependent rescaling of entorhinal grids. *Nat. Neurosci.* **10**, 682–4 (2007).

49. Fyhn, M., Hafting, T., Treves, A., Moser, M.-B. & Moser, E. I. Hippocampal remapping and grid realignment in entorhinal cortex. *Nature* **446**, 190–4 (2007).
50. Solstad, T., Boccara, C. N., Kropff, E., Moser, M.-B. & Moser, E. I. Representation of geometric borders in the entorhinal cortex. *Science* **322**, 1865–8 (2008).
51. Sargolini, F. *et al.* Conjunctive representation of position, direction, and velocity in entorhinal cortex. *Science* **312**, 758–62 (2006).
52. Boccara, C. N. *et al.* Grid cells in pre- and parasubiculum. *Nat. Neurosci.* **13**, 987–94 (2010).
53. Giocomo, L. M., Zilli, E. a, Fransén, E. & Hasselmo, M. E. Temporal frequency of subthreshold oscillations scales with entorhinal grid cell field spacing. *Science* **315**, 1719–22 (2007).
54. Garden, D. L. F., Dodson, P. D., O'Donnell, C., White, M. D. & Nolan, M. F. Tuning of synaptic integration in the medial entorhinal cortex to the organization of grid cell firing fields. *Neuron* **60**, 875–89 (2008).
55. Skaggs, W. E., Knierim, J. J., Kudrimoti, H. S. & McNaughton, B. L. A model of the neural basis of the rat's sense of direction. *Adv. Neural Inf. Process. Syst.* **7**, 173–80 (1995).
56. Taube, J. S. The head direction signal: origins and sensory-motor integration. *Annu. Rev. Neurosci.* **30**, 181–207 (2007).
57. Welinder, P. E., Burak, Y. & Fiete, I. R. Grid cells: the position code, neural network models of activity, and the problem of learning. *Hippocampus* **18**, 1283–300 (2008).
58. Couey, J. J. *et al.* Recurrent inhibitory circuitry as a mechanism for grid formation. *Nat. Neurosci.* **16**, 318–24 (2013).
59. Lever, C., Burton, S., Jeewajee, A., O'Keefe, J. & Burgess, N. Boundary vector cells in the subiculum of the hippocampal formation. *J. Neurosci.* **29**, 9771–7 (2009).

60. Krupic, J., Burgess, N. & O'Keefe, J. Neural representations of location composed of spatially periodic bands. *Science* **337**, 853–7 (2012).
61. Hafting, T., Fyhn, M., Bonnevie, T., Moser, M.-B. & Moser, E. I. Hippocampus-independent phase precession in entorhinal grid cells. *Nature* **453**, 1248–52 (2008).
62. Jeewajee, A., Barry, C., O'Keefe, J. & Burgess, N. Grid cells and theta as oscillatory interference: electrophysiological data from freely moving rats. *Hippocampus* **18**, 1175–85 (2008).
63. Zilli, E. a. Models of grid cell spatial firing published 2005-2011. *Front. Neural Circuits* **6**, 16 (2012).
64. Giocomo, L. M. & Hasselmo, M. E. Time constants of h current in layer ii stellate cells differ along the dorsal to ventral axis of medial entorhinal cortex. *J. Neurosci.* **28**, 9414–25 (2008).
65. Giocomo, L. M. & Hasselmo, M. E. Knock-out of HCN1 subunit flattens dorsal-ventral frequency gradient of medial entorhinal neurons in adult mice. *J. Neurosci.* **29**, 7625–30 (2009).
66. Giocomo, L. M. *et al.* Grid Cells Use HCN1 Channels for Spatial Scaling. *Cell* **147**, 1159–1170 (2011).
67. Ikeda, J., Mori, K., Oka, S. & Watanabe, Y. A columnar arrangement of dendritic processes of entorhinal cortex neurons revealed by a monoclonal antibody. *Brain Res.* **505**, 176–9 (1989).
68. Solodkin, A. & Van Hoesen, G. W. Entorhinal cortex modules of the human brain. *J. Comp. Neurol.* **365**, 610–7 (1996).
69. Burgalossi, A. *et al.* Microcircuits of functionally identified neurons in the rat medial entorhinal cortex. *Neuron* **70**, 773–86 (2011).
70. Barry, C. *et al.* The boundary vector cell model of place cell firing and spatial memory. *Rev. Neurosci.* **17**, 71–97 (2006).



71. Savelli, F., Yoganarasimha, D. & Knierim, J. J. Influence of boundary removal on the spatial representations of the medial entorhinal cortex. *Hippocampus* **18**, 1270–82 (2008).
72. MacDonald, C. J., Lepage, K. Q., Eden, U. T. & Eichenbaum, H. Hippocampal “time cells” bridge the gap in memory for discontinuous events. *Neuron* **71**, 737–49 (2011).
73. Morris, R. G., Garrud, P., Rawlins, J. N. & O’Keefe, J. Place navigation impaired in rats with hippocampal lesions. *Nature* **297**, 681–3 (1982).
74. Wilson, M. A. & McNaughton, B. L. Dynamics of the hippocampal ensemble code for space. **261**, 1055–1058 (1993).
75. Leutgeb, S. *et al.* Independent codes for spatial and episodic memory in hippocampal neuronal ensembles. *Science* **309**, 619–23 (2005).
76. Muller, R. U. & Kubie, J. L. The effects of changes in the environment on the spatial firing of hippocampal complex-spike cells. *J. Neurosci.* **7**, 1951–68 (1987).
77. Stensola, H. *et al.* The entorhinal grid map is discretized. *Nature* **492**, 72–78 (2012).
78. Jezek, K., Henriksen, E. J., Treves, A., Moser, E. I. & Moser, M.-B. Theta-paced flickering between place-cell maps in the hippocampus. *Nature* **478**, 246–9 (2011).
79. Rolls, E. T., Stringer, S. M. & Elliot, T. Entorhinal cortex grid cells can map to hippocampal place cells by competitive learning. *Network* **17**, 447–65 (2006).
80. Cheng, S. & Frank, L. M. The structure of networks that produce the transformation from grid cells to place cells. *Neuroscience* **197**, 293–306 (2011).
81. Monaco, J. D. & Abbott, L. F. Modular realignment of entorhinal grid cell activity as a basis for hippocampal remapping. *J. Neurosci.* **31**, 9414–25 (2011).

82. De Almeida, L., Idiart, M. & Lisman, J. E. The input-output transformation of the hippocampal granule cells: from grid cells to place fields. *J. Neurosci.* **29**, 7504–12 (2009).
83. Sreenivasan, S. & Fiete, I. R. Grid cells generate an analog error-correcting code for singularly precise neural computation. *Nat. Neurosci.* **14**, 1330–1337 (2011).
84. Yoon, K. *et al.* Specific evidence of low-dimensional continuous attractor dynamics in grid cells. *Nat. Neurosci.* **16**, 1077–84 (2013).
85. Bonnevie, T. *et al.* Grid cells require excitatory drive from the hippocampus. *Nat. Neurosci.* **16**, 309–17 (2013).
86. Burak, Y. Do We Understand the Emergent Dynamics of Grid Cell Activity? *J. Neurosci.* **26**, 9352–9354 (2006).
87. Wills, T. J., Lever, C., Cacucci, F., Burgess, N. & O’Keefe, J. Attractor dynamics in the hippocampal representation of the local environment. *Science* **308**, 873–6 (2005).
88. Leutgeb, J. K., Leutgeb, S., Moser, M.-B. & Moser, E. I. Pattern separation in the dentate gyrus and CA3 of the hippocampus. *Science* **315**, 961–6 (2007).
89. RASMUSSEN, T. & PENFIELD, W. The human sensorimotor cortex as studied by electrical stimulation. *Fed. Proc.* **6**, 184 (1947).
90. Dombeck, D. A., Harvey, C. D., Tian, L., Looger, L. L. & Tank, D. W. Functional imaging of hippocampal place cells at cellular resolution during virtual navigation. *Nat. Neurosci.* **13**, 1433–40 (2010).
91. Harvey, C. D., Collman, F., Dombeck, D. A. & Tank, D. W. Intracellular dynamics of hippocampal place cells during virtual navigation. *Nature* **461**, 941–6 (2009).
92. Kjelstrup, K. B. *et al.* Finite scale of spatial representation in the hippocampus. *Science* **321**, 140–3 (2008).
93. Jung, M. W. & Wiener, I. Comparison of Spatial Firing Characteristics Ventral Hippocampus of the Rat. **74**, (1994).

94. Nadel, L. Dorsal and ventral hippocampal lesions and behavior. *Physiol. Behav.* **3**, 891–900 (1968).
95. Henke, P. G. Hippocampal pathway to the amygdala and stress ulcer development. *Brain Res. Bull.* **25**, 691–5 (1990).
96. Swanson, L. W. & Cowan, W. M. An autoradiographic study of the organization of the efferent connections of the hippocampal formation in the rat. *J. Comp. Neurol.* **172**, 49–84 (1977).
97. Poppenk, J., Evensmoen, H. R., Moscovitch, M. & Nadel, L. Long-axis specialization of the human hippocampus. *Trends Cogn. Sci.* **17**, 230–40 (2013).
98. Evensmoen, H. R. *et al.* The Anterior Hippocampus Supports a Coarse, Global Environmental Representation and the Posterior Hippocampus Supports Fine-grained, Local Environmental Representations. *J. Cogn. Neurosci.* **25**, 1908–25 (2013).
99. Brown, T. H., Kairiss, E. W. & Keenan, C. L. Hebbian synapses: biophysical mechanisms and algorithms. *Annu. Rev. Neurosci.* **13**, 475–511 (1990).
100. Langston, R. F. *et al.* Development of the spatial representation system in the rat. *Science* **328**, 1576–80 (2010).
101. Wills, T. J., Cacucci, F., Burgess, N. & O’Keefe, J. Development of the hippocampal cognitive map in preweanling rats. *Science* **328**, 1573–6 (2010).
102. Giocomo, L. M., Moser, M.-B. & Moser, E. I. Computational Models of Grid Cells. *Neuron* **71**, 589–603 (2011).
103. Cheng, K. A purely geometric module in the rat’s spatial representation. *Cognition* **23**, 149–78 (1986).
104. Cheng, K. Whither geometry? Troubles of the geometric module. *Trends Cogn. Sci.* **12**, 355–61 (2008).
105. Biegler, R. & Morris, R. G. Landmark stability is a prerequisite for spatial but not discrimination learning. *Nature* **361**, 631–3 (1993).

106. Etienne, A. S. & Jeffery, K. J. Path integration in mammals. *Hippocampus* **14**, 180–92 (2004).
107. Knierim, J. J., Kudrimoti, H. S. & McNaughton, B. L. Interactions between idiothetic cues and external landmarks in the control of place cells and head direction cells. *J. Neurophysiol.* **80**, 425–46 (1998).
108. Save, E., Nerad, L. & Poucet, B. Contribution of multiple sensory information to place field stability in hippocampal place cells. *Hippocampus* **10**, 64–76 (2000).
109. Etienne, A. S., Maurer, R., Boulens, V., Levy, A. & Rowe, T. Resetting the path integrator: a basic condition for route-based navigation. *J. Exp. Biol.* **207**, 1491–508 (2004).
110. Mach, E. Ueber das Sehen von Lagen und Winkeln durch die Bewegung des Auges. *Sitzungsberichte der Math. Cl. der Kais. Akad. der Wissenschaften* **42**, 215–224 (1860).
111. Furmanski, C. S. & Engel, S. a. An oblique effect in human primary visual cortex. *Nat. Neurosci.* **3**, 535–6 (2000).
112. Wang, G., Ding, S. & Yunokuchi, K. Difference in the representation of cardinal and oblique contours in cat visual cortex. *Neurosci. Lett.* **338**, 77–81 (2003).
113. Xu, X., Collins, C. E., Khaytin, I., Kaas, J. H. & Casagrande, V. a. Unequal representation of cardinal vs. oblique orientations in the middle temporal visual area. *Proc. Natl. Acad. Sci. U. S. A.* **103**, 17490–5 (2006).
114. Nasr, S. & Tootell, R. B. H. A cardinal orientation bias in scene-selective visual cortex. *J. Neurosci.* **32**, 14921–6 (2012).
115. Liang, Z., Shen, W. & Shou, T. Enhancement of oblique effect in the cat's primary visual cortex via orientation preference shifting induced by excitatory feedback from higher-order cortical area 21a. *Neuroscience* **145**, 377–83 (2007).
116. Shen, W., Liang, Z. & Shou, T. Weakened feedback abolishes neural oblique effect evoked by pseudo-natural visual stimuli in area 17 of the cat. *Neurosci. Lett.* **437**, 65–70 (2008).

117. Müller, T. *et al.* An analysis of orientation and ocular dominance patterns in the visual cortex of cats and ferrets. *Neural Comput.* **12**, 2573–95 (2000).
118. Killian, N. J., Jutras, M. J. & Buffalo, E. A. A map of visual space in the primate entorhinal cortex. *Nature* **491**, 761–4 (2012).



## **6 Contributions (papers 1-3)**

---





Paper I

Is not included due to copyright



Paper II



\*Manuscript

## **Topography of head direction cells in medial entorhinal cortex**

Lisa M Giacomo<sup>1†</sup>, Tor Stensola<sup>1‡</sup>, Tora Bonnevie<sup>1‡</sup>, Tiffany van Cauter<sup>1</sup>, May-Britt Moser and Edvard I Moser<sup>1†</sup>

1. Kavli Institute for Systems Neuroscience and Centre for Neural Computation, Norwegian Brain Center, Norwegian University of Science and Technology, Olav Kyrres gate 9, 7491 Trondheim, Norway

\* Current address: Department of Neurobiology, 299 Campus Drive, Stanford University School of Medicine, Stanford, CA 94305

† Corresponding authors.

‡Equal contribution

Running Head: Topographical organization of head direction cells

Author Contributions: LMG, TS, TB, MBM and EIM planned experiments and analyses, LMG, TB and TVC collected data, TS performed the discontinuity analyses, LMG analyzed the remaining data, and LMG and EIM wrote the paper, with inputs from the other authors.

Abstract: 159 words; Main text: 3821 words, Figure legends: 1547 words; References: 1522 words; 6 figures; 6 Supplementary Figures and Supplemental Experimental Procedures and References

## **Abstract**

Neural circuits in the medial entorhinal cortex (MEC) support translation of the external environment to an internal map of space, with grid and head direction neurons providing metrics for distance and orientation. We show here that head direction cells in MEC layer III are organized topographically. Head direction tuning varies widely at all positions on the dorso-ventral axis but in layer III there is a gradual dorsal-to-ventral increase in the average width of the directional firing field. Highly tuned cells were encountered only at the dorsal end of MEC. Similar topography was not observed among head direction cells in layers V-VI. At all locations, in all MEC layers, the preferred firing direction (directional phase) showed a uniform distribution. The continuity of the dorso-ventral tuning gradient co-existed with discrete topography in the spatial scale of simultaneously recorded grid cells. The findings point to dorso-ventral gradients as a fundamental property of entorhinal circuits, upon which modular organization may be expressed in selected subpopulations.

## **Highlights**

- Head direction cells exhibit topographic organization in medial entorhinal cortex
- Entorhinal directional tuning decreases from dorsal to ventral
- The dorsoventral tuning gradient is expressed only in layer III
- The directional tuning gradient is gradual and unlike the topography of grid cells

## **Introduction**

In sensory systems, topographic maps mirror the spatial order of the sensory receptor surfaces. Different topographies characterize different functional systems, with phenotypes spanning from the discrete or modular organization of barrels in the somatosensory cortex [1] and ocular dominance columns in the visual cortex [2, 3] to the orderly but continuous organization of orientation pinwheels superimposed on ocular dominance columns [4, 5]. For all of these topographies, the spatial organization of the sensory maps is thought to arise during development by the formation of precise connections between sensory receptors and central target cells [6-9].

Topographically organized maps have been found also in higher-end non-sensory cortices. One example is the map of spatially-responsive grid cells in the MEC [10-13]. The periodic firing fields of these cells are arranged topographically by scale, with grid wavelength increasing in discrete steps across anatomically overlapping modules along the dorso-ventral MEC axis [13, 14]. A dorso-ventral scale expansion has also been observed in hippocampal place cells [15, 16]. The presence of topographical organization in MEC and hippocampus raises the possibility that, in non-sensory cortices, topography is generated not by inputs from sensory areas but by processes intrinsic to the circuit. An intrinsic mechanism for grid maps would be consistent with reports of gradients in membrane potential dynamics and synaptic integrative properties along the same dorso-ventral MEC axis that shows the expansion in grid scale [17-20]. These gradients span across multiple entorhinal layers and several morphologically-defined cell types [18, 21, 22].

If the gradient in entorhinal grid scale reflects a global change in the composite intrinsic or synaptic properties of the MEC circuit, then similar gradients might also occur in the properties of other functionally defined entorhinal cell types, such as the head direction cells of the intermediate and deep MEC layers [12]. Head direction cells are cells that increase their firing from a low rate to a high rate whenever the animal is facing a particular direction, irrespective of position or behavior at the time [23-25]. Different head direction cells have different directional preferences (phases). By retaining their directional phase relationships across environments, head direction cells form a cohesive map of the animal's orientation [24, 26, 27]. Cells with such directional properties have been found in a variety of brain regions [25, 28-31]. In MEC and adjacent pre- and parasubiculum, head-direction tuning sometimes occurs in conjunction with grid fields [12, 32], pointing to head direction cells as a cell type that might potentially express topography along the same dorso-ventral axis as the grid cells. The aim of the present study was to determine if entorhinal head direction cells express dorso-ventral topography, and if so, whether this topography is continuous or, as in grid cells, modular.

## **Results**

### *Topography of directional tuning*



To examine if entorhinal head direction neurons have properties that mirror the dorso-ventral scale expansion in grid cells, we implanted rats with microdrives running parallel to layer III or V-VI of MEC. Neural activity was then recorded at multiple dorso-ventral MEC locations while the rat explored an open arena (n = 22 rats; 11 were part of previous studies [12, 13, 33]). Recordings started at the dorsal border of MEC and extended up to 4.2 mm further in the ventral direction (recording range per animal:  $1431 \pm 1034 \mu\text{m}$ , mean  $\pm$  standard deviation (S.D.); Fig. 1AC and 2AC; Fig. S1). We identified a total of 1742 well separated cells in MEC layers III and V-VI (597 of which were part of previous studies [12, 13, 33]), in addition to 245 cells in MEC layer II and 206 cells in pre- and parasubiculum. Directional firing was estimated for each neuron in two ways, by correlating peak firing direction across time blocks (directional stability) and by calculating, for the entire trial, the length of the mean vector of firing rate as a function of direction (directional tuning). Neurons with directional stability significantly higher than the 99<sup>th</sup> percentile threshold of a shuffled distribution (directional correlation > 0.20) were classified as head direction cells (layer III: n = 424; layers V-VI: n = 587; 58 % of all layer III/V-VI MEC neurons; Fig. S2). Directional tuning was expressed for each of these cells by the length of their mean firing rate vector (mean vector length, MVL). Using directional tuning (MVL) to define the 99<sup>th</sup> percentile threshold gave similar results (Fig. S2).

Directional tuning in layer III head direction cells correlated significantly with the neuron's position along the dorso-ventral MEC axis ( $r = 0.24$ ,  $P < 0.001$ ; Fig. 1BC). The dorso-ventral gradient was expressed as a gradual decrease in MVL across successive bins of recording positions ( $F(3,418) = 6.88$ ,  $P < 0.001$ ). In particular, the decrease reflected a loss of sharply-tuned cells from dorsal to ventral positions (Fig. 1CD). The MVL of the most sharply-tuned cells (top 25%) dropped steeply ( $F(3,102) = 16.38$ ,  $P < 0.001$ ), in contrast to the most broadly-tuned cells (bottom 25%), which also decreased ( $F(3,102) = 13.0$ ,  $P < 0.001$ ) but at a slower rate (Quartile  $\times$  Dorso-ventral position:  $F(3, 204) = 21.7$ ,  $P < 0.001$ ). The decrease in MVL was accompanied by a drop in the percentage of neurons defined as head direction cells (0 – 500  $\mu\text{m} = 53\%$ ; 501-1000  $\mu\text{m} = 48\%$ ; 1001-1500  $\mu\text{m} = 36\%$  and 1501 – 2000  $\mu\text{m} = 27\%$ ). The dorso-ventral gradient was not caused by larger cell numbers in dorsal MEC than at more ventral MEC positions. Matching the cell numbers by downsampling each bin of recording positions to the number of cells in the smallest bin did not abolish the dorso-ventral MVL gradient. For 100 downsampling iterations, 84/100 P values were significant at  $P < 0.05$ . The gradient was accompanied by a reduction from dorsal to ventral in directional information ( $r = -0.14$ ,  $P < 0.01$ ;  $F(3,418) = 3.75$ ,  $P = 0.01$ ). The changes were independent of firing rate and directional stability; neither firing rate nor directional stability changed significantly across dorso-ventral bins in layer III ( $F(3,418) = 0.30$ ,  $P = 0.83$  and  $F(3, 418) = 0.58$ ,  $P = 0.63$ , respectively). The firing rate of many head direction cells correlated significantly with running speed ( $P < 0.05$  for 133/424 cells; bins of 1 ms).

The dorso-ventral tuning gradient was layer and region-specific. No gradient was detected among head direction cells in MEC layers V-VI. In these layers, the cells remained sharply tuned at all dorso-ventral levels ( $r = 0.03$ ,  $P = 0.50$ ;  $F(6,578) = 0.89$ ,  $P = 0.50$ ; Fig. 2). There was a significant difference between layers III and V-VI in the slope of the regression line for dorso-ventral position versus directional tuning (Fig. 1C vs. 2C; independent-samples t test:  $t(14) =$

3.0,  $P < 0.05$ , data from all rats with at least 20 cells sampled over at least 500  $\mu\text{m}$ ). Directional tuning was also unaltered along the dorso-ventral axis of the adjacent presubiculum (Fig. S3;  $r = 0.14$ ,  $P = 0.35$ , 46 cells sampled over 2500  $\mu\text{m}$  of the presubicular long axis in 1 animal). Sharply-tuned cells were abundant at ventral levels in this brain area, suggesting that, within the parahippocampal system, the gradient in directional tuning may be unique to MEC layer III.

The population of entorhinal head direction cells is functionally diverse. For example, a large number of entorhinal head direction cells have conjunctive grid properties, i.e. the cells fire in a grid pattern but discharge only when the animal runs in a certain range of directions. We asked if the dorso-ventral MEC gradient was expressed specifically in conjunctive or non-conjunctive cells. Conjunctive cells were defined as head direction cells with a grid score higher than the 99th percentile threshold determined from a shuffled distribution (Fig. S4). Using this criterion, we found a higher proportion of conjunctive cells in layer III than layers V-VI (31% and 11% of the head direction cells, respectively,  $Z = 7.95$ ,  $P < 0.001$ ), in agreement with previous reports [12, 32], but there was no difference in the slope of the dorso-ventral tuning gradient between head direction cells that had conjunctive grid fields and head direction cells that were only modulated by direction (Cell group  $\times$  Dorso-ventral position:  $F(3,414) = 0.87$ ,  $P = 0.45$ ), suggesting that the tuning gradient is independent of mechanisms for grid scale.

We next examined how modulation by head direction is organized along the orthogonal medio-lateral axis of the MEC. Unfolded MEC maps were generated from sagittal brain sections by first measuring, for each animal, the total dorso-ventral length of MEC layer II in the section with the deepest tetrode track and then projecting the dorso-ventral recording location of each of the animal's cells onto this layer II measurement (Fig. S5A). Measurements for different animals (one section per rat) were arranged according to medio-lateral position, covering a total medio-lateral length of 840  $\mu\text{m}$  in layer III and 960  $\mu\text{m}$  in layers V-VI. The aggregated 2D map showed a dorso-ventral directional tuning gradient at all medio-lateral levels of layer III, with a consistent dorso-ventral separation of cells with directional tuning in the upper and lower quartiles of the group data (all medio-lateral levels; Fig. S5B). There was no significant correlation between directional tuning (MVL) and the medio-lateral position of the layer III cells ( $r = -0.06$ ,  $P = 0.23$ , 424 cells, all animals). There was no corresponding separation of upper and lower quartiles in layers V-VI (Fig. S5C). Taken together, these data suggest (i) that in layer III, but not in V-VI, sharply-tuned head direction cells are skewed towards the dorsal border of the MEC, and (ii) that this layer III gradient is expressed across a wide medio-lateral range.

Finally, to address whether the band-like directional tuning gradient in layer III is a general feature of rodent MEC topography, we investigated the distribution of head direction cells in a second species. We examined a population of 720 superficial MEC neurons from 14 mice, 7 of which were part of a previous study [34] (Fig. 3). Layers II and III were combined into a single data set in this analysis, as the head direction cell population in mice appears to cross into layer II [34, 35]. Using the same stability criterion and the same shuffling procedure as for the rat data, we identified 296 head direction neurons. Just as in rats, we found a significant decrease from dorsal to ventral MEC in the average tuning width (MVL) of layer III head direction cells ( $r = 0.27$ ,  $P < 0.001$ ;  $F(3,292) = 7.9$ ,  $P < 0.001$ , ANOVA with 4 bins of 300  $\mu\text{m}$  each). This reflected,

like in rats, a gradual loss of sharply-tuned cells and a corresponding increase in broadly-tuned cells (Quartile  $\times$  Dorso-ventral position:  $F(3, 142) = 6.92$ ,  $P < 0.001$ ; Fig. 3BC). The directional tuning gradient was expressed at all medio-lateral levels of the MEC ( $\sim 450 \mu\text{m}$ ) (Fig. S5D).

#### *Directional phase has a non-topographic distribution*

Studies of head direction cells in other brain regions have not observed any topography in the distribution of preferred firing direction, or directional phase. We asked if such topography might yet be present in layer III of MEC, considering that directional tuning is graded in this layer. For each  $500 \mu\text{m}$  bin along the dorso-ventral MEC axis of each animal, we determined the distribution of peak firing directions among all head direction neurons recorded in the area. The directional uniformity of each distribution was estimated by calculating the length of the mean vector of the distribution of peak firing directions. Layer III and V-VI cells were examined separately. Peak firing directions were widely distributed at all dorso-ventral levels in both cell layers (Fig. 4). The average MVL for firing direction was  $0.31 \pm 0.04$  (mean  $\pm$  S.E.M.). MVL did not correlate significantly with bin number along the dorso-ventral axis ( $F(3,20) = 1.35$ ,  $P = 0.29$ ). Thus, the data speak against large-scale topographical organization of directional firing phase, despite the presence of a directional tuning gradient.

The presence of topography in the distribution of directional phase was investigated also in the mouse sample. As in rats, peak firing directions were widely distributed in all dorso-ventral segments (mean MVL:  $0.31 \pm 0.04$ ; correlation with dorso-ventral recording position:  $r = 0.25$ ,  $P = 0.42$ ). The data indicate that head direction cells are organized similarly in rats and mice.

#### *The dorso-ventral directional tuning gradient is non-modular*

If the topographical changes in head direction and grid properties shared a common cellular mechanism, such as a dorso-ventral gradient in an ion-channel conductance [17, 20, 36], they might also share a number of functional properties. In a final set of analyses, we asked if head direction cells express a modular organization similar to that of grid cells, which are organized in clusters with discrete scale and orientation properties [13].

Clustering was observed in grid cells but not head direction cells (Fig. 5A). To quantify modularity, we sorted the grid cells of each animal into successive bins of values for grid spacing and the head direction cells into successive bins for directional tuning (MVL). Cells in each bin were counted (Fig. 5B). Distributions were generated for a range of bin widths. The discontinuity of each distribution (the presence of sharp frequency transitions) was then estimated by calculating the S.D. of all nearest-neighbor bin-differences. S.D.s for different bin widths were finally averaged to yield a single 'discontinuity' measure for each animal (Fig. 5C). Considering that discrete electrode movements would by necessity impose a certain degree of discontinuity on any topographically organized variable, we also calculated, for each grid-spacing and MVL distribution, the discontinuity of the corresponding sample of recording positions (Fig. 5BC). The discontinuity of the direction and spacing distributions were then log normalized by the discontinuity of the corresponding distribution for recording positions (Fig. 5C-

E). Discontinuity of recording positions was not different for grid and head direction cells ( $F(22) = 1.4$ ,  $P > 0.20$ ). Because large cell samples were needed for these intra-animal analyses, the analysis was performed only on the rat data (16 rats, 392 grid cells, 939 head direction cells). For discontinuity analyses of directional tuning, conjunctive and non-conjunctive head direction cells (with and without grid properties) were pooled. The number of conjunctive cells was too low for separate analyses of this subpopulation.

In 12 out of 16 animals, the discontinuity of the directional tuning distribution was lower than for the distribution of recording locations (mean  $\pm$  S.E.M. of log normalized discontinuity:  $-0.23 \pm 0.09$ ; Fig. 5E; see Fig. S6 for data from individual animals). Low discontinuity ratios (log ratios below 0) were measured in both layer III and layer V-VI head direction cells, irrespective of how the data were binned (Fig. 5D). The smooth nature of the MVL distribution was in sharp contrast to the distribution of values for grid spacing in grid cells from the same animals. The discontinuity for grid spacing was always larger than for recording depth (8 out of 8 animals; mean  $\pm$  S.E.M. of log normalized discontinuity:  $0.64 \pm 0.11$ ). Discontinuity was lower for head direction cells than grid cells in all 8 animals with both head direction and grid cell populations as well as across all data sets (Fig. 5E;  $F(22) = 15.3$ ,  $P < 0.001$ , ANOVA with Tukey-Kramer post-hoc test). In head direction cells, log-normalized discontinuity was not significantly different from 0 (layer III:  $t(9) = 1.35$ ,  $P = 0.21$ ; layer V:  $t(6) = 2.21$ ,  $P = 0.07$ ), whereas grid cells had positive values ( $t(7) = 6.05$ ,  $P < 0.001$ ). The effects were present in both left and right MEC (left hemisphere:  $F(14) = 4.2$ ,  $P < 0.05$ ; right hemisphere:  $F(11) = 13.6$ ,  $P < 0.001$ ). Taken together, these observations suggest that entorhinal head direction cells do not share the modular feature organization of grid cells. Instead, directional tuning appears to vary on a continuous scale, with sharply tuned cells dropping off gradually along the dorso-ventral axis of the MEC.

Finally, we validated the discontinuity measure by testing how sensitive it is to the modularity of a model distribution. Probability density functions were generated as mixtures of varying numbers of Gaussian modes with variable spread within a feature space  $[0,1]$ . From these functions, we drew random samples ( $n = 120$  per simulation) and determined their discontinuity following the same procedure as for real data in Fig. 5. Because dorso-ventral recording positions tended to be clustered, with more than one cell recorded in most locations, a similar simulation was performed for recording positions (Fig 6CD). The discontinuity values from the simulated feature distributions were then log normalized to the discontinuity values from the simulated position distributions (Fig. 6EF), and the normalized values were summarized across combinations of mode number and spread in a matrix (Fig. 6G). Each combination was simulated 100 times, and the average value was recorded. From this matrix we calculated the zero-contour that separates combinations of mode number and spread that could be detected as modular from those that could not (log-normalized discontinuity above and below 0, respectively; black contour line in Fig. 6G). Within the simulated feature space, at the lower end of simulated mode numbers, clusters were detectable at Gaussian spreads (S.D.)  $< \sim 0.05$  (feature space/20). As expected, there was a negative relationship between number of modes and their Gaussian spread such that distributions drawn from densities with increased numbers of modes were detectably clustered only when the Gaussian spreads were narrow (Fig. 6G).

To determine which mode-spread combinations were associated with the log-normalized discontinuity values obtained in the head direction and grid spacing data, we calculated contours in the simulation matrix corresponding to these values (dashed colored lines in Fig. 6GH). While mode-spread combinations for grid spacing were constrained to  $< 9$  modes and narrow Gaussian spreads (S.D.  $\sim 0.01$ ), head direction modulation, both in layer III and layers V-VI, were associated with a markedly wider range of mode numbers and broader Gaussian spreads, well outside the detection bound for discontinuous distributions (zero-contour, Fig. 6H). In real data, recorded across extensive portions of the dorso-ventral axis of MEC, no more than 4-5 grid modules have been detected and the total number, for the entire MEC, has been predicted to be within the upper single-digit range [13]. This corresponds well with the grid cluster range predicted by our simulations, suggesting that the discontinuity analysis captures such structure if it is present in the data. According to these analyses, the mode-spread combinations predicted for head direction modulation were far from the modular detection bound, strongly implying that head direction modulation distributes with a smooth topography in both layer III and V.

## **Discussion**

This study provides evidence for topographical organization in the tuning of a population of head direction cells. Previous work has identified head direction cells in a number of brain regions, from the dorsal tegmental nucleus to the parahippocampal cortices [25], but within each region the directional properties of the cell population have not demonstrated any clear-cut anatomical organization. Using a cell sample that is both larger and more widespread than in previous work, we find that (i) head direction-modulated cells exist at all levels of the dorso-ventral axis of MEC, and (ii) in layer III, these cells are arranged topographically such that, over a wide medio-lateral range, the most sharply-tuned cells are located near the dorsal border of MEC. As distance from the dorsal border increases, less directionally tuned cells become more prevalent. A similar gradient was not observed in deeper MEC layers. The orientation of the head direction fields did not exhibit detectable topography, suggesting that directional phase and directional tuning are mechanistically uncoupled.

The directional tuning gradient in MEC layer III provides an example of topography that may be generated within the entorhinal network itself. One possible substrate for the dorsal bias in directional tuning is the patch of cytochrome oxidase-active neurons at the border between MEC and parasubiculum, in which activity is significantly modulated by head direction [37]. However, this dorsal patch of MEC neurons is anatomically discrete and only a few hundred microns wide, whereas the present head direction gradient was continuous and extended over at least 2 millimeters, suggesting that additional or alternative substrates are required to generate the directional tuning gradient along the dorso-ventral MEC axis.

Both head direction cells and grid cells have been proposed to emerge from continuous attractor networks, with one-dimensional continuous ring attractors giving rise to head direction cells [38-40] and two-dimensional continuous attractor sheets underlying the formation of grid

cells [41-46]. All continuous attractor models proposed so far rely on translation-invariant recurrent weight matrices that impose similar tuning widths on all neurons of the network [47]. Variations in the width or shape of the tuning curve are thought to arise from different network modules. The discretization of grid scale and grid orientation in MEC is consistent with this type of translation-invariant continuous-attractor organization [13]. In contrast, the continuity of the directional tuning distribution in layer III would not be expected if head direction cells emerged directly from attractor networks in this layer.

Several factors might contribute to the lack of modularity in the directional tuning distribution of MEC layer III. First, it is possible that the directional signal originates in attractor networks upstream, with continuous tuning curves emerging secondarily in MEC layer III as a result of differential and graded convergence along the dorso-ventral axis of this layer. The existence of sharply-tuned head direction cells in MEC layer V as well as multiple low-level brain areas [48] would be consistent with an external origin of the graded head direction signal. Alternatively, the continuity of the directional tuning gradient may reflect a graded dorso-ventral organization in single-cell properties of layer III cells, resulting from differential expression of ion channel genes between dorsal and ventral MEC, possibly expressed on top of inputs from an afferent attractor network. Several studies have reported dorso-ventral gradients in the kinetics and density of ion channels in MEC, such as variations in properties of Ih [17, 18, 20] and leak potassium currents [20]. Some of these, or other, ion channels may be graded in layer III in a manner that matches the dorsal-ventral topography of head direction cells. However, the number of layer-specific genes with differential expression along the entorhinal dorso-ventral axis is probably large [22]. Whether and how any of these gradients translate to a gradual and regionally selective increase in directional tuning remains to be determined.

The functional implications of the directional tuning gradient remain to be established but the fact that the loss of directional tuning along the dorso-ventral axis coincides with an increase in the scale of co-localized grid cells raises the possibility that these properties are causally related. If grid cells are formed by an attractor mechanism and translation on the neuronal lattice reflects a changing speed and direction input [41-45], the speed of the translation might be reduced in parallel with a decrease in the directional specificity of the velocity vector. Grid scale should consequently be increased. Until this date, however, attractor models have not considered the impact of variations in directional tuning. Directional tuning has also not been considered in intracellular models of grid formation, although it is conceivable that, in these models, reductions in the length of the mean direction vector may dampen the frequency of intrinsic theta oscillations, which in turn should increase the spacing of grid fields [49-51]. Finally, it remains possible that wider directional tuning and larger grid scales reflect changes in the magnitude of a common velocity input to head direction cells and grid cells.

The observation of a dorso-ventral gradient in directional tuning but not directional phase is reminiscent of the scale-phase architecture of the entorhinal grid map and the hippocampal place map. In grid cells as well as place cells, firing locations (phase) show no detectable relationship to brain anatomy whereas field size and field spacing (scale) increase from dorsal to ventral [11, 15, 16]. The broader directional and spatial tuning profiles of ventral cells leads

to increased response overlap within the local cell population. This increase in representational density may improve the fault-tolerance of the network, although probably at the cost of increased ambiguity. The widening of tuning widths at ventral levels may also allow larger parts of the environment to be interconnected, consistent with a primary role for dorsal MEC and hippocampus regions in fine-grained local representations and for ventral regions in coarser and more global representations [16, 52].

### **Experimental Procedures**

Single unit activity was recorded from tetrodes in MEC of 22 male Long-Evans rats and 14 male mice (a hybrid 50:50% background of C57BL/6J:129SVEV). In rats, the tetrode bundle was implanted 0.2 mm in front of or flush with the transverse sinus, 4.2-4.6 mm from the midline and 1.8-2.0 mm below the dura, angled 18-24 degrees in the anterior direction in the sagittal plane. In mice, the bundle was implanted 0.3-0.5 mm in front of the transverse sinus, 3.1-3.25 mm from the midline and 0.8-1.2 mm below the dura, angled 4-8 degrees in the posterior direction in the sagittal plane. The rats were trained to forage a  $1.5 \times 1.5 \times 0.5 \text{ m}^3$  black square box with a white cue card. For the mice, the box size was  $1.0 \times 1.0 \times 0.5 \text{ m}^3$ .

The position of the animal was determined from tracking of the LEDs. Firing fields were characterized by sorting the position data into  $2.5 \times 2.5 \text{ cm}$  bins and smoothing the data with a 21-sample boxcar window filter (400 ms, ten samples of each side). Maps for number of spikes and time were smoothed individually using a quasi-Gaussian kernel over the surrounding  $5 \times 5$  bin. Firing rates were determined by dividing the spike number and time for each bin of the two smoothed maps. The animal's head direction was calculated for each tracked sample from the projection of the relative position of the two LEDs onto the horizontal plane. The directional tuning function for each cell was obtained by plotting the firing rate as a function of the animal's directional heading, divided into bins of 3 degrees and smoothed with a 14.5-degree mean window filter (14 bins on each side). Grid cells and head direction cells were identified by comparing values for spatial periodicity and head direction tuning with corresponding values obtained from distributions of shuffled data (Fig. S2 and Supplementary Experimental Procedures). Discontinuities in grid spacing and head direction tuning were estimated by comparing distributions of these values with the smoothness of the distribution of recording locations along the dorso-ventral MEC axis (Fig. 5 and 6; Supplementary Experimental Procedures).

### **Acknowledgements:**

We thank R. Skjerpeng and V. Frolov for programming, A.M. Amundsgård, I. Hammer, K. Haugen and H. Waade for technical assistance, T. Solstad, Y. Roudi and M.P. Witter for discussion, M.P. Witter for advice on tetrode positions, and H. Eggink, K. Frøland, P. Mertens, T. Solstad and H. Stensola for contributing data to the project. This work was supported by a Personal Postdoctoral Fellowship to LMG, a Centre of Excellence grant and a NEVRONOR grant from the Research Council of Norway, and by funding from the Kavli Foundation.

### **Figure Legends**

**Figure 1:** Directional tuning of layer III head direction cells decreases along the dorso-ventral axis of MEC.

(A) Nissl-stained sagittal section for a rat with tetrodes in layer III of MEC. Red arrows mark the first (most dorsal) and last (most ventral) location where a head direction cell was recorded.

(B) Examples of layer III head direction cells from an individual rat (rat 15733). Polar plots indicating firing rate as a function of head direction are shown for the six head direction cells with the highest MVL in each of four 500  $\mu\text{m}$  bins along the dorso-ventral MEC axis; sharpest tuning on the top and weakest tuning on the bottom. MVL values are indicated above each polar plot. Each column represents data from a single bin.

(C) Directional tuning (MVL) of layer III head direction cells as a function of position along the dorso-ventral axis of MEC. Data are from 17 rats. Left: Scatterplot with purple circles corresponding to individual cells. Black circles correspond to individual cells shown in A (6 sharpest cells of an individual animal). Regression line is indicated. Right: Mean  $\pm$  S.E.M. for bins of 500  $\mu\text{m}$  along the dorso-ventral MEC axis. The sharpest 25% of head direction cells (light purple circles) decreased significantly in tuning breadth whereas weakly tuned cells (bottom 25%, blue circles) were present at all dorso-ventral levels. Panel A shows examples from the upper quartile.

(D) Proportion of sharply-tuned cells (top 25%; light purple) decreases while the proportion of broadly-tuned cells (bottom 25%; light blue) increases with distance along the dorso-ventral MEC axis.

**Figure 2:** Head direction tuning at different levels of the dorso-ventral axis of MEC layers V-VI.

(A) Nissl-stained sagittal section for a rat with tetrodes in layers V-VI of MEC. Arrows as in Fig. 1A.

(B) Examples of head direction cells from layers V-VI of rat 15895. The six head direction cells with the highest mean vector lengths in each 500  $\mu\text{m}$  anatomical bin are shown; sharpest tuning on the left and weakest tuning on the right. Mean vector length is indicated above each cell.

(C) Directional tuning (MVL) of layer V head direction cells as a function of position along the dorso-ventral MEC axis (data from 9 rats). Left: Scatterplot with green circles corresponding to individual cells. Black circles correspond to individual cells shown in A (sharpest cells of an individual animal). Right: Mean  $\pm$  S.E.M. for bins of 500  $\mu\text{m}$  along the dorso-ventral MEC axis (top and bottom quartiles).

(D) Proportion of sharply-tuned and broadly-tuned head direction cells (top and bottom 25%, respectively) at successive dorso-ventral MEC levels.



**Figure 3:** The dorso-ventral gradient in layer III directional tuning translates across rodent species.

(A) Nissl-stained sagittal section for a mouse with tetrodes in layers II and III of MEC. Arrows as in Fig. 1A.

(B) Examples of layer II-III head direction cells from an individual mouse. Polar plots indicating firing rate as a function of head direction are shown as in Fig. 1. The six head direction cells with the highest directional tuning (MVL) in each 300  $\mu\text{m}$  bin are shown.

(C) Directional tuning (MVL) of layer II-III head direction cells as a function of position along the dorso-ventral MEC axis in mice. Left: Scatterplot showing decrease in directional tuning as a function of dorso-ventral recording location (13 mice; one mouse did not have head direction cells). Black circles correspond to individual cells shown in B (one animal). Right: Mean  $\pm$  S.E.M. for bins of 300  $\mu\text{m}$  along the dorso-ventral MEC axis (top and bottom quartiles).

(D) Changes in proportion of sharply and broadly-tuned head direction cells along the dorso-ventral MEC axis, as in Fig. 1D.

**Figure 4:** Non-topographic organization of firing direction in MEC head direction cells.

(A) Circular frequency histograms showing distribution of peak firing directions across layer III cells in 500  $\mu\text{m}$  anatomical bins spanning the dorsal (top) to ventral (bottom) MEC axis of individual rats. Each column represents a different animal and each row a 500  $\mu\text{m}$  bin. The mean vector of the distribution of firing directions is indicated for each sample by a red arrow. Frequency bins are 20 deg. Frequency scale is given by red numbers.

(B) Directional preference or phase (top) and tuning width (bottom) of all head direction-modulated layer III cells in a single rat. There was no detectable change in directional firing preference along the dorso-ventral axis of this animal, whereas the relationship to tuning was highly significant ( $r = 0.60$ ,  $P < 0.001$ ). For other animals, the total cell numbers across layer III bins ( $< 3$  anatomical bins of 500  $\mu\text{m}$ ) were too small for statistical analysis.

(C-D) Distribution of directional preferences (phase) for each dorso-ventral bin in each rat; (C), layer III; (D), layers V-VI. Each circle refers to one cell sample (one anatomical bin in one animal). Uniformity in firing direction is expressed by the length of the mean vector (MVL). Note predominance of low MVLs at all dorso-ventral levels.

**Figure 5:** Modular organization of grid cells but not head direction cells.

(A) Scatterplots showing grid spacing in grid cells (top) and directional tuning (MVL) in head direction cells as a function of rank-ordered dorso-ventral recording position in individual

animals. Layer III and layer V-VI head direction cells are shown separately (middle and bottom, respectively). Each dot corresponds to one cell. Cells are plotted sequentially along the x-axis to avoid overlap between cells at similar recording depths. Kernel smoothed density estimates (vertical black area) are presented to the right for each data set. Kernel width: [data range]/35. Note modular distribution of grid spacing in contrast to directional tuning.

(B) Frequency distributions showing data from scatterplots in A (black bars). Frequency distributions were generated for grid spacing or directional tuning (black bars) as well as dorso-ventral recording locations (gray bars). The latter were plotted to allow correction for discontinuities in cell sampling along the dorso-ventral axis that might cause overestimation of discontinuity in the firing data. Discontinuity was then estimated for each of the three distributions as the standard deviation of all nearest-neighbor frequency bin count differences averaged over bin widths. Discontinuity values were calculated for a range of bin widths. Shown here are plots with an intermediate bin width ([data range]/10).

(C) Discontinuity for grid spacing or directional tuning MVL (black bars) and dorso-ventral recording locations (gray bars) calculated for the data in B. Grid spacing showed a more discontinuous distribution than expected from discontinuities in the distribution of recording locations [13]. Directional tuning, in contrast, was not more discontinuous than the anatomical distribution.

(D) Log normalized discontinuity for grid spacing (red) and head direction tuning (cyan) across a range of bin widths in the 8 animals where both grid-cell and head direction-cell populations were recorded. For each animal and bin width, discontinuity of grid spacing or directional tuning MVL was log normalized to the discontinuity of the corresponding distribution of dorso-ventral recording positions. Colored areas show S.E.M. Grid cells had larger discontinuity values than head direction cells at all bin widths. Head direction cells had negative values in both layer III and layer V-VI. The more negative values of the layer V-VI data reflect the weak topographical organization of these cells (in layers V-VI, MVL distributes widely at all dorso-ventral levels such that even large steps in dorso-ventral recording location produce a smooth distribution).

(E) Log normalized discontinuity averaged across bin widths in all 16 animals (means  $\pm$  S.E.M.).

**Figure 6:** Validation of discontinuity measure.

(A) Simulation showing effect of number and width of modes on the discontinuity of a frequency distribution. Histograms (black bars) of simulated feature distributions ( $n = 120$  samples each) were drawn randomly from multimodal probability density functions (PDFs; red curves). The PDFs featured 3 Gaussian modes (mode locations indicated by red dots above each plot) with varying spread (indicated in red text left of each figure). Increased spread caused less clustering in the drawn distributions, which in turn was reflected as a decrease in discontinuity (values shown above each plot). Frequency and density were normalized to maximum values per plot.

(B) Same as A but for distributions with 8 modes.

(C) Frequency plot showing distribution of simulated recording positions. In real data, multiple cells tend to be recorded at the same position, resulting in increased clustering. Such clustering was incorporated in the simulated position distribution by drawing  $n = 120$  samples from  $P_v n$  random uniform positions in dorso-ventral (DV) recording space (defined in the present example within  $[0,1]$ ), where  $P_v$  is the average ratio of number of recording positions to number of recorded cells per data set. The effect on discontinuity (measured as in Fig. 5) is shown above the plot.

(D) Same as C, but for the 8 mode distributions in B.

(E) Discontinuity from the simulated distributions in A log-normalized to the discontinuity of the simulated recording position distribution in C. Bars show log-normalized discontinuity with different Gaussian spread (indicated under each bar). Negative values indicate less clustering in A than for the simulated recording distribution in C.

(F) Same as E, but for the 8-mode distributions and simulated recording positions in BD. The high number of modes caused lower log-normalized discontinuity values.

(G) Summary matrix showing log-normalized discontinuity across a range of distribution widths and numbers of modes. Log-normalized discontinuity is color-coded. For each condition, the value represents the mean from 100 simulation trials. The black solid line is the zero-contour and denotes the separation between combinations of mode number and widths that are identifiable as modular (positive, lighter colors in heat map) and those that are not (negative, darker colors in heat map). Plotted in dashed colored lines are the contours corresponding to the mean log-normalized discontinuity observed for head-direction modulation (green: layers V-VI, purple: layer III) and grid cell spacing (red; see Fig. 5).

(H) Contour map from G, including S.E.M. of the data. Color-coding as in G.

## **References**

1. Woolsey, T.A., and van der Loos, H. (1970). The structural organization of layer IV in the somatosensory region (SI) of mouse cerebral cortex. The description of a cortical field composed of discrete cytoarchitectonic units. *Brain Res* 17, 205-242.
2. Hubel, D.H., and Wiesel, T.N. (1962). Receptive fields, binocular interaction and functional architecture in the cat's visual cortex. *J Physiol* 160, 106-154.
3. Hubel, D.H., and Wiesel, T.N. (1969). Anatomical demonstration of columns in the monkey striate cortex. *Nature* 221, 747-750.
4. Blasdel, G.G., and Salama, G. (1986). Voltage-sensitive dyes reveal a modular organization in monkey striate cortex. *Nature* 321, 579-585.
5. Bonhoeffer, T., and Grinvald, A. (1991). Iso-orientation domains in cat visual cortex are arranged in pinwheel-like patterns. *Nature* 353, 429-431.
6. Sperry, R.W. (1943). Visuomotor coordination in the new (*Triturus viridescens*) after regeneration of the optic nerve. *J Comp Neurol* 79, 33-55.
7. Sperry, R.W. (1963). Chemoaffinity in the orderly growth of nerve fiber patterns and connections. *Proc Natl Acad Sci U S A* 50, 703-710.
8. Cheng, H.J., Nakamoto, M., Bergemann, A.D., and Flanagan, J.G. (1995). Complementary gradients in expression and binding of ELF-1 and Mek4 in development of the topographic retinotectal projection map. *Cell* 82, 371-381.
9. Drescher, U., Kremoser, C., Handwerker, C., Loschinger, J., Noda, M., and Bonhoeffer, F. (1995). In vitro guidance of retinal ganglion cell axons by RAGS, a 25 kDa tectal protein related to ligands for Eph receptor tyrosine kinases. *Cell* 82, 359-370.
10. Fyhn, M., Molden, S., Witter, M.P., Moser, E.I., and Moser, M.B. (2004). Spatial representation in the entorhinal cortex. *Science* 305, 1258-1264.
11. Hafting, T., Fyhn, M., Molden, S., Moser, M.B., and Moser, E.I. (2005). Microstructure of a spatial map in the entorhinal cortex. *Nature* 436, 801-806.
12. Sargolini, F., Fyhn, M., Hafting, T., McNaughton, B.L., Witter, M.P., Moser, M.B., and Moser, E.I. (2006). Conjunctive representation of position, direction, and velocity in entorhinal cortex. *Science* 312, 758-762.
13. Stensola, H., Stensola, T., Solstad, T., Frøland, K., Moser, M.B., and Moser, E.I. (2012). The entorhinal map is discretized. *Nature* 492, 72-78.
14. Barry, C., Hayman, R., Burgess, N., and Jeffery, K.J. (2007). Experience-dependent rescaling of entorhinal grids. *Nat Neurosci* 10, 682-684.
15. Jung, M.W., Wiener, S.I., and McNaughton, B.L. (1994). Comparison of spatial firing characteristics of units in dorsal and ventral hippocampus of the rat. *J Neurosci* 14, 7347-7356.
16. Kjelstrup, K.B., Solstad, T., Brun, V.H., Hafting, T., Leutgeb, S., Witter, M.P., Moser, E.I., and Moser, M.B. (2008). Finite scale of spatial representation in the hippocampus. *Science* 321, 140-143.
17. Giocomo, L.M., and Hasselmo, M.E. (2008). Time constants of h current in layer II stellate cells differ along the dorsal to ventral axis of medial entorhinal cortex. *J Neurosci* 28, 9414-9425.
18. Giocomo, L.M., Zilli, E.A., Fransen, E., and Hasselmo, M.E. (2007). Temporal frequency of subthreshold oscillations scales with entorhinal grid cell field spacing. *Science* 315, 1719-1722.
19. Boehlen, A., Heinemann, U., and Erchova, I. (2010). The range of intrinsic frequencies represented by medial entorhinal cortex stellate cells extends with age. *J Neurosci* 30, 4585-4589.

20. Garden, D.L., Dodson, P.D., O'Donnell, C., White, M.D., and Nolan, M.F. (2008). Tuning of synaptic integration in the medial entorhinal cortex to the organization of grid cell firing fields. *Neuron* *60*, 875-889.
21. Giocomo, L.M., and Hasselmo, M.E. (2008). Computation by oscillations: implications of experimental data for theoretical models of grid cells. *Hippocampus* *18*, 1186-1199.
22. Ramsden, H.L., Simpson, T.I., and Nolan, M.F. (2012). Gene expression patterns reflect anatomical and physiological variation in adult mouse medial entorhinal cortex. *FENS abstract* *6*, 068.024.
23. Ranck, J.B.J. (1985). Head direction cells in the deep cell layer of dorsal postsubiculum in freely moving rats. In *Electrical activity of the archicortex*, G. Buzsaki and C.H. Vanderwolf, eds. (Budapest: Akademiai Kiado), pp. 217-220.
24. Taube, J.S., Muller, R.U., and Ranck, J.B.J. (1990). Head-direction cells recorded from the postsubiculum in freely moving rats. I. Description and quantitative analysis. *J Neurosci* *10*, 420-435.
25. Taube, J.S. (2007). The head direction signal: origins and sensory-motor integration. *Annu Rev Neurosci* *30*, 181-207.
26. Taube, J.S., and Burton, H.L. (1995). Head direction cell activity monitored in a novel environment and during a cue conflict situation. *J Neurophysiol* *74*, 1953-1971.
27. Yoganarasimha, D., Yu, X., and Knierim, J.J. (2006). Head direction cell representations maintain internal coherence during conflicting proximal and distal cue rotations: comparison with hippocampal place cells. *J Neurosci* *26*, 622-631.
28. Chen, L.L., Lin, L.H., Green, E.J., Barnes, C.A., and McNaughton, B.L. (1994). Head-direction cells in the rat posterior cortex. I. Anatomical distribution and behavioral modulation. *Exp Brain Res* *101*, 8-23.
29. Taube, J.S. (1995). Head direction cells recorded in the anterior thalamic nuclei of freely moving rats. *J Neurosci* *15*, 70-86.
30. Stackman, R.W., and Taube, J.S. (1998). Firing properties of rat lateral mammillary single units: head direction, head pitch and angular velocity. *J Neurosci* *18*, 9020-9037.
31. Cho, J., and Sharp, P.E. (2001). Head direction, place, and movement correlates for cells in the rat retrosplenial cortex. *Behav Neurosci* *115*, 3-25.
32. Boccara, C.N., Sargolini, F., Thorensen, V.H., Solstad, T., Witter, M.P., Moser, E.I., and Moser, M.B. (2010). Grid cells in pre- and parasubiculum. *Nat Neurosci* *13*, 987-994.
33. Brun, V.H., Solstad, T., Kjelstrup, K.B., Fyhn, M., Witter, M.P., Moser, E.I., and Moser, M.B. (2008). Progressive increase in grid scale from dorsal to ventral medial entorhinal cortex. *Hippocampus* *18*, 1200-1212.
34. Giocomo, L.M., Hussaini, S.A., Zheng, F., Kandel, E.R., Moser, M.B., and Moser, E.I. (2011). Grid cells use HCN1 channels for spatial scaling. *Cell* *147*, 1159-1170.
35. Fyhn, M., Hafting, T., Witter, M.P., Moser, E.I., and Moser, M.B. (2008). Grid cells in mice. *Hippocampus* *18*, 1230.
36. Giocomo, L.M., and Hasselmo, M.E. (2009). Knock-out of HCN1 subunit flattens dorsal-ventral frequency gradient of medial entorhinal neurons in adult mice. *J Neurosci* *29*, 7625-7630.
37. Burgalossi, A., Herfst, L., von Heimendahl, M., Forste, H., Haskic, K., Schmidt, M., and Brecht, M. (2011). Microcircuits of functionally identified neurons in the rat medial entorhinal cortex. *Neuron* *70*, 773-786.
38. Skaggs, W.E., Knierim, J.J., Kudrimoti, H.S., and McNaughton, B.L. (1995). A model of the neural basis of the rat's sense of direction. *Adv Neural Inf Process Syst* *7*, 173-180.
39. Zhang, K. (1996). Representation of spatial orientation by the intrinsic dynamics of the head-direction cell ensemble: a theory. *J Neurosci* *16*, 2112-2126.

40. Redish, A.D., Elga, A.N., and Touretzky, D.S. (1996). A coupled attractor model of the rodent head direction system. *Network* 7, 671-685.
41. Fuhs, M.C., and Touretzky, D.S. (2006). A spin glass model of path integration in rat medial entorhinal cortex. *J Neurosci* 26, 4266-4276.
42. McNaughton, B.L., Battaglia, F.P., Jensen, O., Moser, E.I., and Moser, M.B. (2006). Path integration and the neural basis of the 'cognitive map'. *Nat Rev Neurosci* 7, 663-678.
43. Burak, Y., and Fiete, I.R. (2009). Accurate path integration in continuous attractor network models of grid cells. *PLoS Comput Biol* 5, e1000291.
44. Couey, J.J., Witoelar, A., Zhang, S.J., Zheng, K., Ye, J., Dunn, B., Czajkowski, R., Moser, M.B., Moser, E.I., Roudi, Y., et al. (2013). Recurrent inhibitory circuitry as a mechanism for grid formation. *Nat Neurosci* 16, 318-324.
45. Bonnevie, T., Dunn, B., Fyhn, M., Hafting, T., Derdikman, D., Kubie, J.L., Roudi, Y., Moser, E.I., and Moser, M.B. (2013). Grid cells require excitatory drive from the hippocampus. *Nat Neurosci* 16, 309-317.
46. Pastoll, H., Solanka, L., van Rossum, M.C., and Nolan, M.F. (2013). Feedback inhibition enables  $\theta$ -nested  $\gamma$  oscillations and grid firing fields. *Neuron* 77, 141-154.
47. Moser, E.I., Moser, M.B., and Roudi, Y. (2013). Network mechanisms of grid cells. *Philos Trans R Soc Lond B Biol Sci* *In Press*.
48. Sharp, P.E., Blair, H.T., and Cho, J. (2001). The anatomical and computational basis of the rat head-direction cell signal. *Trends Neurosci* 24, 289-294.
49. Burgess, N., Barry, C., Jeffery, K.J., and O'Keefe, J. (2005). A grid and place cell model of path integration utilizing phase precession versus theta. In *Computational Cognitive Neuroscience Meeting*, R.C. O'Reilly, ed. (Washington, D.C.).
50. Burgess, N., Barry, C., and O'Keefe, J. (2007). An oscillatory interference model of grid cell firing. *Hippocampus* 17, 801-812.
51. Hasselmo, M.E., Giocomo, L.M., and Zilli, E.A. (2007). Grid cell firing may arise from interference of theta frequency membrane potential oscillations in single neurons. *Hippocampus* 17, 1252-1271.
52. Nadel, L., Hoscheidt, S., and Ryan, L.R. (2013). Spatial cognition and the hippocampus: the anterior-posterior axis. *J Cogn Neurosci* 25, 22-28.

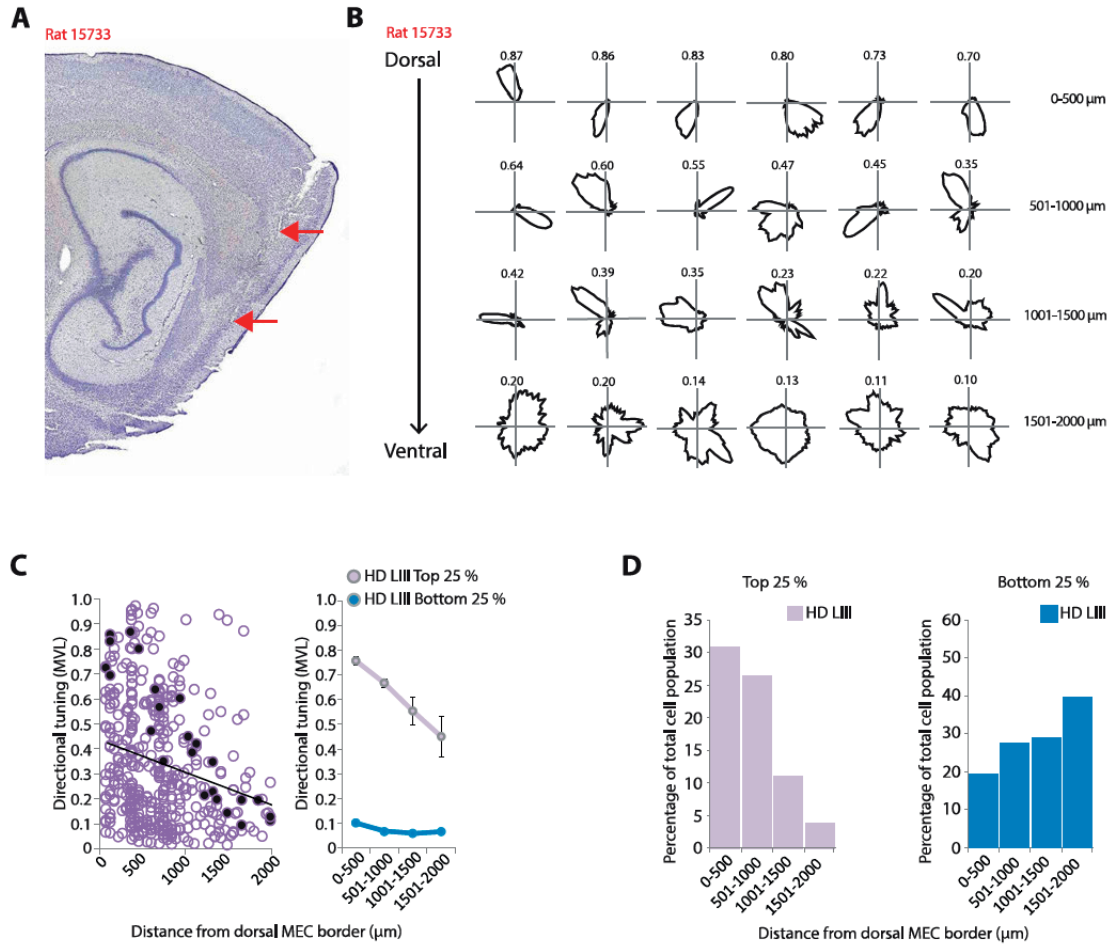


Figure 2

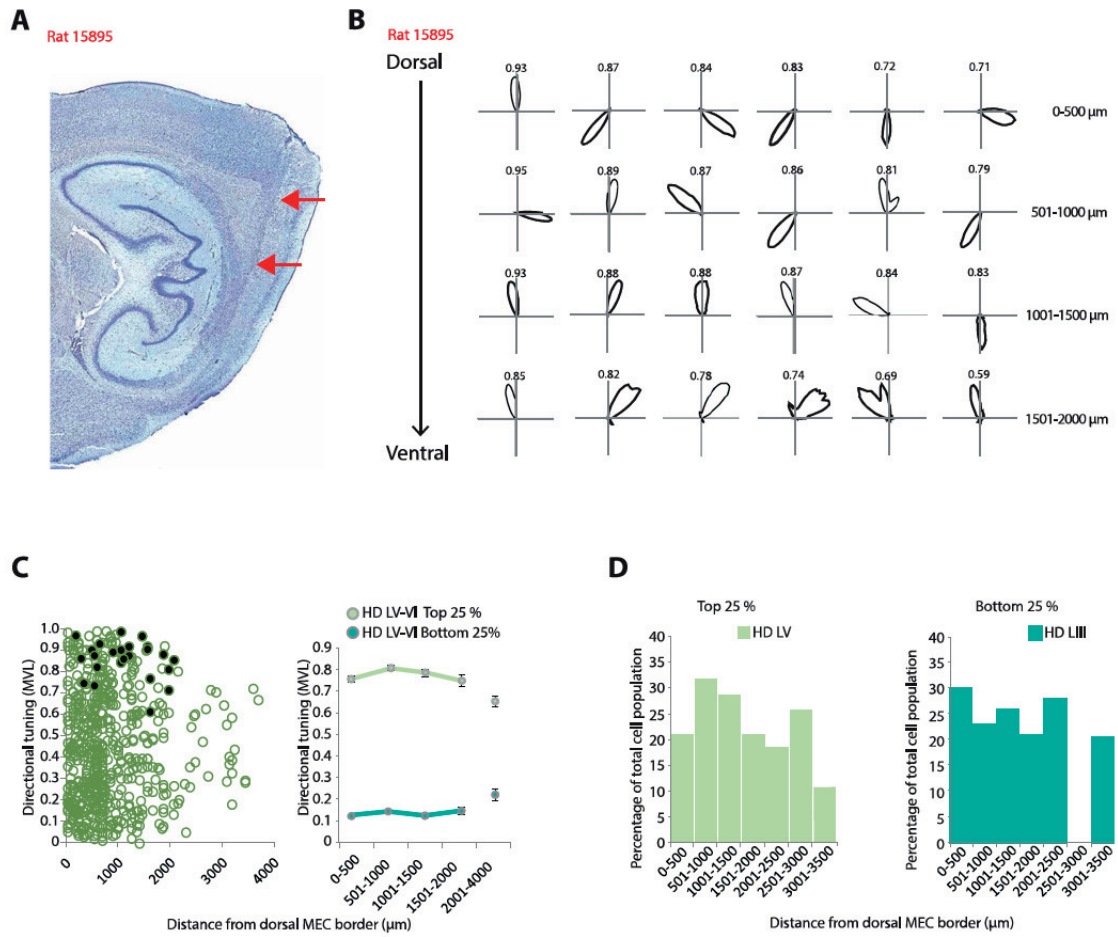




Figure 3

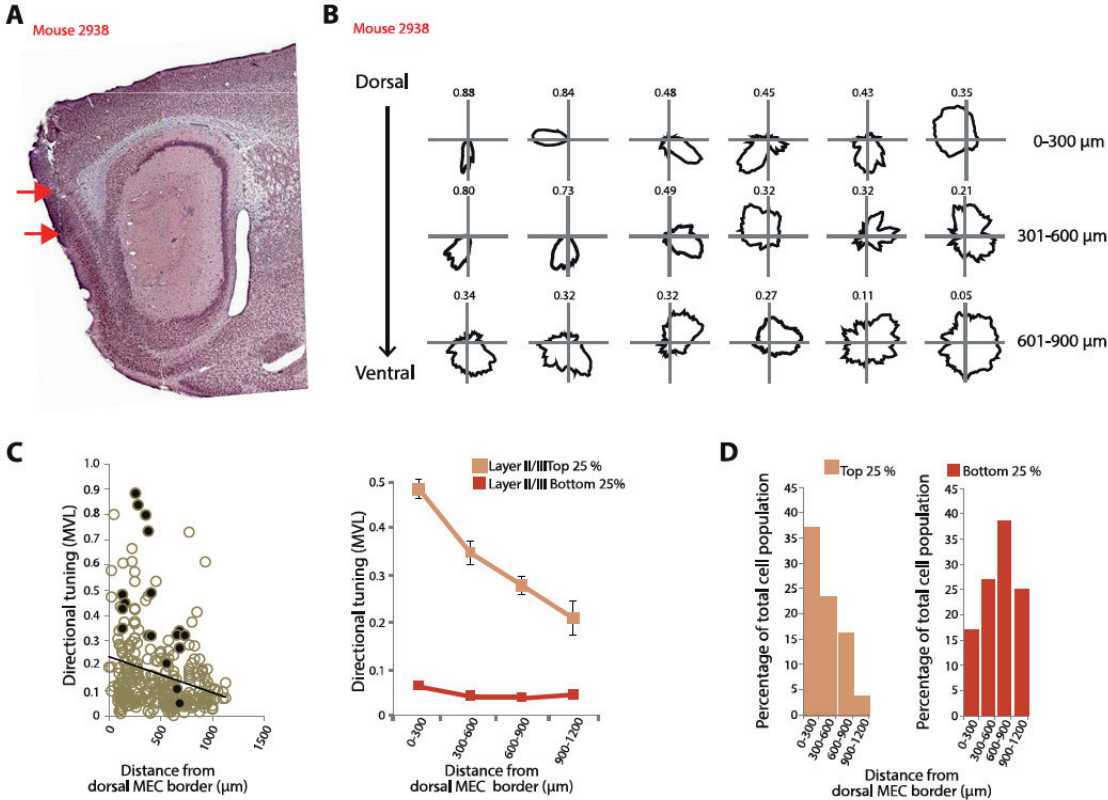


Figure 4

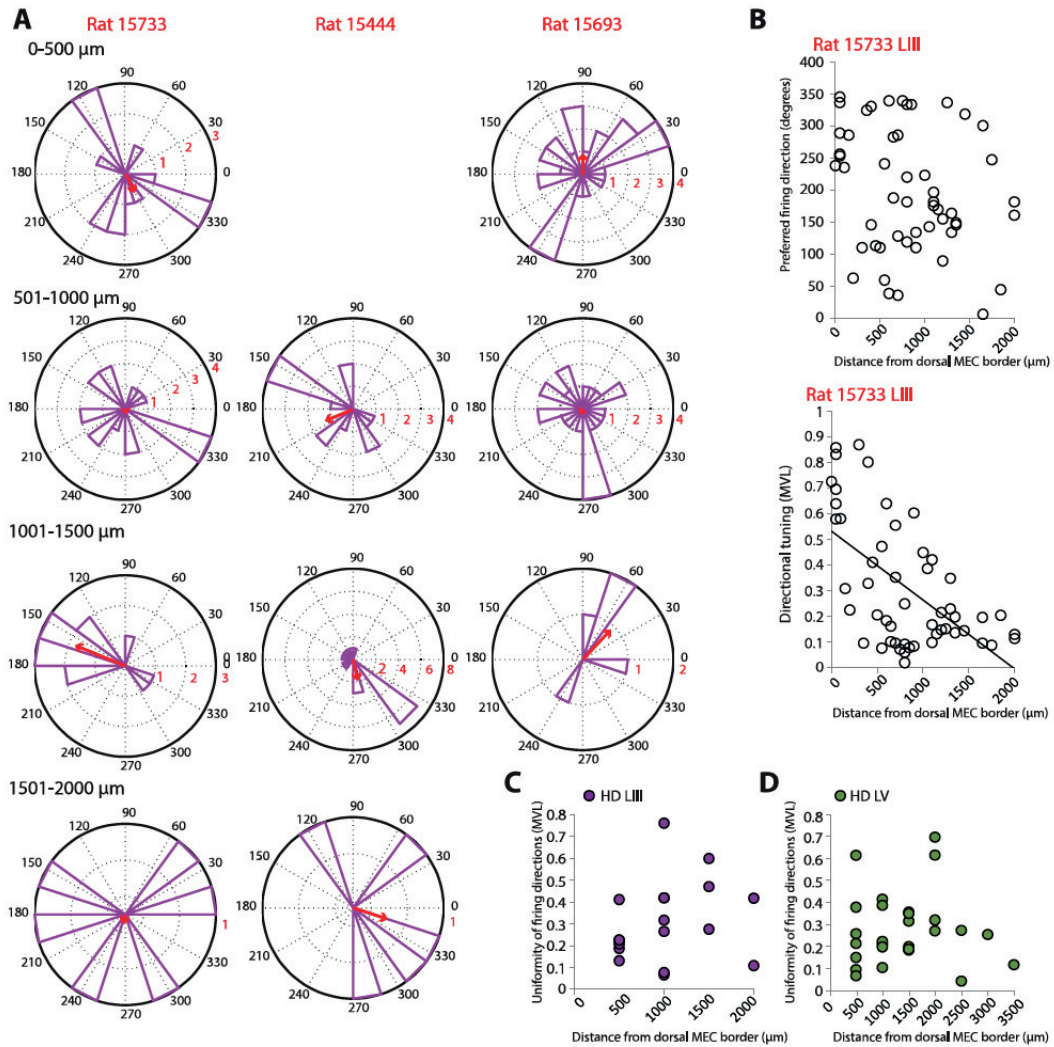


Figure 5

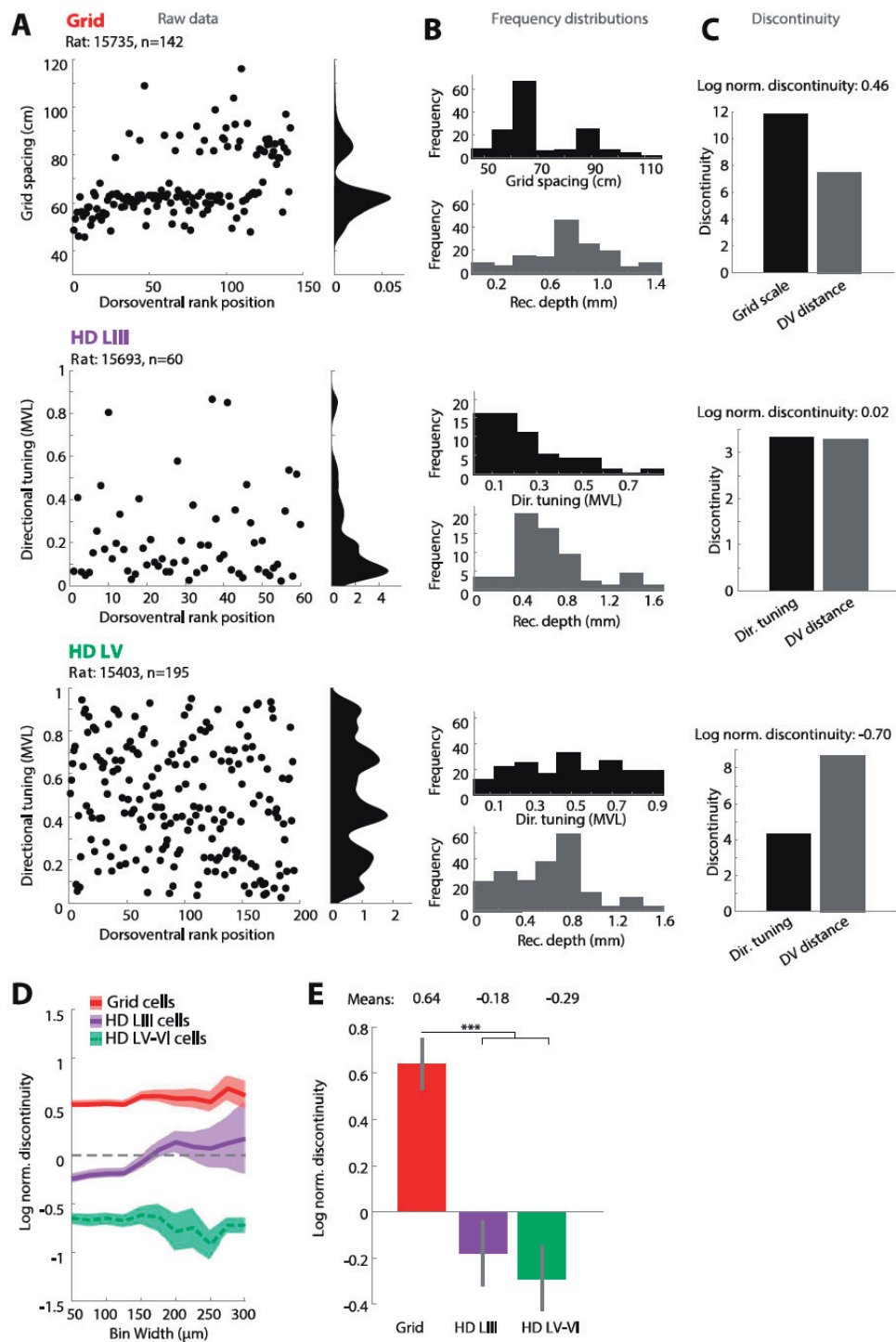
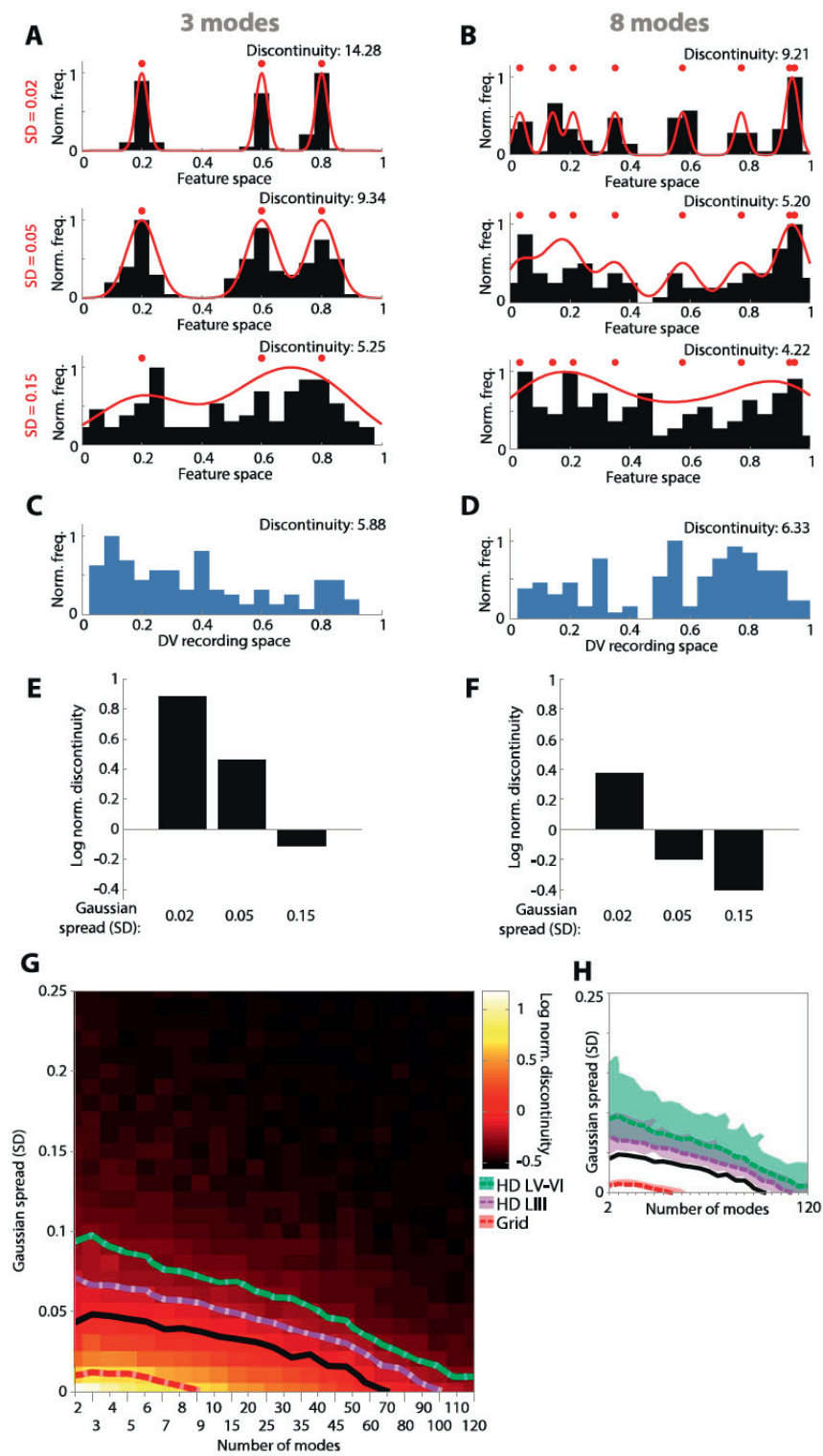


Figure 6



### **Supplementary Experimental Procedures**

#### *Subjects*

Single-unit neural activity was recorded in medial entorhinal cortex (MEC) in 22 freely moving male Long-Evans rats (3-9 months old, 350-550 g at surgery) and 14 freely moving male mice (a hybrid 50:50% background of C57BL/6J:129SVEV, 3-9 months old, 26-38 g at surgery). Eleven of the rats and 7 of the mice were taken from previous studies using similar behavioral paradigms [1-4]. The previous studies did not focus on head direction cells and the majority of the head direction neurons from these animals were not published. Results were similar for new and old data. As in previous studies [2, 5], head direction-tuned firing resided primarily in layers III-VI of the rat MEC.

The animals were housed individually in transparent plexiglass cages (45 × 30 × 35 cm for rats; 30 × 30 × 30 cm for mice) in a temperature and humidity-controlled rat or mouse vivarium near the recording rooms. All animals were maintained on a 12-h light/ 12-h dark schedule. Testing occurred in the dark phase. Both rats and mice were kept at 85-90% of free-feeding body weight and food deprived 18-24 h before each training and recording trial. Water was available *ad libitum*.

#### *Surgery*

Animals were housed together in transparent cages until surgery. With the exception of animals included from previous studies, the animals were first anesthetized with isoflurane (rats: induction chamber level of 5.0% with an air flow at 1400 ml/min; mice: induction chamber level of 3.0% with an air flow at 1200 ml/min). The isoflurane level was gradually reduced once the animals were secured in the stereotaxic apparatus to 1% with an air flow at 1000-1200 ml/min. In addition, an injection of buprenorphine was given immediately after the animal was secured in the stereotaxic apparatus (0.3 mg/ml). Levels of anesthesia were monitored by regularly checking the breathing rate as well as testing reflexes with toe and tail pinch.

All animals were implanted in either one or both hemispheres with a microdrive (16-channel in rats and 8-channel in mice) connected to tetrodes that had been cut flat to the same level. Tetrodes were made of 17 μm polyimide-coated platinum-iridium (90-10%) wire. Electrode impedances were reduced to ~200 kΩ at 1 kHz by platinum plating just before surgical implantation. Small watchmaker's screws and dental cement were used to secure the microdrive to the skull. For rats, the tetrode bundle was implanted 0.2 mm in front of or flush with the transverse sinus, 4.2-4.6 mm from the midline and 1.8-2.0 mm below the dura, angled 18-24 degrees in the anterior direction in the sagittal plane. For mice, the tetrode bundle was implanted 0.3-0.5 mm in front of the transverse sinus, 3.1-3.25 mm from the midline and 0.8-1.2 mm below the dura, angled 4-8 degrees in the posterior direction in the sagittal plane. After surgery, the animals were allowed 3-5 days of recovery before recording in the test environments began.

### *Data Collection*

The animals were exposed to a square box with side walls of 1.5 m in rats and 1.0 m in mice. Before each recording trial, the animal rested on a pedestal or in a large transparent box. The animal was then connected to the recording equipment via AC-coupled unity-gain operational amplifiers and a counterbalance was used so that the animal could move freely throughout the recording box. Over the course of 5-20 days, the tetrodes were lowered in steps of 50  $\mu\text{m}$  or less until the first single neurons could be isolated at appropriate depths. When the spike amplitudes exceeded 2 times the noise level (r.m.s. 20-30  $\mu\text{V}$ ), neural activity was recorded during spontaneous exploratory food-motivated running. Recorded signals were amplified 8000 to 25000 times and bandpass-filtered between 0.8 and 6.7 kHz. Triggered spikes were stored to a disk at 48 kHz (50 samples per waveform, 8 bits/sample) with a 32 bit time stamp (clock rate at 96 kHz). EEG was recorded single-ended from one of the electrodes, amplified 3000-10000 times, lowpass-filtered at 500 Hz, sampled at 4800 Hz and stored with the unit data. The position of the animal was determined from two light-emitting diodes that were tracked by the recording system and an overhead video camera at a sampling rate of 50 Hz. Trials lasted 40 min. After the session, the tetrodes were lowered in steps of 50  $\mu\text{m}$  in rats and 25  $\mu\text{m}$  in mice. At least two hours were allowed to pass before any additional experimental data was collected. For all recording boxes, the walls were made of black acrylic sheets, a polarizing white cue card was displayed in a constant location, and curtains surrounded the box. During recording, small vanilla biscuits or chocolate cereal crumbles were randomly scattered in the enclosure to promote foraging behavior. Between sessions, animals rested in their home cage in the animal housing room. The floor of the test box was cleaned with soap and water between trials.

### *Spike sorting and position estimates*

All spike sorting occurred offline using graphical cluster-cutting software provided by AXONA Ltd (*tint*, originally written by Neil Burgess, UCL). Clustering was performed manually in two-dimensional projections of multidimensional parameter space (consisting of waveform amplitudes) using autocorrelation and cross-correlation functions as additional separation tools. Cluster separation was estimated by calculating distances, in Maholonobis space, between clustered spikes from different cells on the same tetrode (isolation distances) [6]. There was no significant effect of dorso-ventral location on this separation estimate ( $F(3,418) = .89$ ,  $P = 0.45$ ; mean Maholonobis distance:  $54.5 \pm 18.4$ ).

The position of the animal was determined from tracking of the LEDs. Firing fields were characterized by sorting the position data into  $2.5 \times 2.5$  cm bins and smoothing the data with a 21-sample boxcar window filter (400 ms, ten samples of each side). Maps for number of spikes and time were smoothed individually using a quasi-Gaussian kernel over the surrounding  $5 \times 5$  bins [3, 7]. Firing rates were determined by dividing the spike number and time for each bin of the two smoothed maps. The peak rate was defined as the rate in the bin with the highest rate in the firing rate map. Data only included epochs with running speeds between 2.5 and 100 cm/s. Instantaneous running speed was determined by binning data into 1 s segments.

### *Identification of head direction cells*

The animal's head direction was calculated for each tracked sample from the projection of the relative position of the two LEDs onto the horizontal plane. The directional tuning function for each cell was obtained by plotting the firing rate as a function of the animal's directional heading, divided into bins of 3 degrees and smoothed with a 14.5-degree mean window filter (14 bins on each side). The strength of directional tuning was estimated by a directional stability measure. Directional stability was calculated by first quartering each recording session into four equally sized time bins (Supplementary Fig. 2). Next, firing rate by direction was correlated between different time bins (bin 1 vs 2, 1 vs 3, 1 vs 4, etc.), resulting in a total of six comparisons. If the mean correlation for all six comparisons was higher than the 99<sup>th</sup> percentile threshold of a shuffled distribution of directional correlations, the neuron was classified as a head direction cell (Supplementary Fig. 2b). The shuffled distribution was based on all cells from rats that were recorded in either layer III or layer V-VI of MEC (in rats: 920 and 822 cells, respectively) or in adjacent pre- or parasubiculum (in rats: 206 cells). Mouse cells were shuffled separately from rat cells (in mice: 720 cells). No layer V cells were recorded in mice. Four hundred permutations were performed for each cell in each shuffling procedure. For each permutation trial, the entire sequence of spikes fired by the cell was time-shifted along the animal's path by a random interval between 20 s and the total trial length minus 20 s, with the end of the trial wrapped to the beginning. For each permutation, a firing rate map was constructed, the preferred firing direction was calculated, and the stability across the four quarters of the trial was determined. Finally, the 99<sup>th</sup> percentile was read out from the overall distribution of directional stability scores in the shuffled data. For rats, the 99<sup>th</sup> percentile threshold was 0.20; in mice, it was 0.19. Cells with larger values were defined as head direction cells. In addition to using the directional stability measure to define head direction cells, we also shuffled cells to generate a 99<sup>th</sup> percentile threshold for mean vector length (P99 = .19) (Supplemental Fig. 2D). Shuffling was performed in the same manner as shuffling for directional stability but for each permutation, a firing rate map was constructed and the mean vector length calculated. Any cell with a mean vector length higher than the 99<sup>th</sup> percentile was classified as a head direction cell for this analysis. The use of mean vector length to determine the head direction population resulted in an artificial flooring effect and excluded a large number of cells that had a stable but very broad directional tuning. On the other hand, the use of the directional stability measurement avoids this flooring effect and offers the benefit of utilizing one measure to define the population of head direction cells and a second measure (mean vector length) to examine the organization in head direction tuning.

A preliminary analysis with separate shuffling of layer III cells on one hand and layer V-VI and pre- and parasubiculum cells on the other showed an almost negligible difference in 99<sup>th</sup> percentile thresholds (0.20 and 0.21, respectively). Later analysis combined the two cell populations to generate a single 99<sup>th</sup> percentile measure that applied to both layer III and V-VI of the rat MEC, as well as the adjacent presubiculum. To quantify the directional tuning of the head direction cells, we first plotted, for each cell, the distribution of firing rates across all head directions and then calculated, for each cell, the length of the mean vector (the Rayleigh vector, Supplementary Fig. 2). Directional tuning was also estimated by calculating a directional information score:

$$\text{information rate} = \sum_i p_i \lambda_i \log_2 \frac{\lambda_i}{\lambda}$$

where  $\lambda_i$  is the mean firing rate of a unit in the  $i$ -th bin,  $\lambda$  is the overall mean firing rate, and  $p_i$  is the probability that the animal's head pointed in the  $i$ -th directional bin (time spent with the head in the  $i$ -th direction / total recording time).

#### *Identification of grid cells*

To quantify hexagonal periodicity we computed a grid score for each cell by taking a circular sample of the autocorrelation and comparing rotated versions of this sample [2]. The Pearson correlation of this circle, with its rotation in alpha degrees, was obtained for angles of 60 degrees and 120 degrees and for 30, 90 and 150 degrees [2]. The cell's grid score was defined as the minimum difference between any of the elements in the first group and any elements of the second. Grid spacing was defined as the median distance between the center and the nearest six peaks in the autocorrelogram. Because of the sensitivity of the analysis to noise in the grid autocorrelations, grid spacing was analyzed only for cells that met a set of criteria. First, the median distance to the six nearest peaks should match the radius of the circle that gave the highest grid score (the 'outer radius' OR). If the ratio between these two measures was beyond 2 standard deviations of the mean, the cell was excluded from the grid spacing analysis. Second, if the grid spacing detected by the nearest six peaks in the autocorrelation showed a range that was beyond 2 standard deviations of the mean, the cell was excluded from the grid spacing analysis. This criterion removed only a small number from the total cell population (46 out of 596 total grid cells in rats). Grid cells were defined as cells in which rotational symmetry-based grid scores exceeded the 99<sup>th</sup> percentile of a distribution of grid scores for shuffled recordings from the entire population of cells in the same age group and the same brain region. Shuffling was performed in the same way as in previous work [3, 7]. The chance level was determined by a random permutation procedure using all cells recorded. One hundred permutations were performed for each cell in the sample. For each permutation trial, the entire sequence of spikes fired by the cell was time-shifted along the animal's path by a random interval between 20 s and the total trial length minus 20 s, with the end of the trial wrapped to the beginning. The shuffling procedure was repeated 100 times for each of the cells in the sample. For each permutation, a firing rate map and an autocorrelation map were constructed and a grid score was calculated. The 99<sup>th</sup> percentile was read out from the overall distribution of grid scores in the shuffled data for each region. A cell was defined as a grid cell when the grid score exceeded this 99<sup>th</sup> percentile. Cells that passed 99th percentile thresholds for both grid and head direction cells, were defined as conjunctive.

#### *Preferred firing direction (directional phase)*

To examine the distribution of preferred firing directions (directional phases), we analyzed groups of head direction cells in individual rats and mice. Only animals with at least five head direction cells across two anatomical bins (500  $\mu\text{m}$  bins in rats and 300  $\mu\text{m}$  bins in mice) were



used in the analysis. In each animal and for each anatomical bin, we constructed a circular histogram for the preferred firing direction of the cell sample. Similar directional firing preferences were reflected by a high MVL. Layers III and V-VI were analyzed separately. A high value for mean vector length indicates that many head direction cells share the same preferred firing direction while a low value indicates a broader distribution of directional firing preferences. A subset of animals had five or more layer III head direction cells at the same depth but in two different hemispheres. This dataset was used to compare the distribution of preferred firing directions across left and right brain hemispheres (Supplementary Fig. 9).

#### *Discontinuity of distributions for head direction tuning and grid scale*

Methods for calculating the *discontinuity* of a distribution were similar to those developed for a previous study [4]. *Discontinuity* of grid spacing was calculated for each animal with 15 or more grid cells and a grid spacing range of at least 20 cm. Conjunctive and non-conjunctive grid cells were treated similarly. *Discontinuity* of head direction tuning (MVL) was calculated for each animal with 15 or more head direction cells and a MVL range of at least 0.35. Grid cells were first ranked with respect to grid spacing and head direction cells with respect to MVL. In addition, to control for *discontinuity* caused by uneven sampling along the dorso-ventral MEC axis, we ranked both cell types with respect to position of the cells along the dorso-ventral MEC axis. Frequency histograms were then generated for each distribution, using a range of bin sizes. For the recording positions, bin sizes ranged from 50  $\mu\text{m}$  to  $1/7^{\text{th}}$  of the distance between the most dorsal and the most ventral recording location. The number of bins used for each distribution of recording positions was then used to generate corresponding frequency distributions for grid spacing and MVL. For each distribution, the standard deviation of all nearest-neighbor bin count-differences was calculated and its average across bin widths referred to as the '*discontinuity*' of the distribution. The procedure gave low values for smooth distributions (with small nearest-neighbor differences in counts) and large values for step-like or multimodal distributions (with large nearest-neighbor differences in counts, see Fig. 8). Next, the *discontinuity* values for grid spacing and head direction modulation were normalized to (divided by) the *discontinuity* of the corresponding distribution of recording locations. Finally, we determined the log of this ratio, which distributes symmetrically around zero. The log ratio served as the basis for comparing *discontinuity* across cell populations. *Discontinuity* values above zero were taken as indicators of modular organization over and above what was expected from the distribution of recording locations. Large gaps in the sampling distribution may reduce the robustness of the analysis, so to minimize the influence of *discontinuity* in sampling of recording locations, we only considered data sets in which the 90<sup>th</sup> percentile of anatomical inter-cell-distance was less than 225  $\mu\text{m}$ . This resulted in 8 animals with a total of 392 grid cells (mean cell number  $\pm$  S.D.:  $49.0 \pm 38.6$ ). Head direction data sets included 333 layer III cells from 10 rats ( $33.3 \pm 16.0$  cells) and 606 layer V-VI cells from 7 rats ( $86.6 \pm 62.0$  cells). The discreteness of the reference distribution of recording locations was not different across cell groups (Supplementary Fig. 16). *Discontinuity* of MVL was not determined for conjunctive head direction cells because the number of such cells was too low.

### *Discontinuity simulation*

Data simulation was used to determine the effect of number and width of modes on discontinuity in a multimodal distribution. The goal was to systematically explore the relationship between the number of clusters and their width on randomly drawn distributions within some predefined feature space. We generated probability density functions (PDFs) composed of a varying number of Gaussian modes ( $N_m$ ) within a feature space in the interval  $[0,1]$ . Mode-locations in this space were drawn from the uniform distribution  $X \sim U(0,1)$ .  $N_m$  was explored within  $[2, N_c]$ , where  $N_c$  = number of 'cells' (samples randomly drawn from the PDFs in every simulation;  $N_c$  = 120 per simulation). When  $N_m = N_c$ , the resulting drawn distribution is uniform, and per definition not clustered beyond the contribution from chance. As the ratio of modes to cells decreases ( $N_m < N_c$ ), there will be more than 1 cell drawn per mode on average, increasing feature clustering. When  $N_m \ll N_c$ , all cells are drawn from a small number of modes. In this way, we could systematically introduce increased clustering in the drawn distribution. How much clustering results in the drawn distributions depends on separability between contributions from each mode, which is dependent on the Gaussian spread of each PDF mode. For each simulation, the mode spread was equal for all modes. The range of spreads considered were standard deviations (S.D.) from 0 to 0.25 given the feature-space interval  $[0,1]$ . In each simulation, after drawing  $N_c$  samples from the  $N_m$  modes, we calculated the discontinuity of the resulting distribution. The procedure for this was identical to that for experimental data (detailed above). In experimental data, multiple cells tend to be recorded at the same dorso-ventral position, increasing clustering within the distribution of recording positions, which in turn might cause a possible bias in the discontinuity of the experimental feature distribution. To correct for such bias, this clustering was incorporated in a simulated position distribution by drawing  $N_c$  samples from  $P_u N_c$  random uniform positions in a simulated dorso-ventral (DV) recording space. This recording space was defined within  $[0,1400]$ , corresponding to the median recording position range in  $\mu\text{m}$  across all experimental data sets used.  $P_u$  is the ratio of unique recording positions to sample size (cell number) averaged over all experimental data sets used.  $P_u N_c$  was rounded to nearest integer. For each simulation, we calculated the ratio of discontinuity values from the simulated feature distribution to the simulated distribution of recording positions. The log of this ratio distributes symmetrically around zero and was used to indicate detectable modularity in the drawn distributions. Simulation of each mode-spread combination was run 100 times and the mean log discontinuity recorded in a matrix. The zero-isoline of this matrix designates the bound separating detectable (positive values) and non-detectable (non-positive values) distribution modularity.

### *Statistical procedures*

Student t-tests were used to compare groups when the data did not deviate substantially from a normal distribution and variance was comparable across groups. All t-tests were two-tailed. Data are reported as means  $\pm$  S.E.M. or means  $\pm$  S.D., as indicated. Group differences in analyses with more than two levels (e.g. anatomical bins) were assessed with analyses of variance (one-way or two-way ANOVAs). For analyses of effects by distance along the dorsal-ventral axis, anatomical bins with less than five data points were not included in any ANOVA analysis.

#### *Histology and reconstruction of recording positions*

Electrodes were not moved after the final recording session. The animals were euthanized with an overdose of pentobarbital and were transcardially perfused with 0.9% saline (wt/vol) followed by 4% formaldehyde (wt/vol). The brains were extracted and stored in 4% formaldehyde. At least 24 h later, the brains were quickly frozen, cut in sagittal sections (30  $\mu\text{m}$ ) using a cryostat, mounted and stained with cresyl violet. The positions of the tips of the recording electrodes were determined from digital pictures of the brain sections. The measurements were made using AxioVision (LE Rel. 4.3). The laminar location of the recording electrodes in MEC was determined on the basis of cytoarchitectonic criteria. The borders between MEC and presubiculum, parasubiculum and postrhinal cortical regions were determined from Nissl-stained sagittal brain sections, the Allen Brain Atlas and an atlas of the parahippocampal region [8]. These Nissl-stained sections were later used to construct unfolded maps (flat maps) of the 2D distribution of head direction tuning. For each animal, the total length of MEC layer II was first measured in the brain section with the deepest tetrode track. The location of each head direction cell was then projected onto the MEC length. MEC lengths from different animals were arranged according to medio-lateral position, creating an aggregate 2D map of the entire range over which head direction cells had been recorded. Animals were only included if head direction cells were recorded over a range of 500  $\mu\text{m}$  or more, at a minimum of 5 locations. Finally, for each animal or hemisphere, the mean dorso-ventral recording location was plotted for cells with MVLs in the top and bottom quartiles, respectively, and positions were smoothed with a boxcar filter with a Gaussian kernel.

#### *Approvals*

Experiments were performed in accordance with the Norwegian Animal Welfare Act and the European Convention for the Protection of Vertebrate Animals used for Experimental and Other Scientific Purposes. The experiments were approved by the National Animal Research Authority of Norway.

1. Brun, V.H., Solstad, T., Kjelstrup, K.B., Fyhn, M., Witter, M.P., Moser, E.I., and Moser, M.B. (2008). Progressive increase in grid scale from dorsal to ventral medial entorhinal cortex. *Hippocampus* 18, 1200-1212.
2. Sargolini, F., Fyhn, M., Hafting, T., McNaughton, B.L., Witter, M.P., Moser, M.B., and Moser, E.I. (2006). Conjunctive representation of position, direction, and velocity in entorhinal cortex. *Science* 312, 758-762.
3. Giocomo, L.M., Hussaini, S.A., Zheng, F., Kandel, E.R., Moser, M.B., and Moser, E.I. (2011). Grid cells use HCN1 channels for spatial scaling. *Cell* 147, 1159-1170.
4. Stensola, H., Stensola, T., Solstad, T., Frøland, K., Moser, M.B., and Moser, E.I. (2012). The entorhinal map is discretized. *Nature* 492, 72-78.
5. Boccara, C.N., Sargolini, F., Thorensen, V.H., Solstad, T., Witter, M.P., Moser, E.I., and Moser, M.B. (2010). Grid cells in pre- and parasubiculum. *Nat Neurosci* 13, 987-994.
6. Schmitzer-Tobert, N., Jackson, J., Henze, D., Harris, K., and Redish, A.D. (2005). Quantitative measures of cluster quality for use in extracellular recordings. *Neuroscience* 131, 1-11.

7. Langston, R.F., Ainge, J.A., Couey, J.J., Canto, C.B., Bjerknes, T.L., Witter, M.P., Moser, E.I., and Moser, M.B. (2010). Development of the spatial representation system in the rat. *Science* 328, 1576-1580.
8. Kjonigsen, L.J., Leergaard, T.B., Witter, M.P., and Bjaalie, J.G. (2011). Digital atlas of anatomical subdivisions and boundaries of the rat hippocampal region. *Front Neuroinform* 5, doi: 10.3389/fninf.2011.00002.

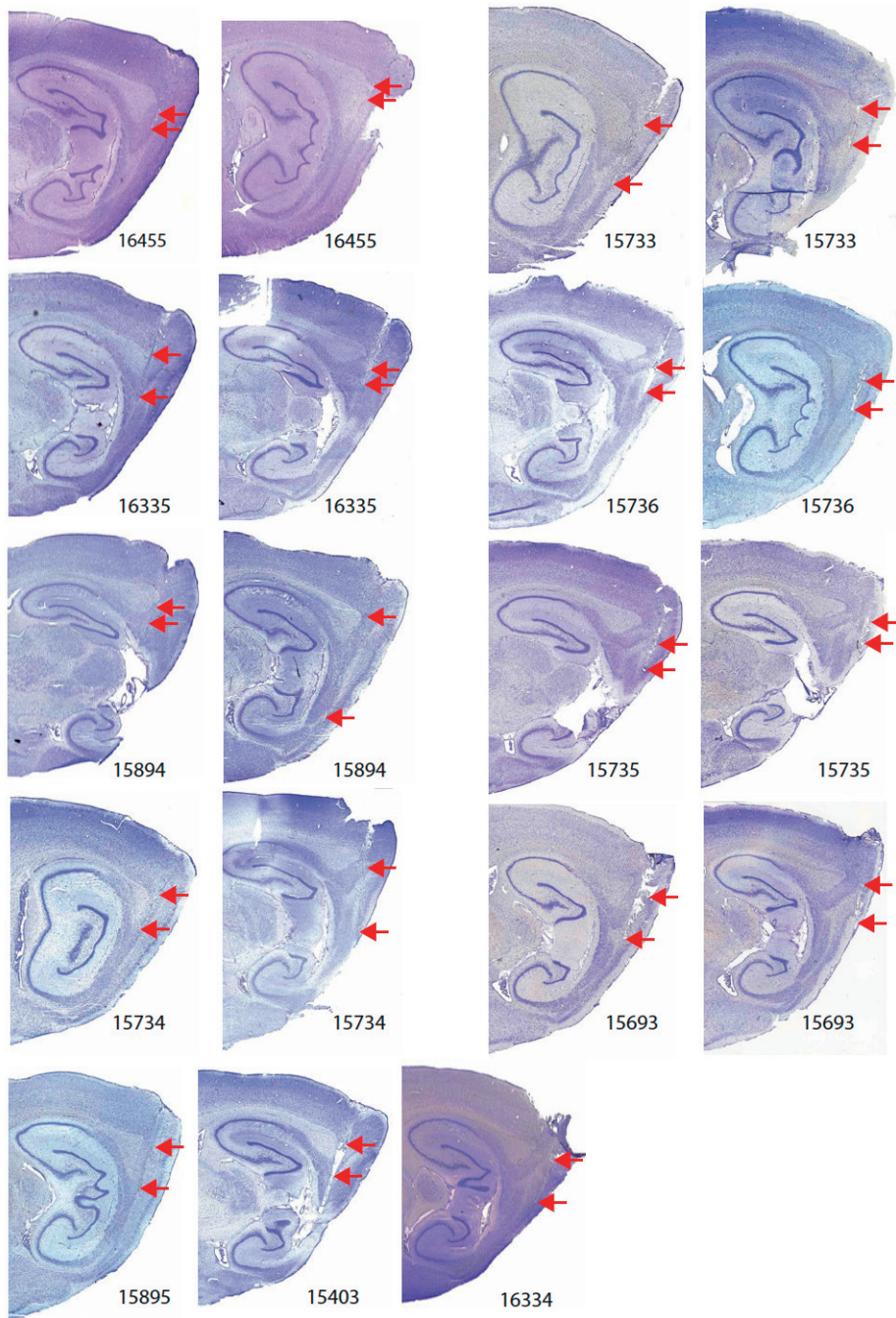


**Figure S1:** Nissl-stained sagittal sections for rats with recordings in layer III or V-VI of MEC. Red arrows mark the first (most dorsal) and last (most ventral) location where a head direction or grid cell was recorded. All rats were implanted bilaterally, except for the three rats in the bottom row. Rats that were included in previous studies are not shown. For rats with bilateral recordings, the left hemisphere is always shown first (to the left). For rat 15894, all data from the left hemisphere and portions of the right hemisphere were categorized as pre- or parasubiculum (Figure S3).

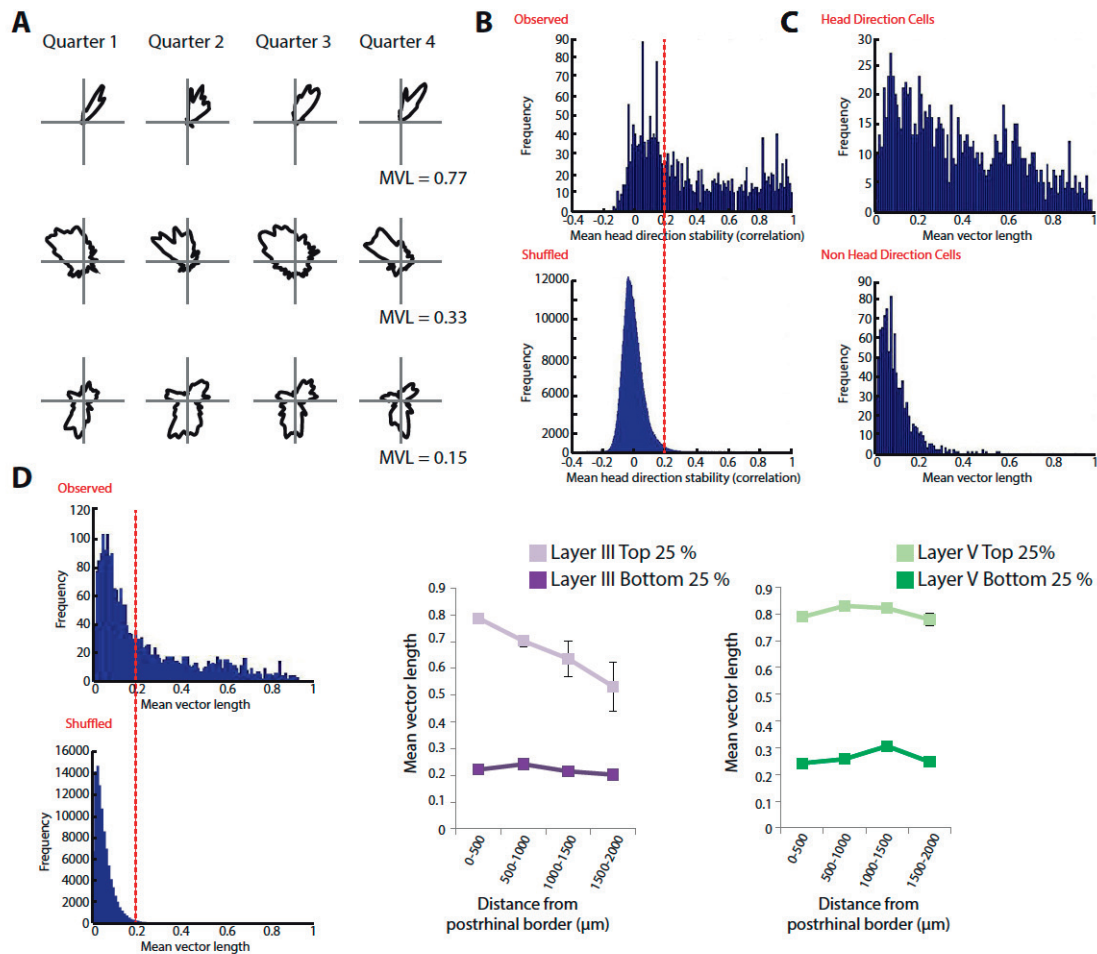


**Figure S2:** Measuring directional stability and defining the population of head direction cells.

(A) To determine the directional stability of a cell's firing pattern, the entire session was quartered into four and the directional firing preference calculated for each quarter. The directional firing preference was then correlated between quarters, until all possible combinations had been examined (Quarter 1 x Quarter 2, Quarter 1 x Quarter 3, Quarter 1 x Quarter 4, Quarter 2 x Quarter 3, Quarter 2 x Quarter 4, Quarter 3 x Quarter 4), for a total of six comparisons. The mean of all comparisons was defined as the cell's directional stability.

(B) The directional stability of each cell was compared to a shuffled distribution of directional correlations. Spike times were shifted by a random interval between 20 seconds and the total trial length minus 20 seconds, with the end of the trial wrapped to the beginning. The shuffling was repeated 400 times for each cell. For each permutation, the preferred firing direction was calculated and stability compared across the four time quarters, as described in (A). The shuffled distribution is shown on the bottom and the observed distribution on the top. The red dotted line indicates the 99th percentile threshold from the shuffled distribution used to define the head direction population in the observed data.

(C) Top: Directional tuning (mean length of the firing rate vector) of all cells defined as head direction cells based on the shuffling procedure in (B). Bottom: The mean vector length values of all cells not defined as head direction cells based on the shuffling procedure in (B).

(D) We also shuffled cells to generate a 99th percentile threshold for mean vector length ( $P99 = .19$ ). Any cell with a mean vector length higher than the 99th percentile was classified as a head direction cell for this analysis (Left). Using this approach, a significant dorsal-ventral gradient was observed in layer III (All cells  $F(3,310) = 4.62$  and  $P < 0.01$ ; Top 25%  $F(3,76) = 9.21$  and  $P < 0.001$ ) but not layer V (Top 25%  $F(3,117) = 2.6$ ,  $P > 0.05$ ) (right). The use of the directional stability measurement offers the benefit of utilizing one measure to define the population of head direction cells and a second measure (mean vector length) to examine the organization in head direction tuning. On the other hand, this analysis uses the same measure to both define the population and examine the organization in head direction tuning.

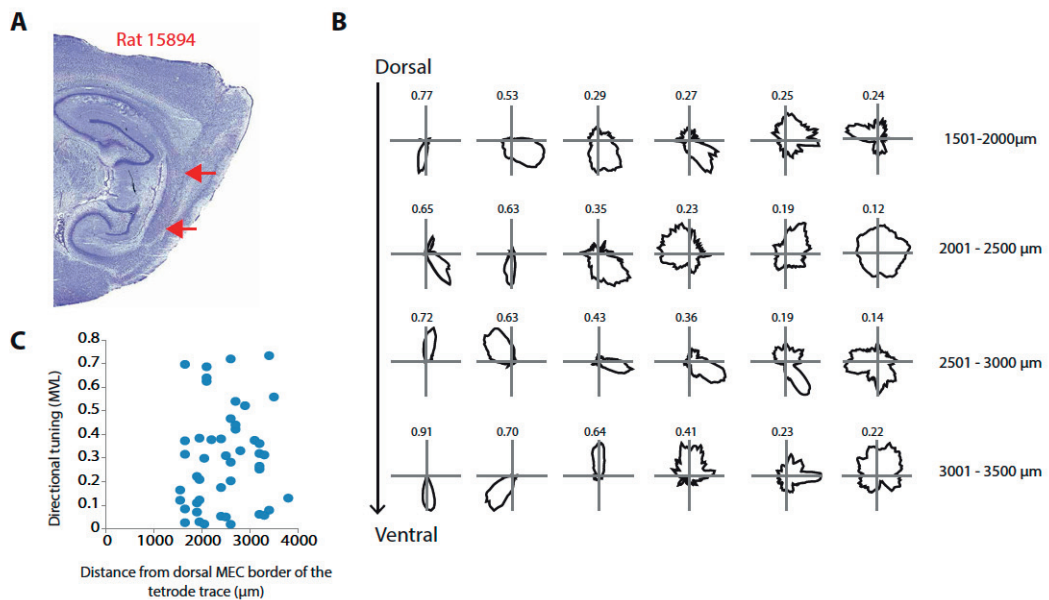


**Figure S3:** Sharp head direction tuning in ventral presubiculum. All data are from the right hemisphere of rat 15894 (Fig. S1).

(A) Nissl-stained sagittal section for a rat with tetrodes in intermediate-to-ventral presubiculum. Red arrows indicate presubiculum boundaries. Cells in B and C were recorded along the trace between the two arrows.

(B) The six head direction cells with the highest mean vector lengths in each of four successive 500  $\mu\text{m}$  bins along the dorso-ventral axis of the presubiculum (between the red arrows in A); dorsal at the top, ventral at the bottom, sharpest tuning on the left and weakest tuning on the right. Mean vector length is indicated above each cell.

(C) Directional tuning (MVL) of intermediate-to-ventral presubiculum head direction cells as a function of position along the dorso-ventral axis in A. Blue circles correspond to individual cells.

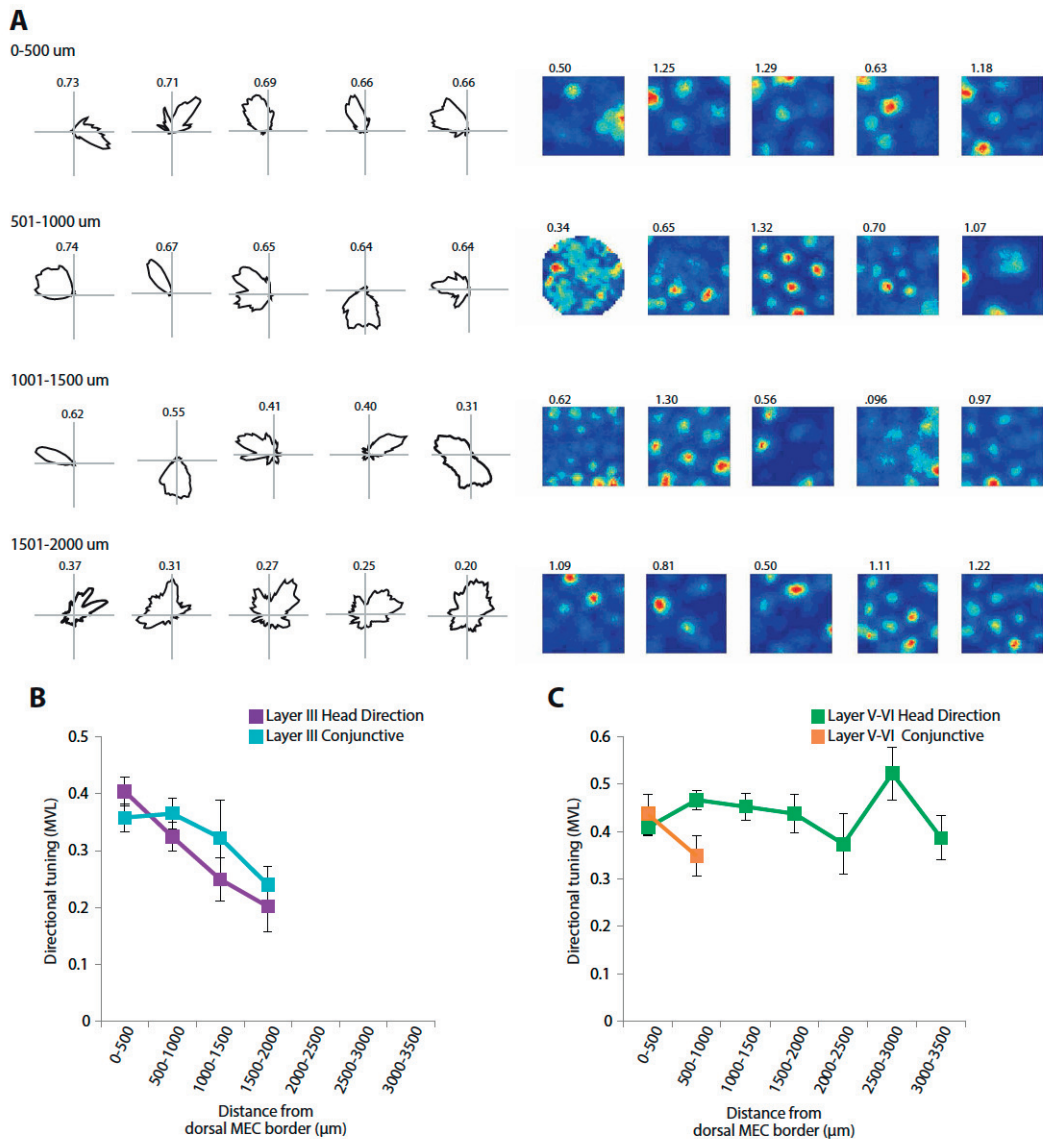


**Figure S4:** Comparison of conjunctive grid  $\times$  head direction cells with head direction cells that responded only to head direction.

(A) We defined conjunctive cells as head direction cells with a grid score higher than the 99th percentile threshold determined from a shuffled distribution ( $P_{99} = 0.34$ ; layer III  $n = 131$ , layer V  $n = 65$ ). Examples of the five conjunctive cells with the highest MVL are shown for each anatomical bin. Left: Polar plot of head direction tuning. MVL is indicated above each plot. Right: Corresponding rate map showing grid firing pattern. Grid score is indicated above each plot.

(B-C) Both layer III (B) and layer V (C) contained conjunctive cells. Bins with less than 5 cells are not shown. There was no difference in the slope of the dorso-ventral tuning gradient between pure head direction cells and head direction cells with conjunctive grid fields in layer III (Group  $\times$  Depth:  $F(3,414) = 0.87$ ,  $P = 0.45$ ). Analysis of tuning in conjunctive cells along the dorsal-ventral axis was limited, as the box size used occluded the observation of grid cells with large spatial scales.



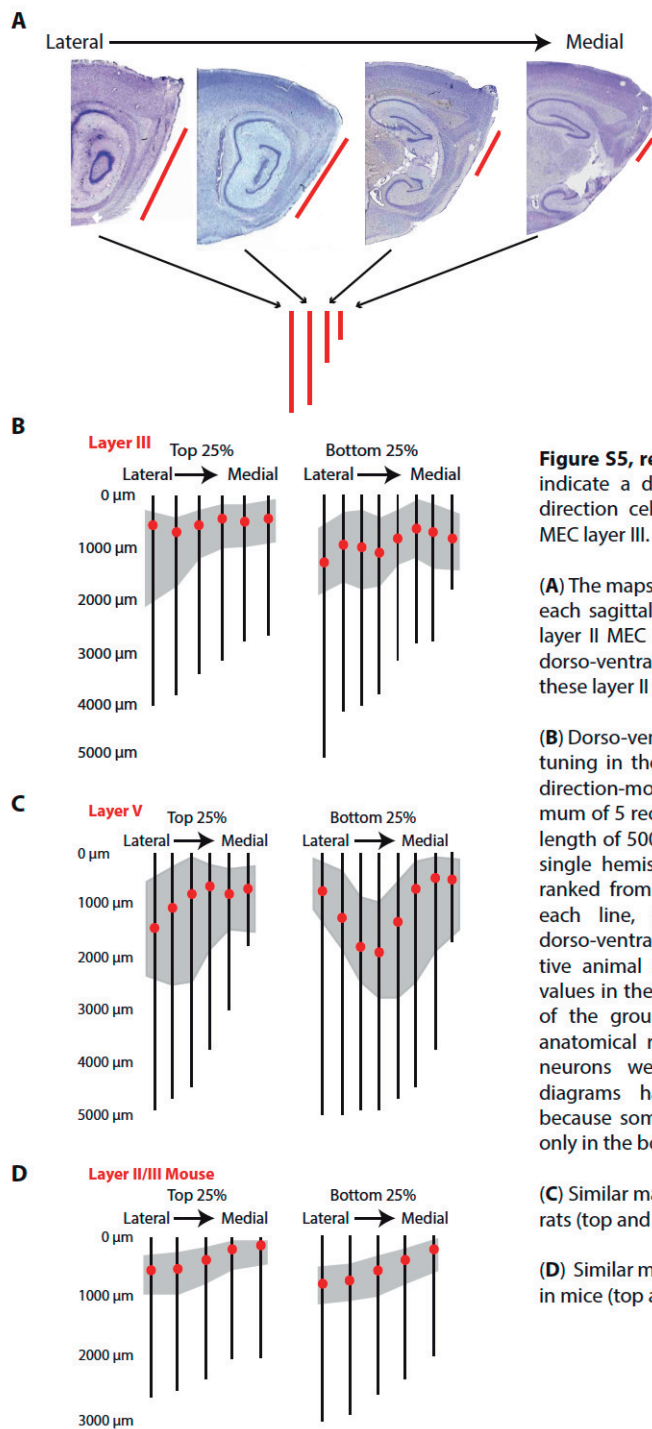


**Figure S5, related to Figure 1:** Unfolded maps indicate a dorsal band of sharply-tuned head direction cells along the medio-lateral axis of MEC layer III.

(A) The maps were constructed by measuring, for each sagittal brain section, the entire length of layer II MEC (red lines) and then projecting the dorso-ventral positions of recorded cells onto these layer II measurements.

(B) Dorso-ventral position of cells with directional tuning in the top and bottom 25% of all head direction-modulated cells in all rats with a minimum of 5 recording positions across a minimum length of 500  $\mu\text{m}$ . Each vertical line represents a single hemisphere from one animal. Lines are ranked from most lateral to most medial. On each line, a red dot indicates the mean dorso-ventral position for all cells of the respective animal that had directional tuning (MVL) values in the top (left) or bottom (right) quartile of the group data. Light gray highlights the anatomical range across which head direction neurons were recorded. The left and right diagrams have different numbers of lines because some rats had cells only in the top or only in the bottom quartile of the group data.

(C) Similar maps for layer V recording positions in rats (top and bottom quartiles).

(D) Similar maps for layer II-III recording positions in mice (top and bottom quartiles).

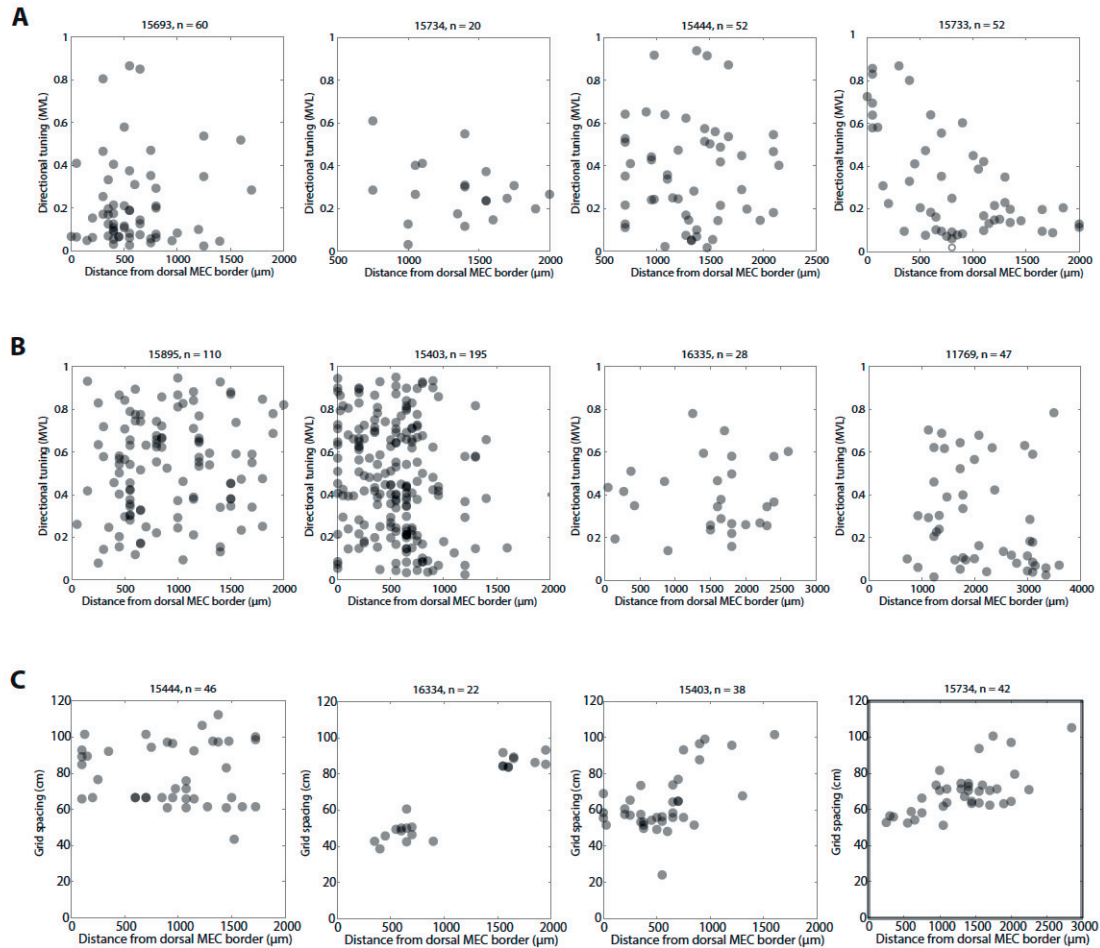


**Figure S6, related to Figure 5:** Distribution of directional tuning and grid spacing along the dorso-ventral axis of MEC. Distributions are shown for all rats with head direction cells or grid cells sampled over a distance of 2000 μm or more along the dorso-ventral MEC axis.

(A-B) Directional tuning distribution in MEC layer III (A) and layer V-VI (B). Each panel in A and B shows the mean vector length (MVL) of the directional distribution of firing rate for all identified head direction cells in one animal, plotted as a function of dorso-ventral recording location (distance in micrometers from the dorsal MEC border). Each dot corresponds to one cell. To allow visualization of overlapping data points, dot color is multiplicative. Rat identity and sample size are indicated atop each plot. The gradient in head directional tuning in layer III was not dependent on any single animal, as significance was maintained with the removal of individual animals (All ANOVA  $P < .05$  and all correlation  $P$  values  $< .001$ ).

(C) Distribution of grid spacing along the dorso-ventral MEC axis. Each panel shows grid spacing from all grid cells in one animal. Symbols as in A-B.



## Paper III

Is not included due to copyright

